Charles University in Prague

Faculty of Mathematics and Physics

DOCTORAL THESIS

Eva Havlíčková

Computer modelling of plasma processes and transport for selected applications

Department of Surface and Plasma Science

Supervisor: Prof. RNDr. Rudolf Hrach, DrSc.

Study programme: Mathematical and Computer Modelling

A dissertation submitted in conformity with the requirements
for the degree of Doctor of Philosophy

I would like to thank my supervisor, Professor Rudolf Hrach, for leadership and valuable recommendations during the whole study. I am grateful to colleagues from IPP Prague for their support and hospitality and colleagues from EURATOM/IPPLM, EURATOM/UKAEA, EURATOM/Risø and scientists working within the EFDA-JET TF-E Modelling month for inspiration, discussions and fruitful collaboration.

I hereby declare that this thesis is my own work based on the cited sources and literature. I approve to make the thesis available for lending.

Prague, September 7, 2009 Eva Havlíčková

Contents

1 Objectives 1

I MODELLING OF PLASMA-SOLID INTERACTION IN DC GLOW DISCHARGE 3

2 Theoretical background 5
- 2.1 Probe theory . . . 5
- 2.2 Experimental setup of glow discharge . . . 6
- 2.3 Computational approach . . . 7
  - 2.3.1 Microscopic description . . . 7
  - 2.3.2 Kinetic description . . . 8
  - 2.3.3 Fluid description . . . 9
- 2.4 Computational fluid dynamics . . . 12
  - 2.4.1 Finite difference method . . . 13
  - 2.4.2 Finite element method . . . 14
  - 2.4.3 Finite volume method . . . 15
  - 2.4.4 Comparison . . . 16

3 Introduction 18

4 Two-dimensional particle-in-cell simulation 20
- 4.1 Basic features . . . 20
- 4.2 Computational method . . . 21
  - 4.2.1 Molecular dynamics simulation . . . 22
  - 4.2.2 Particle-in-cell method . . . 23
  - 4.2.3 Algorithm for solving Poisson's equation . . . 24
  - 4.2.4 Non self-consistent technique . . . 25
- 4.3 Basic results . . . 25

5 Two-dimensional fluid model 29
5.1 Fluid description and governing equations 29
5.2 Computational method 30
5.2.1 Poisson solver 30
5.2.2 Transport equations 31
5.2.3 Boundary conditions 33
5.3 Basic results 34

6 Results 37
6.1 Influence of collisions 37
6.2 Influence of pressure 38
6.3 Influence of magnetic field 39
6.4 Influence of geometry 41
6.5 Discussion and comparison 42

7 Conclusions 47

II TOKAMAK PLASMA MODELLING 49

8 Theoretical background 51
8.1 Tokamak configuration 51
8.2 Plasma-solid interaction 52
8.2.1 Sheath properties 52
8.2.2 Plasma-surface processes 54
8.3 Plasma transport 55
8.4 Operational regimes 56
8.4.1 Simple SOL 56
8.4.2 Complex SOL 56
8.4.3 Ionization of neutrals 56
8.4.4 Detachment 57
8.5 Edge plasma modelling 58
8.5.1 Two-point model 59
8.5.2 One-dimensional fluid model 60
8.5.3 Two-dimensional fluid model 61

9 Introduction 62
9.0.4 Present status 62
9.0.5 Outline of presented work 64

10 Numerical investigation of plasma parameters in COMPASS tokamak **65**
10.1 COMPASS device 65
10.2 Numerical model 66
10.2.1 Core region 66
10.2.2 Boundary region 67
10.3 Results 68
10.4 Summary 72

11 One-dimensional model of edge plasma transport **73**
11.1 Basic features 73
11.2 Mathematical description 74
11.2.1 Fluid equations 74
11.2.2 Source terms 76
11.2.3 Transport properties 77
11.2.4 Model of neutrals 79
11.3 Computational method 79
11.3.1 Technique of discretization 80
11.3.2 Algorithm for solving system of linear equations 81
11.3.3 Boundary conditions 82
11.4 Results 84
11.4.1 Input parameters 84
11.4.2 Basic plasma model 85
11.4.3 Influence of neutrals 86
11.4.4 Dependence on operational conditions 88
11.5 Validation and benchmark 90
11.5.1 Symmetry verification 90
11.5.2 Test of conservation 92
11.5.3 Benchmark with B2 93
11.6 Application to time-dependent problems 94
11.6.1 Comparison with analytic model for steady state . . . 96
11.6.2 Transient studies 100
11.6.3 Final coupling 111

12 Introduction to two-dimensional edge modelling **113**
12.1 Plasma edge and numerical tools 113
12.2 Grid and geometry 114
12.3 Fluid model and mathematical description 115
12.4 Model of neutrals 116
12.5 Boundary conditions 117
12.6 Drifts and currents 118

12.7 Numerics and overview 119

13 Conclusions 121

References 123

CHAPTER 1

Objectives

The presented work contributes to computer modelling of plasma. Various techniques have been applied to solve several selected problems of plasma physics. The work is divided into two parts according to areas of plasma physics that are investigated. Both parts start with a basic theoretical background that is essential for understanding the problems and provides an introduction to studied problems on a general level (chapters 2 and 8). An introduction to the presented work and the scope of the work follow with a short description of the main points which the work is focused on (chapters 3 and 9). Some common aspects of both parts can be found in used numerical techniques and algorithms. A brief review of elementary methods and their mathematical description is given in the first part and the implemented algorithms are then described in detail in individual sections.

The objective of the first part was to create a tool to simulate the plasma-solid interaction in conditions typically observed in a low-temperature glow discharge plasma. Two different methods of computational physics are used and compared (chapters 4–6).

The second part gathers computational studies of plasma behaviour in the fusion research. The work focuses specifically on the edge plasma transport in tokamaks. Several subjects of interest have been investigated and they follow each other according to the level of their complexity. First, plasma parameters in a tokamak are studied from the global point of view by means of a code coupling the main plasma and the edge region and using a simple description of the edge plasma behaviour (chapter 10). Further, a one-dimensional fluid model of the edge plasma has been developed and its description and application to time-dependent problems follow in chapter 11. The work presented in chapter 11 represents the key point of the thesis. Chapter 12 provides an introduction to two-dimensional edge modelling. Main points for a possible continuation are summarized in the last chapter.

PART I

MODELLING OF PLASMA-SOLID INTERACTION IN DC GLOW DISCHARGE

CHAPTER 2

Theoretical background

2.1 Probe theory

One of the fundamental techniques for measuring the properties of a plasma is the probe diagnostics. The current collected by the probe, biased at a given voltage, provides information about the conditions in the plasma [1].

When a solid or a biased electrode is immersed into a plasma, a local disturbance develops and the Debye sheath is formed in the vicinity of the electrode. The condition of quasi-neutrality is not valid near the surface, the ion and electron densities can differ and large electric field can be sustained [1, 2].

Let us assume a one-dimensional example. The effect of introducing a potential φ_0 at $x = 0$ is given by a solution of Poisson's equation

$$\varphi = \varphi_0 \mathrm{exp}\left(-\frac{x}{\lambda_\mathrm{D}}\right). \tag{2.1}$$

We assumed that electrons are in thermal equilibrium and satisfy the Boltzmann relation $n_\mathrm{e} = n_0 \mathrm{exp}(e\varphi/kT_\mathrm{e})$ and ions are infinitely massive so that the ion density $n_\mathrm{i} = n_0$ is constant. The decay length λ_D is called the Debye length, n_0 is the undisturbed plasma density and x is the distance from the position where the potential is imposed. The externally imposed potential is shielded within a distance of the order of λ_D and outside the sheath region, the plasma remains quasineutral $n_\mathrm{e} \simeq n_\mathrm{i}$ [1]. The Debye length is here defined as

$$\lambda_\mathrm{D} = \sqrt{\frac{\epsilon_0 k T_\mathrm{e}}{n_0 e^2}}. \tag{2.2}$$

The I-V characteristic measured by the probe (the current flowing to the surface as a function of the voltage) allows to determine the physical properties of the plasma – the density, the electric potential, the electron temperature (in case of the Maxwell energy distribution) or the electron energy distribution function in general case. The analysis and theoretical aspects are described in [1] where basic relations between the measured parameters and the properties of the plasma are derived.

The probe diagnostics has the advantage of providing local measurements. Experimentally, the electrostatic probes are simple devices, the theory of probes, however, is complicated and certain assumptions and simplifications are required. There is only a limited range of conditions under which the derived theoretical formulas are justified and do not lead to faulty interpretations. The theory becomes further complicated when a magnetic field or negative ions are present. The exact way in which the plasma parameters are related to the probe characteristic depends on the probe shape. The fundamental Langmuir theory involves the planar, cylindrical and spherical geometry and the configuration of a single or double probe. In a hot, dense and magnetized plasma as found in the fusion research, more complicated configurations or different types of probes can be used.

2.2 Experimental setup of glow discharge

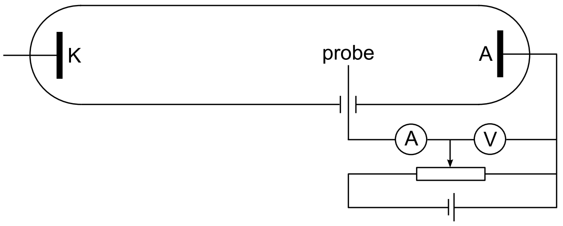

Figure 2.1: A circuit for probe measurements in the glow discharge.

The classical and fundamental device where the probe measurements can be easily performed is illustrated in Fig. 2.1. The scheme of a discharge involves two metal electrodes connected to a DC power supply enclosed in a glass tube of the radius $R \sim 1$ cm. The tube can be evacuated and filled with various gases at different pressures [3].

Typical conditions in a glow discharge are low currents ($I \sim 10^{-6} - 10^{-1}$ A), low or medium pressures ($p \approx 100 - 1000$ Pa) and high voltages ($U \sim 100 - 1000$ V). The glow discharge plasma is very weakly ionized and the temperature of the electrons and ions is widely separated ($T_\mathrm{e} \sim 10^4$ K, $T_\mathrm{i} \approx 300$ K).

To perform the probe analysis of the glow discharge, a probe is inserted into the positive column of the discharge. The classical Langmuir probe is a metal conductor of the planar, cylindrical or spherical shape and its inactive part is coated by an insulator. The characteristic size is about 0.1–1 mm or even smaller. The probe potential is imposed by a DC power supply and it is determined with respect to a reference electrode, typically the anode (Fig. 2.1).

2.3 Computational approach

Plasma processes in the vicinity of an electrode inserted into a plasma can be simulated numerically. The investigation of the plasma-solid interaction plays an important role in the field of the probe diagnostics or plasma technologies and the computer modelling might effectively enrich the theoretical studies and experimental observations.

In any macroscopic physical system containing many individual particles, there are basically three levels of the mathematical description: the exact microscopic description, the kinetic theory, and the macroscopic or fluid description. The computational treatment of a plasma system can be build up on the basis of these three fundamental approaches.

The microscopic approach leads to computationally intensive simulations. An accurate description of the behaviour of the system, based on an analysis of the trajectories of all constituent particles might be virtually impossible for some problems. On the other hand, the macroscopic information might be insufficient for some applications. Therefore these two descriptions are sometimes combined together into the hybrid modelling approach [4, 5]. Other applications combine the kinetic description with the fluid approach and treat some components of the system as a fluid and others kinetically. Another description, appropriate for a high-temperature plasma in strong magnetic fields, averages the kinetic equations over the fast circular motion of the gyroradius. The gyrokinetic modelling has been extensively used in tokamak simulations.

2.3.1 Microscopic description

The behaviour of a system can be described on the microscopic level when the dynamics of the system is based on a description of the motion of all individual particles. Because the system generally consist of a large number of the particles, it is impossible to find the properties of such complex system analytically.

The microscopic approach is the principle of the Molecular dynamics (MD), a computational technique in which the equations of motion of the particles are solved numerically [6]. The algorithm comprises several stages.

Interactions between the particles are described by a force field. Since a precise calculation of the force field (the potential) as a sum of the forces from all the constituent particles would be intolerably time-demanding, various effective algorithms (e.g. the particle-in-cell (PIC), the particle-particle-particle-mesh (P^3M), the Ewald summation or the fast multipole method (FMM)) are being implemented. The motion of the particles in a force field $\mathbf{F}$ is governed by Newton's laws

$$\frac{\mathrm{d}\mathbf{r}}{\mathrm{d}t} = \mathbf{v}, \tag{2.3}$$

$$\frac{\mathrm{d}\mathbf{v}}{\mathrm{d}t} = \frac{\mathbf{F}}{m}. \tag{2.4}$$

The ordinary differential equations (2.3) and (2.4) are solved numerically by propagating the solution in time with given initial conditions. The algorithm used to update the positions and velocities of the particles can be typically based e.g. on the second-order Leap-frog or Verlet integrator [7].

In a low-temperature and weakly ionized plasma, such as the glow discharge plasma, collisions of charged species with neutrals are significant and have to be taken into account. Apparently, the whole system of the plasma and neutrals would be insoluble purely within the MD approach and in this case, only the charged plasma species are evolved by the MD simulation, while the collisions with the neutrals are treated separately. The neutrals constitute a background in which the plasma particles are scattered. The most natural method to describe the plasma-neutral collisions is a stochastic treatment based on the Monte Carlo (MC) technique [8], using the cross-sections of individual reactions or the mean free path characterizing the rate of the collisions.

The MD simulations are costly in computer time, especially in two or three dimensions. The setup of the MD simulation – namely the time step, the number of particles and the grid spacing should account for the available computational power. The most time-consuming task is the evaluation of the force field from the positions of the particles and parallel algorithms that allow to distribute the computation among more CPUs are highly appreciated.

2.3.2 Kinetic description

The accurate description of a plasma system, based on an analysis of the trajectories of particles, is theoretically too complex and the models may be in practise computationally insoluble for some problems. Then the probability concepts can be applied and the plasma behaviour can be solved by statistical methods of physical kinetics.

The main statistical characteristic of the system in the kinetic approach is the distribution function $f = f(\mathbf{r}, \mathbf{v}, t)$, the probability density to find a particle at time t at position $\mathbf{r}$ with velocity $\mathbf{v}$. By averaging out the microscopic information in the exact theory, one obtains statistical equations describing the evolution of the distribution function. The essential equation of the kinetic theory is the Boltzmann equation (BE)

$$\frac{\partial f}{\partial t} + \mathbf{v} \cdot \nabla f + \frac{\mathbf{F}}{m} \cdot \nabla_v f = \left(\frac{\partial f}{\partial t} \right)_{\mathrm{c}} \tag{2.5}$$

which can be derived from Liouville's theorem. In practise, the Vlasov equation – a formulation in the absence of collisions and assuming that the force is exclusively electromagnetic or the Fokker-Planck equation – a formulation when the Coulomb collisions are present, are commonly used.

The kinetic equation can not be solved analytically in general. It is a non-linear integro-differential equation that contains the collision integral and it can be solved analytically only in special cases. The numerical solution of the Boltzmann equation represents a real challenge for numerical methods. The difficulties of the numerical solution are caused by the non-linearity, the complexity due to the dimensionality (large number of independent variables) and the evaluation of the integral that defines the collision operator.

A variety of techniques for integrating the differential equation have been applied to solve the equations computationally, commonly with the Monte Carlo method for evaluating the collision integral [9]. The kinetic treatment is not further considered in the thesis.

2.3.3 Fluid description

Averaging the kinetic theory even further by deriving velocity moments of the Boltzmann equation, a set of partial differential equations (PDEs) can be established, describing the evolution of macroscopic plasma quantities such as the density, the mean velocity or the pressure, without any knowledge of the individual particle motion. The numerical solution of the fluid model will be introduced in section 2.4 devoted to methods of computational fluid dynamics (CFD).

Theoretical definition

Zero moment of the Boltzmann equation ($\int_{-\infty}^{+\infty}(\mathrm{BE})\,\mathrm{d}^3v$) is the continuity equation for the particle density

$$\frac{\partial n}{\partial t} + \nabla\cdot(n\mathbf{u}) = \frac{Q^\rho}{m}. \tag{2.6}$$

The source term on the right-hand side of the equation (2.6) corresponds to the collision term of the Boltzmann equation and describes a mass production and annihilation due to the ionization and recombination or eventually due to other processes. Similarly, the momentum transport equation

$$\frac{\partial(mn\mathbf{u})}{\partial t} + \nabla(mn\mathbf{uu}) + \nabla\mathbb{P} - nq(\mathbf{E}+\mathbf{u}\times\mathbf{B}) = \mathbf{u}Q^\rho + \mathbf{Q}^p \tag{2.7}$$

can be obtained as the first moment of the Boltzmann equation ($m\int_{-\infty}^{+\infty}\mathbf{v}\,(\mathrm{BE})\,\mathrm{d}^3v$). Here we substituted the Lorentz force $\mathbf{F} = q\,(\mathbf{E}+\mathbf{v}\times\mathbf{B})$. The second moment ($\frac{1}{2}m\int_{-\infty}^{+\infty}v^2\,(\mathrm{BE})\,\mathrm{d}^3v$) determines the energy transport

$$\begin{aligned}\frac{\partial}{\partial t}\left(\frac{1}{\gamma-1}p + \frac{1}{2}mnu^2\right) + \nabla\cdot\left(\frac{1}{\gamma-1}p\mathbf{u} + \mathbf{u}\mathbb{P} + \frac{1}{2}mnu^2\mathbf{u} + \mathbf{q}\right)\\ -nq\mathbf{E}\cdot\mathbf{u} = \frac{1}{2}u^2Q^\rho + \mathbf{u}\cdot\mathbf{Q}^p + Q^E.\end{aligned} \tag{2.8}$$

$\mathbb{P}_{\mathrm{ij}} = p\,\delta_{\mathrm{ij}}$ defines the scalar pressure p and γ in (2.8) is the ratio of specific heats, i.e. $\gamma = \frac{5}{3}$ if a gas has three degrees of freedom for motion. The mean parameters (the density n, velocity $\mathbf{u}$, pressure tensor $\mathbb{P}$ and heat flux $\mathbf{q}$) are defined as

$$n = \int_{-\infty}^{+\infty} f\,\mathrm{d}^3v, \tag{2.9}$$

$$\mathbf{u} = \frac{1}{n}\int_{-\infty}^{+\infty}\mathbf{v}f\,\mathrm{d}^3v, \tag{2.10}$$

$$\mathbb{P} = m\int_{-\infty}^{+\infty}(\mathbf{v}-\mathbf{u})(\mathbf{v}-\mathbf{u})f\,\mathrm{d}^3v, \tag{2.11}$$

$$\mathbf{q} = \frac{1}{2}m\int_{-\infty}^{+\infty}(\mathbf{v}-\mathbf{u})(\mathbf{v}-\mathbf{u})^2f\,\mathrm{d}^3v \tag{2.12}$$

and the following formulas define the transport of the mass, momentum and energy due to collisions

$$Q^{\rho} = m \int_{-\infty}^{+\infty} \left(\partial f/\partial t\right)_{\mathrm{c}} \, \mathrm{d}^3 v, \tag{2.13}$$

$$\mathbf{Q}^{p} = m \int_{-\infty}^{+\infty} (\mathbf{v} - \mathbf{u}) \left(\partial f/\partial t\right)_{\mathrm{c}} \, \mathrm{d}^3 v, \tag{2.14}$$

$$Q^{E} = \frac{1}{2} m \int_{-\infty}^{+\infty} (\mathbf{v} - \mathbf{u})^2 \left(\partial f/\partial t\right)_{\mathrm{c}} \, \mathrm{d}^3 v. \tag{2.15}$$

Classical fluid formulation

We could continue to derive the moments of the Boltzmann equation for high-order terms, the equation chain must be, however, truncated somewhere. In many practical problems this is made in the first order by substituting the energy equation by an equation of the state, e.g. $p = nkT$, or in the second order by using a closure approximation for the heat flux $\mathbf{q}$, e.g. the algebraic expression $\mathbf{q}_{\mathrm{e}} = -\frac{5}{2} k D_{\mathrm{e}} n_{\mathrm{e}} \nabla T_{\mathrm{e}}$, known as Fourier's approximation [10]. The equations (2.6)–(2.8) constitute a typical set of the fluid equations which are used in many simulations. To complete the system of the equations and establish the self-consistent description of a plasma, we must describe the electromagnetic behaviour of the plasma. The system is therefore closed by Maxwell's equations. The precise derivation of the fluid equations is explained in [11] in more detail.

Various specific applications of the fluid theory requires different forms of models. Generally, we can use one set of the fluid equations for each plasma species. This constitutes the two-fluid model if we consider a simple two-component (ion and electron) plasma. Another alternative when plasma is considered as a single fluid in the center of mass frame constitutes the most widely known plasma theory – magnetohydrodynamics [2].

Sources and sinks of the mass, momentum and energy due to collisions are generally very complicated functions of the velocity and they are commonly simplified in the following manner. The mass balance collision term in the equation (2.6) gives the rates of creation and loss of species. The productivity of the reactions is defined by the reaction rate coefficients k_{r} corresponding to a collision of type r. Assuming an electron collision with a neutral, the source term for the formation of species k can be evaluated as

$$Q^{\rho}_{\mathrm{k}} = m_{\mathrm{k}} \sum_{\mathrm{r}} l_{\mathrm{rk}} k_{\mathrm{r}}(T_{\mathrm{e}}) n_{\mathrm{e}} n_{\mathrm{n}} \tag{2.16}$$

where l_{rk} is the number of particles of species k created or lost per the collision type r [12]. The reaction rate coefficient is defined as $k_{\mathrm{r}} = \langle v\sigma_{\mathrm{r}} \rangle$ where σ_{r} is the cross-section of the collision r. A useful approximation of the collision term in the momentum transport equation (2.7) and the energy equation (2.8) is Krook's approximation

$$\mathbf{Q}_{\mathrm{k}}^{p} = -\sum_{\mathrm{l}} \frac{m_{\mathrm{k}} m_{\mathrm{l}}}{m_{\mathrm{k}} + m_{\mathrm{l}}} n_{\mathrm{k}} \left(\mathbf{u}_{\mathrm{k}} - \mathbf{u}_{\mathrm{l}}\right) \overline{\nu}_{\mathrm{kl}}, \tag{2.17}$$

$$Q_{\mathrm{k}}^{E} = -\sum_{\mathrm{l}} \frac{3}{2} k\, n_{\mathrm{k}} \frac{2 m_{\mathrm{k}} m_{\mathrm{l}}}{(m_{\mathrm{k}} + m_{\mathrm{l}})^2} \left(T_{\mathrm{k}} - T_{\mathrm{l}}\right) \overline{\nu}_{\mathrm{kl}} \tag{2.18}$$

where $\overline{\nu}_{\mathrm{kl}}$ is the mean collision frequency [13].

The fluid equations are usually simplified further. In some cases, viscous effects characterized by the anisotropic part of the pressure can be neglected and the pressure tensor $\mathbb{P}$ is reduced to the scalar pressure p. The electron energy equation is often simplified by neglecting the kinetic energy contribution compared to the thermal one. Another standard modelling approach used commonly in many simulations is the drift-diffusion approximation [10, 14–18]. The full momentum equation (2.7) is replaced by an algebraic expression for the particle flux and the number of partial differential equations in the model is reduced. The transport of species due to the density gradient and the transport of charged species under the influence of an electric field

$$\frac{\partial n}{\partial t} + \nabla \cdot \mathbf{\Gamma} = \frac{Q^{\rho}}{m}, \tag{2.19}$$

$$\mathbf{\Gamma} = \pm \mu n \mathbf{E} - \nabla(Dn) \tag{2.20}$$

is described by the mobility μ and the diffusion coefficient D. The expression (2.20) is equivalent to the equation of motion (2.7) after neglecting the unsteady and inertial contribution (the first and second term). Conditions under which the drift-diffusion approximation is fulfilled are mentioned in [10–12]. In these publications, one can find also useful closure approximations or the issue of the treatment of collision processes.

2.4 Computational fluid dynamics

The fluid model introduced in the previous section is a set of non-linear partial differential equations and can be solved by methods of computational fluid dynamics. The most fundamental consideration in CFD is how to treat a continuous fluid in a discretized fashion on a computer. The spatial domain is discretized into small cells to form a grid and a suitable algorithm is then applied to solve the equations. Commonly, the algorithms convert the problem of PDE solution to solving a system of algebraic equations (Fig. 2.2), however, they differ in a way how the differential equations are discretized and how the individual differentiated terms in PDEs are replaced by algebraic expressions connecting nodal values on the grid. Generally, we can distinguish between the finite difference method (FDM), finite element method (FEM) and finite volume method (FVM). Time derivatives in time-dependent equations are discretized almost exclusively using the finite difference approach.

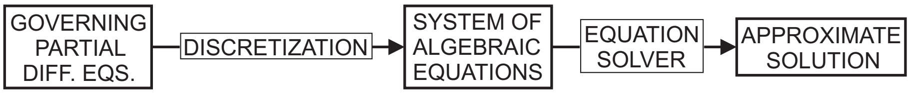

Figure 2.2: An overview of the computational solution.

2.4.1 Finite difference method

The method of finite differences is widely used in CFD [19–21]. The finite difference representation of derivatives is based on Taylor's series expansions. The discretization process introduces an error dependent on the order of terms in the Taylor's series which are truncated. The derivation of elementary finite difference schemes of the first-order or second-order accuracy is described in [22].

To represent the derivatives by the differences, a number of choices is available, especially when the dependent variable appearing in the governing equation is a function of both coordinates and time. In that case, the finite difference approach can be divided into implicit and explicit techniques. The explicit techniques are relatively simple to set up and program, but there are stability constraints given by Von Neumann method [22] which can result in long computer running times. On the other hand, the implicit methods are stable even for larger values of the time step, however, a system of algebraic equations must be solved at each time step and thus the implicit techniques are more complicated to implement.

Publications devoted to the fluid modelling in plasma physics mention a variety of methods based on the finite difference schemes, namely the explicit Lax-Wendroff and MacCormack's methods, the implicit Crank-Nicholson scheme, all described in [22] in more detail. At last, let us mention the drift-diffusion approximation (section 2.3.3) representing a PDE of convection-diffusion type. The standard explicit treatment requires too small grid spacing and therefore special discretization schemes have been developed.

The most widely used is the Scharfetter-Gummel implicit scheme [23], originally developed in the frame of semiconductor device simulations.

2.4.2 Finite element method

The finite element formulation is introduced in [22, 24]. A computational domain is divided into non-overlapping elements. The elements have either a triangular or a quadrilateral form, they can be curved and cover the whole domain. The grid formed by the elements need not be structured, in opposite to the FDM.

The basic philosophy of the FEM is that an approximate solution u of the discrete problem is assumed a priori to have a prescribed form and to belong to a function space

$$u = \sum_{j=1}^{\mathrm{N}} u_j \phi_j(x, y, z). \tag{2.21}$$

The basis (shape) functions ϕ_j are chosen almost exclusively from low-order piecewise polynomials and it is computationally advantageous to assume a function non-zero in the smallest possible number of elements associated with the function (Fig. 2.3).

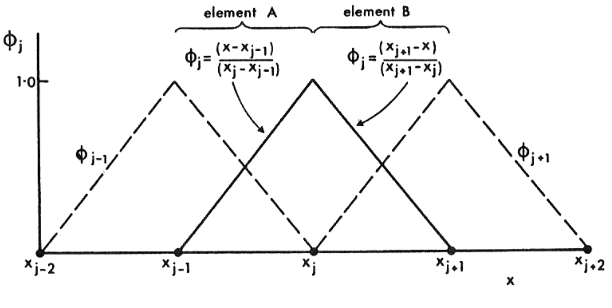

Figure 2.3: One-dimensional linear approximating functions. Reprinted from [24].

The FEM does not look for a solution of a partial differential equation itself, but looks for a solution of the integral form of the PDE obtained from a weighted residual formulation [22, 24]. The unknown coefficients u_j are determined by requiring that the integral of the weighted residual R of the PDE over the computational domain Ω is zero

$$\int_{\Omega} W_j(x, y, z)\, R\, dx\, dy\, dz = 0 \qquad j = 1, 2, ..., \mathrm{N}. \tag{2.22}$$

Different choices for the weight function W_j give rise to different methods in the class of methods of weighted residuals. In the FEM, the weight functions are chosen from the same family as the basis functions $W_j = \phi_j$, which is the most popular choice. The equation (2.22) results in a system of algebraic equations for the coefficients u_j or a system of ordinary differential equations in case of time-dependent problems. The finite element approach is applied in [25] for example.

2.4.3 Finite volume method

The fundamental idea of the finite volume method is to discretize the integral form of equations instead of the differential form and it can be thought as a special case of the so-called subdomain method [24]. A computational domain is subdivided into a set of cells that cover the whole domain (Fig. 2.4). The volumes on which the integral forms of conservation laws are applied need not coincide with the cells of the grid and they can even be overlapping. Different choices of volumes determine different formulations of the FVM.

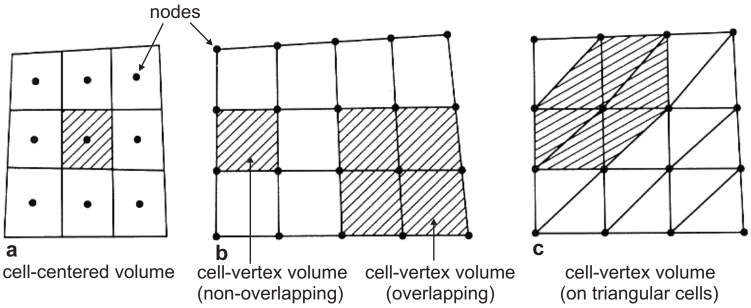

Figure 2.4: A typical choice of the volumes in the FVM. Reprinted from [22].

A PDE is integrated over the control volume and then an approximate evaluation of the integral form is obtained by the discretization. As a brief example, let us consider the cell-vertex formulation (Fig. 2.5) applied to a PDE of the form

$$\frac{\partial u}{\partial t} + \frac{\partial f}{\partial x} + \frac{\partial g}{\partial y} = 0. \tag{2.23}$$

Integrating the equation (2.23) over the control volume ABCD (Fig. 2.5) and applying Green's theorem yields the integral form

$$\frac{d}{dt}\int u\,dV + \int\limits_{\mathrm{ABCD}} (f\,dy - g\,dx) = 0 \tag{2.24}$$

that can be discretized to obtain an approximate equation for each nodal point (j,k)

$$S_{\mathrm{ABCD}}\,\frac{du_{j,k}}{dt}+\sum_{\mathrm{AB}}^{\mathrm{DA}}(f\,\Delta y-g\,\Delta x)=0. \tag{2.25}$$

The discretization scheme again represents a system of algebraic equations. An introduction to the finite volume technique is given in [22]. The method has been applied e.g. in [26].

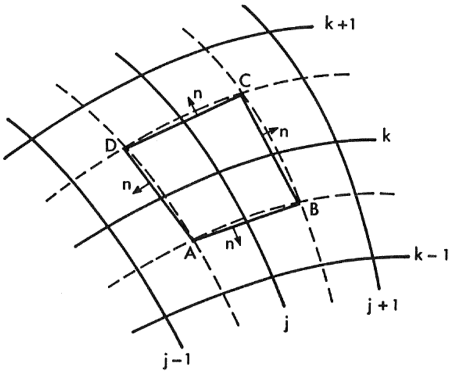

Figure 2.5: A two-dimensional finite volume. Reprinted from [24].

2.4.4 Comparison

Both finite difference techniques and methods based on the weighted residual formulation are widely used in simulations. The advantage of the FDM is its relatively simple implementation, especially in case of problems which do not require to transform coordinates. By contrast, a practical use of the FEM and FVM in simulations is usually connected with commercial solvers such as FLUENT [27–29] or COMSOL Multiphysics [30].

The principle and comparisons of these three techniques are demonstrated in [22, 24] on various applications and specific examples. The most important advantage of the FEM and FVM is a possibility to use an unstructured grid. Due to the unstructured form, very complex geometries can be handled with ease [22]. This geometric flexibility is not shared by the FDM. In addition, the FVM provides a simple way of the discretization without the need to introduce generalized coordinates even when the global grid is irregular [24]. The use of the FVM is also supported by situations where the conservation laws can not be represented by PDEs, but only the integral forms are guaranteed (discontinuities, etc). However, the main problem of the FVM are difficulties in the definition of derivatives which can not be based on Taylor's expansions. The FVM becomes more complicated if it is applied to a PDE containing the second derivatives, therefore the FVM is best suitable for flow problems in primitive variables where the viscous terms are absent or are not very important [22].

The accuracy of particular methods is analyzed again in [22, 24]. As a rough guide, the use of linear approximating functions in the FEM generates solutions of about the same accuracy as the second-order FDM and the accuracy of the FEM with quadratic approximating functions is comparable with the third-order FDM [24]. The accuracy of the finite volume techniques is determined by the formulation type and can depend on irregularity of the grid. Generally, finite volume approaches are first-order or second-order accurate in space [22].

The fluid models developed in the frame of the thesis are based on the finite difference approach and the numerical solution and the implementation of the technique will be described in individual sections.

CHAPTER 3

Introduction

The sheath formation during the interaction of a plasma with a solid surface is a fundamental phenomenon of plasma science. The understanding of processes in the boundary layer between the plasma and immersed substrates is very important in probe diagnostics and in plasma based and plasma chemical technologies. In recent years, the behaviour of the sheath and presheath region has been a topic of many investigations [31–36]. The sheath structure and the sheath formation have been analyzed by many authors experimentally and theoretically and regarding the complexity of the studied problems, the computational approach is now being widely used. Moreover, the theoretical description loses its validity in some conditions (e.g. a collisional plasma at high pressures) and in that case, the computational approach proved to be the best solution.

Chapters 4–5 present a computational analysis of the plasma-solid interaction in the DC glow discharge in a low-temperature argon plasma. Plasma processes can be simulated using various computational approaches (see section 2.3). Differences between common computational techniques are connected particularly with times of the computation, the accuracy and the applicability scope. The fluid modelling is used for various kinds of problems in plasma physics. Since the fluid codes are based on solving a set of partial differential equations for macroscopic plasma quantities such as the density or average velocity, they describe the macroscopic evolution of plasma phenomena and no direct evidence about the individual particles can be obtained. The particle techniques, where the trajectories of individual particles are being traced, provide microscopic information about processes in the plasma and give more detailed insight into the plasma behaviour, but crucial demands are time requirements, especially in more dimensions.

In the scope of this thesis two groups of techniques of computational physics were applied to solve the same problem. A particle code (chapter 4) and a fluid model (chapter 5) were used to study the sheath structure and the interaction of an argon plasma with a probe for conditions of the DC glow discharge, also in the presence of an external magnetic field. Some modern plasma-based technologies employ magnetic fields and therefore the movement of charged particles in these fields is of scientific interest. The magnetic field significantly influences the sheath region, its size and shape. In addition to effects of the magnetic field, the influence of the pressure and the size of a solid surface immersed in the plasma on the sheath structure is analyzed. Chapter 6 compares results of the fluid model and the particle simulation, discusses discrepancies, reviews the applicability of both techniques and compares their time requirements.

The effort was focused on the physical aspects of plasma processes during the plasma-solid interaction and realistic assumptions about physical processes taking place in the sheath and presheath region. Besides these questions, the interest was focused on problems of computational physics such as the efficiency of computer codes. The attentions was given to the performance of the individual algorithms in two dimensions and a comparison of both computational methods was concerned.

CHAPTER 4

Two-dimensional particle-in-cell simulation

4.1 Basic features

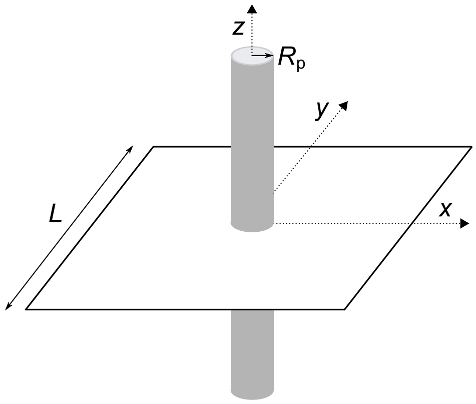

Figure 4.1: The two-dimensional computational domain $L \times L$ and a cylindrical probe with the radius R_p.

A two-dimensional particle model has been developed to simulate a problem of the interaction of a plasma and a probe embedded into the plasma. The probe is immersed into the positive column of a DC glow discharge and a small region surrounding the probe is described by the model.

A low-temperature two-component argon plasma is considered in the model presented in the thesis, however, the implementation of the model enable to simulate also a multi-component chemically active plasma. Some results for an electronegative plasma composed of electrons, positive argon ions and negative oxygen ions showing the influence of the plasma composition on the sheath structure have been published in [37].

The algorithm combines the deterministic MD simulation of the trajectories of charged plasma species (electrons and argon ions) and the stochastic MC treatment of the scattering of these particles from a neutral background. In the presented results, only elastic collisions were taken into account for the purpose of a comparison with the fluid code introduced in chapter 5, regarding that results with non-elastic atomic processes such as the ionization, recombination and excitation have been published already elsewhere [38] and the non-elastic collisions were neglected without loss of generality of the model.

The model describes the interaction of the plasma with a cylindrical probe of the infinite length. This approximation allows to reduce the dimensionality of the problem and use a two-dimensional spatial computational domain. The domain is discretized to form a grid. The Cartesian coordinate system is applied. The plasma motion is simulated in a square computational region (x,y) with the probe in the centre in the z direction perpendicular to the computational plane (Fig. 4.1).

4.2 Computational method

The charged particles are initially randomly distributed in the computational domain and a random velocity corresponding to the Maxwell velocity distribution is assigned to each particle. Although the model is two-dimensional in the spatial space, all three Cartesian components of the velocity are calculated, which is referred to as the 2D3V model. A sink of particles appears as the particles cross the boundary of the domain or as they leave the region of the simulation at the plasma-probe interface. At the external boundaries, an undisturbed plasma with the Maxwell energy distribution function both for the electrons and ions is assumed. The density of the undisturbed plasma n_0 is a parameter of the model. A source of the particles from the undisturbed plasma is simulated as the Maxwellian flux of the particles to the domain and the particles are generated with positions at the boundary. It is also possible to implement the source simply as a flux of particles from a region surrounding the computational domain in which the particles are also simulated by the MD. The velocity of these particles is Maxwellian and the particles are uniformly distributed in the region with the density n_0. In principle, however, an arbitrary velocity distribution of the particles could be used in a particle code.

Collisions of charged species with neutral atoms are treated stochastically. A frequency of the collision events is determined either by the mean free path or the mean collision frequency which are parameters of the model and they are prescribed to a constant value.

The dynamics of particles is driven by the electromagnetic force. An external electric field is not considered and the potential is calculated from the Coulomb interaction. An external magnetic field can be included into the simulation, but for the simplicity, only a magnetic field in the x direction parallel with the computational plane is involved so that the model can still be two-dimensional.

4.2.1 Molecular dynamics simulation

The temporal evolution of the system of charged plasma species is calculated by the MD technique. Initial conditions are prescribed and the time-dependent plasma behaviour is described by Newton's equations. The equations are integrated to advance the positions and velocities of the individual particles. Macroscopic parameters of the system converge to a steady-state solution describing e.g. the spatial or energy distribution of the particles in the computational region or the potential drop in the sheath which develops during the interaction of the plasma with the probe.

The numerical solution of Newton's laws of motion (section 2.3.1) is based on the Leap-frog algorithm

$$\mathbf{v}_i^{k+1/2} = \mathbf{v}_i^{k-1/2} + \frac{\mathbf{F}_i^k}{m_i}\Delta t, \tag{4.1}$$

$$\mathbf{r}_i^{k+1} = \mathbf{r}_i^k + \mathbf{v}_i^{k+1/2}\Delta t. \tag{4.2}$$

The equations are integrated for each particle (index i). The solution is updated iteratively to the new time level $t^k = t^0 + k\Delta t$ using the Leap-frog integrator and starting with initial conditions for the positions $\mathbf{r}_i^0$ at time t^0 and for the velocities $\mathbf{v}_i^{-1/2}$ at time $t^0 - \frac{1}{2}\Delta t$.

The force $\mathbf{F}$ describes the electrostatic interactions of the particles. The magnetic field is not included in the force $\mathbf{F}$. The influence of an external magnetic field can be simulated by the MD, however, a special treatment is required, because the Leap-frog integrator (4.1)–(4.2) can be applied only if the force is not a function of the velocity. The algorithm (4.1)–(4.2) can be modified to describe the motion of particles in a magnetic field when the influence of the electrostatic interaction and the magnetic field is separated in the following way

$$\mathbf{v}_i^{*} = \mathbf{v}_i^{k-1/2} + \frac{1}{2}\frac{\mathbf{F}_i^k}{m_i}\Delta t, \tag{4.3}$$

$$\mathbf{v}_i^{**} = \mathbb{R}(\mathbf{B}) \cdot \mathbf{v}_i^{*}, \tag{4.4}$$

$$\mathbf{v}_i^{k+1/2} = \mathbf{v}_i^{**} + \frac{1}{2}\frac{\mathbf{F}_i^k}{m_i}\Delta t, \tag{4.5}$$

$$\mathbf{r}_i^{k+1} = \mathbf{r}_i^{k} + \mathbf{v}_i^{k+1/2}\Delta t. \tag{4.6}$$

The equations (4.3)–(4.6) constitute the algorithm "half acceleration, rotation, half acceleration" and its formulation can be found in [7]. The influence of the magnetic field is introduced as a rotation of the velocity vector around the axis coinciding with the magnetic field direction (the operator $\mathbb{R}$). The angular velocity of the rotation corresponds to the cyclotron frequency ω_{c}.

The plasma is composed of electrons and positive argon ions. Due to significantly different masses, the dynamics of these species is governed by significantly distinct time scales. A correct solution of time-dependent problems would require to update the heavier ions using the smaller time step corresponding to the characteristic time scale of the lighter electrons. Such treatment would be computationally too intensive for conditions assumed in the presented model, therefore the dynamics of the electrons and ions is separated using a different time step Δt for each plasma species. This technique is justified when it is applied to solve a steady-state problem. The time-dependent evolution of the system is unphysical when different time steps are used for different species, while the final stationary state to which the system converges should not be affected.

4.2.2 Particle-in-cell method

The electrostatic interaction between charged particles is calculated by the particle-in-cell method. The PIC method is widely used for its straightforward implementation, particularly in plasma physics.

The computational region is discretized to form a mesh. The charge of the particles is interpolated to the mesh points using a bilinear scheme (the cloud-in-cell algorithm [6]).

The electric potential φ is calculated on the mesh points from the charge density ρ as a solution of Poisson's equation

$$\triangle\varphi = -\frac{\rho}{\epsilon_0} \tag{4.7}$$

and is fixed by Dirichlet boundary conditions. The potential is set to $\varphi = 0$ at the interface with the undisturbed plasma. The internal boundary represents an interface with a metal probe with a voltage U_p and the boundary condition imposed on the electric potential is $\varphi = U_\mathrm{p}$.

The electric field $\mathbf{E} = -\nabla\varphi$ is interpolated from the mesh points back to the particle locations (x_i,y_i) and the electric force $\mathbf{F}_i = q_i\mathbf{E}(x_i, y_i)$ required to integrate the equations of motion is obtained.

4.2.3 Algorithm for solving Poisson's equation

Poisson's equation (4.7) is discretized on the grid using the traditional five-point stencil (Fig. 4.2). The grid is equidistant in both directions $\Delta x = \Delta y = h$. The equation

$$\varphi_{i+1,j} + \varphi_{i-1,j} - 4\varphi_{i,j} + \varphi_{i,j+1} + \varphi_{i,j-1} = -\frac{\rho_{i,j}}{\epsilon_0}h^2 \tag{4.8}$$

for each nodal point (i,j) is formulated. A cylindrical probe requires to modify the equation (4.8) in the vicinity of the probe to involve the real probe shape. Distances between the grid points and the boundary defined by the cylindrical probe surface must be calculated and the discretized Poisson's equation has a general form

$$\begin{aligned} &\varphi_{i+1,j}\frac{c+d}{b} + \varphi_{i-1,j}\frac{c+d}{a} + \varphi_{i,j+1}\frac{a+b}{d} + \varphi_{i,j-1}\frac{a+b}{c} \\ -\,&\varphi_{i,j}\left(\frac{a+b}{c} + \frac{a+b}{d} + \frac{c+d}{a} + \frac{c+d}{b}\right) = \frac{e}{\epsilon_0}(n_\mathrm{e} - n_\mathrm{i})\frac{(a+b)(c+d)}{2} \end{aligned} \tag{4.9}$$

with appropriate distances a, b, c and d (Fig. 4.2). The difference scheme applied at each grid point (i,j) constitutes a system of linear equations. Two solvers of the linear system have been implemented. The system can be solved either iteratively or using the UMFPACK library [39–42].

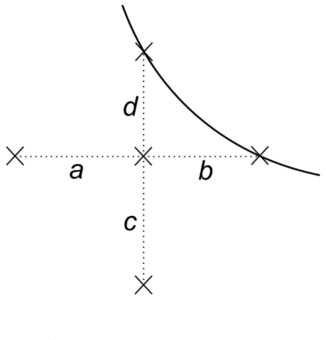

Figure 4.2: The five-point stencil.

The iterative solver is based on the successive over-relaxation (SOR) method, a fast modification of the Gauss-Seidel method. The solution is updated to the new time level $(k+1)$ in the following iterative procedure

$$\varphi^*_{i,j} = \frac{abcd}{ab+cd}\left[\frac{\varphi^k_{i+1,j}}{b(a+b)} + \frac{\varphi^k_{i-1,j}}{a(a+b)} + \frac{\varphi^k_{i,j+1}}{d(c+d)} + \frac{\varphi^k_{i,j-1}}{c(c+d)} + \frac{\rho}{2\epsilon_0}\right], \quad (4.10)$$

$$\varphi^{k+1}_{i,j} = \omega\varphi^*_{i,j} + (1-\omega)\varphi^k_{i,j}. \quad (4.11)$$

In the SOR algorithm, a parameter ω is used to speed up the convergence, which happens if the value of ω is correctly chosen. The technique and proper values of the parameter ω are specified in [43].

Although the SOR is not the strongest iterative technique, it was chosen for its simple implementation. For the sake of the efficiency, however, it is advisable to use the direct solver implemented in the UMFPACK library. The solution of systems of linear equations in UMFPACK is based on an LU decomposition solver.

4.2.4 Non self-consistent technique

The solution of Poisson's equation self-consistently with the spatial distribution or particles is the most time-consuming part of the model, particularly in two or three dimensions. The method can be much more effective if the potential is prescribed before the calculation. It can be specified analytically or computed by a different technique, e.g. the fluid modelling. Analytic formulas are given in [1] and the non self-consistent treatment of the force field is used e.g. in [44]. The presented self-consistent PIC code can be easily modified into the non self-consistent form and some results have been already published in [45].

4.3 Basic results

Input parameters of the PIC simulation are summarized in Tab. 4.1. We consider a cylindrical probe of the infinite length with the radius R_p and its axis perpendicular to the two-dimensional computational domain $L \times L$. The values of the undisturbed plasma density and the mean collision frequency corresponding to a given pressure were derived from experimental data obtained during measurements performed in the positive column of the DC glow discharge in an argon plasma.

The computational grid is uniform in both dimensions. The following results were obtained using a grid with the resolution 200 × 200 grid points and the time steps of the numerical iterations were $\Delta t_\mathrm{e} = 1 \times 10^{-11}$ s and $\Delta t_\mathrm{i} = 1 \times 10^{-8}$ s. The total number of particles in the simulation is varying

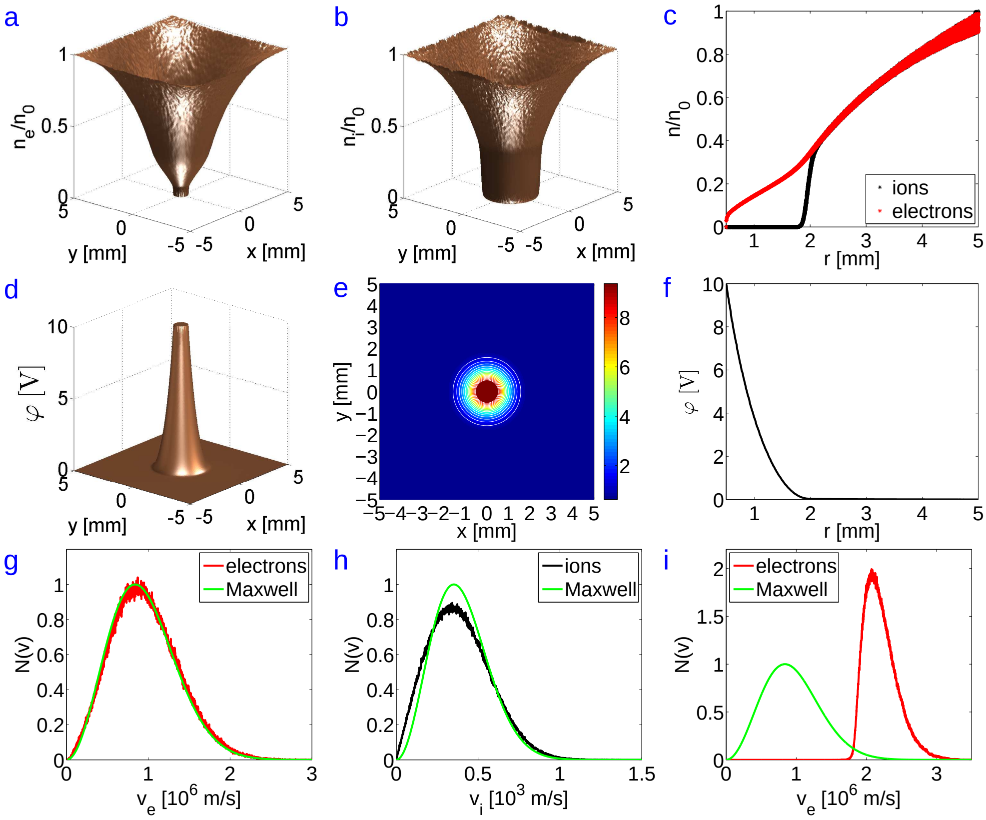

Figure 4.3: The normalized plasma density n_e/n_0 and n_i/n_0 (a, b, c), the electric potential φ [V] (d, e, f), the velocity distribution of the electrons and ions $N(v_\mathrm{e})$ and $N(v_\mathrm{i})$ in the whole region (g, h) and the electron velocity distribution $N(v_\mathrm{e})$ at the probe surface (i). $R_\mathrm{p} = 5 \times 10^{-4}$ m, $p = 1000$ Pa, $B_x = 0$ T.

parameter	**description**
$L = 0.01$ m	the size of the computational domain
$R_\mathrm{p} = 5.0 \times 10^{-4}$ m	the probe radius
$U_\mathrm{p} = 10$ V	the probe voltage
$T_\mathrm{e} = 23210$ K	the temperature of electrons
$T_\mathrm{i} = 300$ K	the temperature of argon ions
$p = 1000$ Pa	the pressure
$\overline{\nu}_\mathrm{e} = 7.8 \times 10^9$ s^{-1}	the collision frequency of electrons
$\overline{\nu}_\mathrm{i} = 3.9 \times 10^7$ s^{-1}	the collision frequency of argon ions
$n_0 = 2.7 \times 10^{15}$ m^{-3}	the density of the undisturbed plasma

Table 4.1: Parameters of the model.

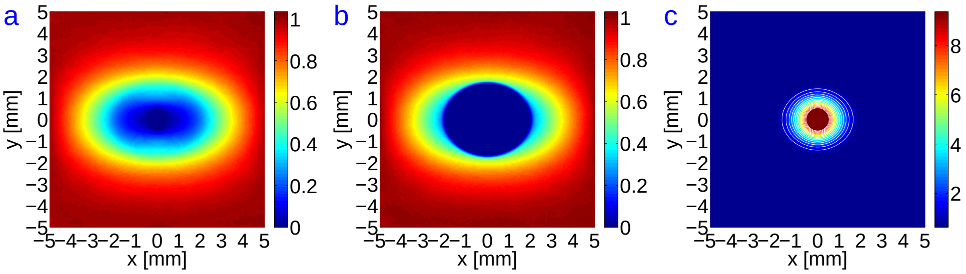

Figure 4.4: The normalized electron density n_{e}/n_0 (a), the normalized ion density n_{i}/n_0 (b) and the electric potential φ [V] (c). $R_{\mathrm{p}} = 5 \times 10^{-4}$ m, $p = 1000$ Pa, $B_x = 0.1$ T.

as the particles leave or enter the domain. The simulations were started with 6×10^6 charged particles.

The results of the simulation with the parameters specified in Tab. 4.1 are shown in Fig. 4.3. The distribution of the plasma density and electric potential in the computational domain is symmetric around the probe axis. The radial dependence of the plasma density in the presheath region is logarithmic, which is predicted also by a simple theoretical model – the analytic solution of the diffusion equation (see section 6.1), and which is also in agreement with experimental investigations. In the vicinity of the probe, the sheath region develops with a significant potential drop. The quasi-neutrality condition is not fulfilled, the electrons are attracted towards the positively biased probe and the electron density is higher than the density of the ions $n_{\mathrm{e}} > n_{\mathrm{i}}$ (Fig. 4.3 c). Let us remark that Fig. 4.3 is a result of a two-dimensional calculation. The values in each grid position (i,j) are plotted in Fig. 4.3 c. It causes the vertical spread of the plasma density becoming significant at the end due to imposing the boundary condition on a square computational domain. The distance r ranges from the probe surface $r = 0.5$ mm to the end of the computational domain $r = 5$ mm.

The plasma distribution in the sheath and presheath region and the velocity distributions of the electrons and ions are influenced by collision processes. Only elastic scattering of charged particles from neutrals was taken into account here. Fig. 4.3 g and h show the velocity distribution of the electrons and ions in the simulated region. The electron distribution coincides well with the Maxwell velocity distribution function, while the ions are not precisely Maxwellian as a result of collisions. There are various ways how collisions can be implemented in a particle code. Possible treatments of the collision processes and their influence on the energy distribution function are discussed in [46] where an improved approach for the ions is described. Here the treatment of the collisions in not the main subject of interest.

Besides the atomic processes, the sheath structure and formation is affected by the magnetic field. The simulation in Fig. 4.4 was carried out assuming a constant external magnetic field in the direction of the x axis $\mathbf{B} = (B_x, 0, 0)$. The effect of the magnetic field is clearly illustrated. The shape of the sheath region is elongated in the x direction parallel with the magnetic field, and the perturbed region has an elliptic form in two dimensions. More results will be presented and discussed in chapter 6.

CHAPTER 5

Two-dimensional fluid model

The physical aspects of any fluid flow are governed by three fundamental principles – the mass, momentum and energy conservation. In plasma physics, some of the authors [16, 48] simplify the momentum equation and use the drift-diffusion approximation (section 2.3.3) for modelling of the plasma-solid interaction. Compared to this standard approach, the model presented here aims to solve the full momentum equation. The model has been also implemented in COMSOL Multiphysics [49] where a model using the drift-diffusion equation has been successfully solved before [38]. However, the convergency for the full model in COMSOL Multiphysics was not maintained and no stable solution has been obtained.

5.1 Fluid description and governing equations

The mathematical description of a plasma flow in the fluid modelling is based on a model governed by partial differential equations describing macroscopic plasma parameters such as the density n and the average velocity $\mathbf{u}$. The governing PDEs can be derived taking velocity moments of the Boltzmann equation (section 2.3.3). A practical use of the fluid approach for a plasma is not based on the general form of the equations as they can be derived from the Boltzmann equation and various approximations are commonly considered. In this computational study, we use the following system of the conservation laws describing a transport of the mass and momentum for each plasma species (electrons k=e and ions k=i)

$$\frac{\partial n_{\mathrm{k}}}{\partial t} + \nabla \cdot (n_{\mathrm{k}} \mathbf{u}_{\mathrm{k}}) = 0, \tag{5.1}$$

$$m_{\mathrm{k}} n_{\mathrm{k}} \frac{\partial \mathbf{u}_{\mathrm{k}}}{\partial t} + m_{\mathrm{k}} n_{\mathrm{k}} (\mathbf{u}_{\mathrm{k}} \cdot \nabla) \mathbf{u}_{\mathrm{k}} = q_{\mathrm{k}} n_{\mathrm{k}} (\mathbf{E} + \mathbf{u}_{\mathrm{k}} \times \mathbf{B}) - \nabla p_{\mathrm{k}} - m_{\mathrm{k}} n_{\mathrm{k}} \overline{\nu}_{\mathrm{k}} \mathbf{u}_{\mathrm{k}}. \tag{5.2}$$

The quantities in the equations (5.1) and (5.2) have their usual meaning – the density n, the average velocity $\mathbf{u}$, the pressure p, the mean collision frequency $\overline{\nu}$, the mass m, the charge q, the electric and magnetic fields $\mathbf{E}$ and $\mathbf{B}$. The continuity and momentum equations (5.1) and (5.2) are supplemented with Poisson's equation for the electric potential φ

$$\triangle\varphi = \frac{e}{\epsilon_0}(n_{\mathrm{e}} - n_{\mathrm{i}}). \tag{5.3}$$

We assume a constant temperature of the electrons and ions, the scalar pressure $p_{\mathrm{k}} = n_{\mathrm{k}} k T_{\mathrm{k}}$ and a constant collision frequency $\overline{\nu}_k$. Viscous effects are neglected and we do not solve for the energy balance. The source terms are simplified due to the assumption of elastic collisions, non-elastic collisions such as the excitation and ionization are neglected. A fluid model with more precise treatment of the collisions considering the non-elastic scattering and including the energy equation is presented in [38], however, on the other hand, the model described in [38] has other constraints. Compared to other papers where the momentum equation is simplified, this model works with the full momentum equation. It is usual, under certain assumptions being fulfilled, to cancel the inertial and convective term of the equation (5.2). The simplified momentum equation is of an algebraic form and describes a flux composed of the drift and the diffusion, see the equation (2.20). In such a case, Scharfetter-Gummel scheme [23, 50] is commonly proposed to solve the continuity equation which is a PDE of the convection-diffusion type.

5.2 Computational method

The system of equations (5.1)–(5.3) is solved using the finite difference approach. The equations are discretized on a regular rectangular grid (i,j) with a uniform grid spacing in both dimensions.

5.2.1 Poisson solver

The electric potential φ is calculated on the grid points as a solution of Poisson's equation (5.3). The equation (5.3) is discretized on the grid with the five-point stencil using central differences for spatial derivatives, similarly as in chapter 4. The resulting system of linear equations can be solved by the UMFPACK library or by the SOR method.

5.2.2 Transport equations

The fluid equations (5.1) and (5.2) can be written in a general form

$$\frac{\partial f}{\partial t} + \frac{\partial}{\partial x}(f v_x) + \frac{\partial}{\partial y}(f v_y) = S \tag{5.4}$$

for the quantity $f = (n, u_x, u_y)$ and with the advective velocity $\mathbf{v} = (v_x, v_y)$ and a source S. The same form of the continuity and momentum equation allows us to apply the same method of solution and the equations (5.1) and (5.2) can be discretized in a similar way. The numerical algorithm is based on the flux-corrected transport (FCT) scheme and the solution is being updated to converge to a steady state with a time step Δt.

The numerical implementation of the FCT technique involves three steps – an advection, a diffusion and an anti-diffusion. To update the solution, any traditional high-order numerical scheme can be used. The two-step Lax-Wendroff discretization [51] is implemented here. Basically, it uses Lax-Friedrichs steps to construct solution values at intermediate points and there are various ways how the method can be formulated in two dimensions. Let us assume a source-free advection equation for a function f

$$\frac{\partial f}{\partial t} + \frac{\partial F}{\partial x} + \frac{\partial G}{\partial y} = 0 \tag{5.5}$$

solved on an equidistant Cartesian grid with a uniform grid spacing $\Delta x = \Delta y = h$. The algorithm assumes that the flow variable f is transported to the next time level using the following difference form

$$f_{i,j}^{k+1} = f_{i,j}^{k} - \frac{\Delta t}{h}\left(F_{i+1/2,j}^{k+1/2} - F_{i-1/2,j}^{k+1/2}\right) - \frac{\Delta t}{h}\left(G_{i,j+1/2}^{k+1/2} - G_{i,j-1/2}^{k+1/2}\right) \tag{5.6}$$

where the fluxes $F = F(f)$ and $G = G(f)$ are obtained at the intermediate time level $(k + \frac{1}{2})$ according to a formula involving the Lax-Friedrichs scheme

$$\begin{aligned} f_{i+1/2,j}^{k+1/2} = {} & \frac{1}{4}\left(f_{i,j}^{k} + f_{i+1,j}^{k} + f_{i+1/2,j-1/2}^{k} + f_{i+1/2,j+1/2}^{k}\right) \\ & - \frac{\Delta t}{2h}\left(F_{i+1,j}^{k} - F_{i,j}^{k}\right) - \frac{\Delta t}{2h}\left(G_{i+1/2,j+1/2}^{k} - G_{i+1/2,j-1/2}^{k}\right) \end{aligned} \tag{5.7}$$

and in a similar manner for the remaining intermediate points. In the equations (5.6) and (5.7), $F_{i,j}^{k}$ expresses $F(f_{i,j}^{k})$ and so on. The diffusive flux D is then computed using a diffusivity coefficient η

$$D_{i+1/2,j}^{k} = \eta\left(f_{i+1,j}^{k} - f_{i,j}^{k}\right) \tag{5.8}$$

and analogically at the remaining points and the solution is advanced

$$f_{i,j}^{k+1} = f_{i,j}^{k+1} + D_{i+1/2,j}^{k} - D_{i-1/2,j}^{k} + D_{i,j+1/2}^{k} - D_{i,j-1/2}^{k}. \tag{5.9}$$

The final step to update the solution to the next time level is to anti-diffuse the solution using a flux limiter

$$f_{i,j}^{k+1} = f_{i,j}^{k+1} - L_{i+1/2,j}^{k+1} + L_{i-1/2,j}^{k+1} - L_{i,j+1/2}^{k+1} + L_{i,j-1/2}^{k+1}. \tag{5.10}$$

The flux limiter L is calculated using the formula

$$L_{i+1/2,j}^{k+1} = S_{i+1/2,j} \max\left\{0, \min\left\{c_1, c_2, c_3\right\}\right\} \tag{5.11}$$

where c_1, c_2 and c_3 are defined as

$$c_1 = S_{i+1/2,j}\left(f_{i,j}^{k+1} - f_{i-1,j}^{k+1}\right), \tag{5.12}$$

$$c_2 = S_{i+1/2,j}\left(f_{i+2,j}^{k+1} - f_{i+1,j}^{k+1}\right), \tag{5.13}$$

$$c_3 = |A_{i+1/2,j}^{k+1}| \tag{5.14}$$

and

$$A_{i+1/2,j}^{k+1} = \eta\left(f_{i+1,j}^{k+1} - f_{i,j}^{k+1}\right) \tag{5.15}$$

is the anti-diffusive flux computed using the updated solution $f_{i,j}^{k+1}$ from the equation (5.6). The factor $S_{i+1/2,j}$ is 1 or -1 according to the following condition

$$S_{i+1/2,j} = \begin{cases} +1 & A_{i+1/2,j}^{k+1} \geq 0 \\ -1 & A_{i+1/2,j}^{k+1} < 0 \end{cases}. \tag{5.16}$$

The diffusivity coefficient η in the equations (5.8) and (5.15) is calculated automatically in the code with a primary purpose to smooth oscillations that can occur in the numerical solution and its magnitude depends on the advective velocity, time step and grid spacing

$$\eta = \frac{\epsilon}{(1+2\epsilon)^2}, \tag{5.17}$$

$$\epsilon = \max\left(v_{i,j}\frac{\Delta t}{h}\right). \tag{5.18}$$

The FCT method is a high-order monotone and conservative scheme and it is second-order accurate in general. The whole procedure enables to smooth oscillations arising in the numerical solution and to resolve steep gradients. The implementation follows the algorithm presented in [52] and a detailed description of the FCT and its important properties are pointed out in [53, 54]. As an extension of the mathematical summary given above, appropriate boundary conditions were applied again, thus the difference schemes were properly modified at the probe boundary to involve the boundary conditions correctly with respect to the curved probe surface. The technique was further advanced to handle the source term S of the equation (5.4), but the basic algorithm still follows the described form. To evolve the solution of a system of the form (5.4) numerically, it is usually possible to treat the influence of the source term separately from the influence of the convective terms. The source term was treated implicitly here.

5.2.3 Boundary conditions

The two-dimensional model of the plasma-probe interaction assumes a square computational domain (x,y) and a cylindrical probe of the infinite length in the z direction with a positive voltage U_p (Fig. 4.1). The boundary conditions for this problem imposed on the density, velocity and electric potential are summarized in Tab. 5.1. Similar boundary conditions were used in [21]. The problem is fixed by Dirichlet boundary conditions for the electric potential, assuming a biased electrode with the voltage U_p and an undisturbed quasineutral plasma on the exterior of the computational domain. A Dirichlet boundary condition is also used for the plasma density at the outer boundary by setting the density to an experimental value of the undisturbed plasma density. All the other conditions are kept open, i.e. we extrapolate the values from nearest grid points inside the computational region to the boundary.

	exterior (undisturbed plasma)	**interior** (solid surface)
n_e	Dirichlet ($n_\mathrm{e} = n_0$)	open (extrapolation from the interior of the domain)
n_i	Dirichlet ($n_\mathrm{i} = n_0$)	Dirichlet ($n_\mathrm{i} = 0$)
$\mathbf{u}_\mathrm{e}$	open	open
$\mathbf{u}_\mathrm{i}$	open	open
φ	Dirichlet ($\varphi = 0$)	Dirichlet ($\varphi = U_\mathrm{p}$)

Table 5.1: Boundary conditions.

5.3 Basic results

Parameters of the fluid model are specified in Tab. 5.2 and they are identical with the parameters of the particle simulation in section 4.3.

parameter	**description**
$L = 0.01$ m	the size of the computational domain
$R_{\mathrm{p}} = 5.0 \times 10^{-4}$ m	the probe radius
$U_{\mathrm{p}} = 10$ V	the probe voltage
$T_{\mathrm{e}} = 23210$ K	the temperature of electrons
$T_{\mathrm{i}} = 300$ K	the temperature of argon ions
$p = 1000$ Pa	the pressure
$\overline{\nu}_{\mathrm{e}} = 7.8 \times 10^{9}$ s^{-1}	the collision frequency of electrons
$\overline{\nu}_{\mathrm{i}} = 3.9 \times 10^{7}$ s^{-1}	the collision frequency of argon ions
$n_0 = 2.7 \times 10^{15}$ m^{-3}	the density of the undisturbed plasma

Table 5.2: Parameters of the model.

The computational grid used in the fluid code is uniform and the time stepping is automatic and it is governed by the Courant-Friedrichs-Lewy (CFL) stability criterion [22]. For the simulation without an external magnetic field (Fig. 5.1) and the parameters specified in Tab. 5.2, the values $\Delta t_{\mathrm{e}} = 2 \times 10^{-11}$ s and $\Delta t_{\mathrm{i}} = 8.5 \times 10^{-9}$ s satisfy the stability conditions in the steady state, comparably the same values as in the PIC code for the simulation in Fig. 4.3. The simulation in Fig. 5.1 was carried out with the resolution 800 × 800 grid points and only elastic collisions were considered. Fig. 5.1 shows the distribution of the electrons and ions in the computational domain, the electric potential and the mean velocity of the charged particles for a case without the magnetic field.

The effect of an external magnetic field is illustrated in Fig. 5.2 and described further in the following chapter where also a comparison of the fluid and particle approach is discussed. Note that the results in Fig. 5.2 were produced with a different strength of the magnetic field than the results of the PIC simulation in Fig. 4.4, provided that for strong magnetic fields, stability problems occurred.

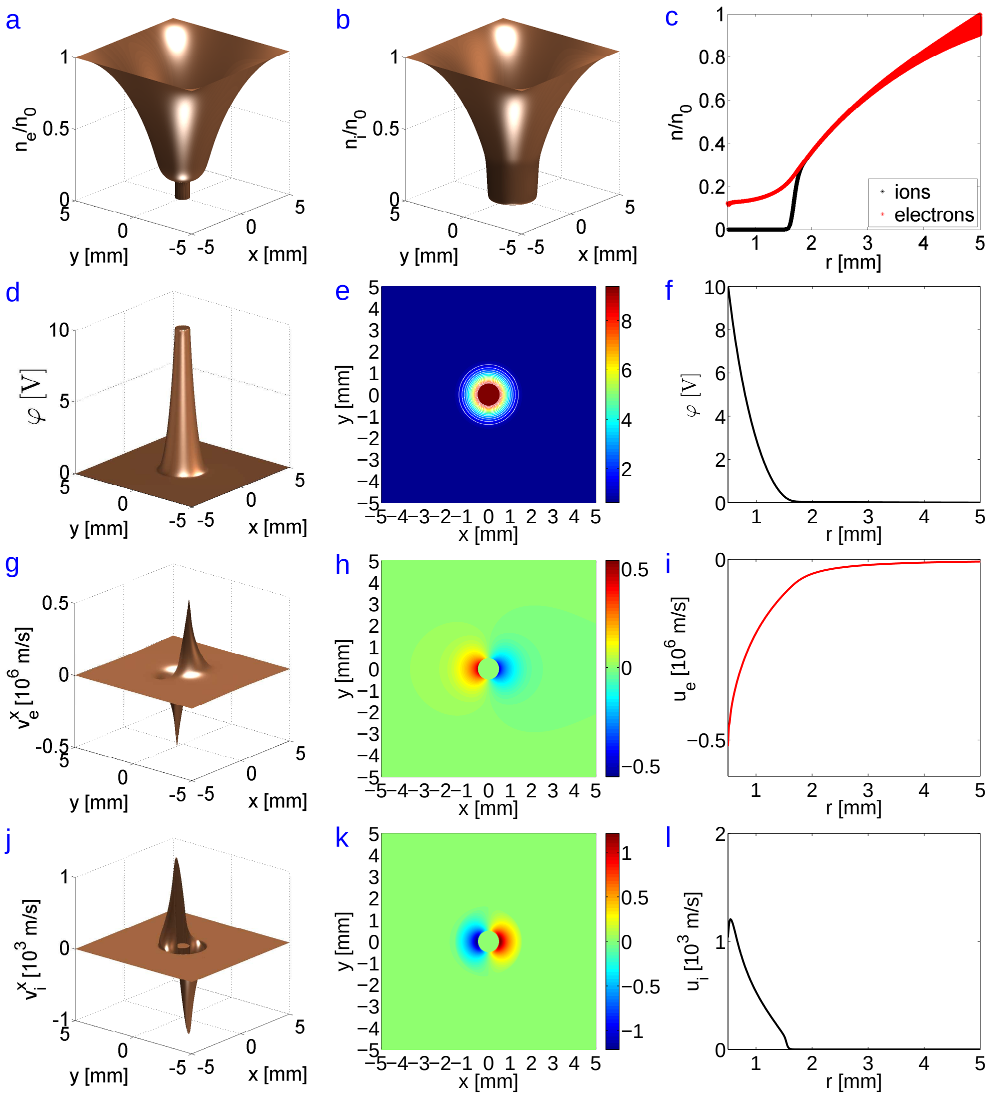

Figure 5.1: The normalized plasma density n_{e}/n_0 and n_{i}/n_0 (a, b, c), the electric potential φ [V] (d, e, f), the x component of the average electron velocity u_{e}^x [10^6 m/s] (g, h), the magnitude of the average electron velocity u_{e} [10^6 m/s] (i), the x component of the average ion velocity u_{i}^x [10^3 m/s] (j, k) and the magnitude of the average ion velocity u_{i} [10^3 m/s] (l). $R_{\mathrm{p}} = 5 \times 10^{-4}$ m, $p = 1000$ Pa, $B_x = 0\,$T.

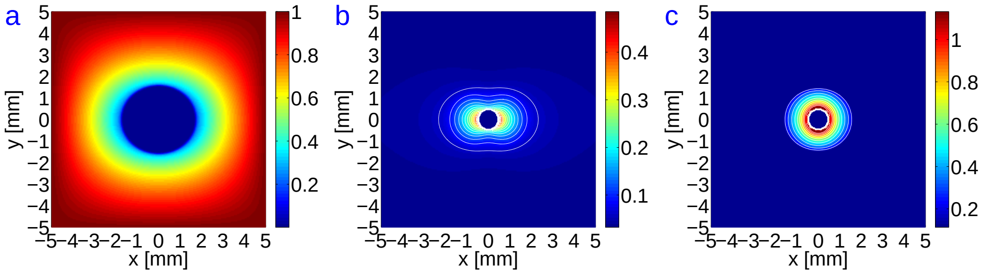

Figure 5.2: The normalized ion density n_i/n_0 (a), the average velocity of the electrons u_e [10^6 m/s] (b) and the average velocity of the ions u_i [10^3 m/s] (c). $R_\mathrm{p} = 5 \times 10^{-4}$ m, $p = 1000$ Pa, $B_x = 0.001$ T.

CHAPTER 6

Results

The sheath formation in the vicinity of a solid surface and the structure of the sheath is influenced by various physical processes, the composition of the plasma or the geometry of the immersed solid substrate. Chapter 6 summarizes effects of collisions, an external magnetic field, the pressure and the probe size on the sheath size and shape and on the distribution of charged particles in the sheath and presheath region. Some results have been already published in [37, 55]. The results calculated by the fluid and particle approach slightly differ, however, both techniques give the same results in qualitative sense concerning the influence of various parameters. A comparison of both approaches follows in section 6.5.

6.1 Influence of collisions

Properties of the sheath are influenced by collision processes. The collisions of charged particles with neutral atoms influence the thickness of the sheath and the spatial and velocity distribution of the charged particles in the sheath and presheath region. The effect can be deduced from Fig. 6.1 which compares results of three simulations. The first simulation involves only elastic scattering, the second simulation was calculated with non-elastic collisions (such as the excitation and ionization) using energy dependent cross-sections and the results of the third simulation were obtained for a collisionless case. In all cases, the same mean collision frequencies were used. The treatment of the non-elastic atomic processes was based on data presented in [56].

Radial profiles of the plasma density are compared with an analytic solution of the diffusion equation for these specific cases. The diffusion equation is written in cylindrical coordinates

$$\frac{\partial^2 n}{\partial r^2} + \frac{1}{r}\frac{\partial n}{\partial r} = 0 \qquad (6.1)$$

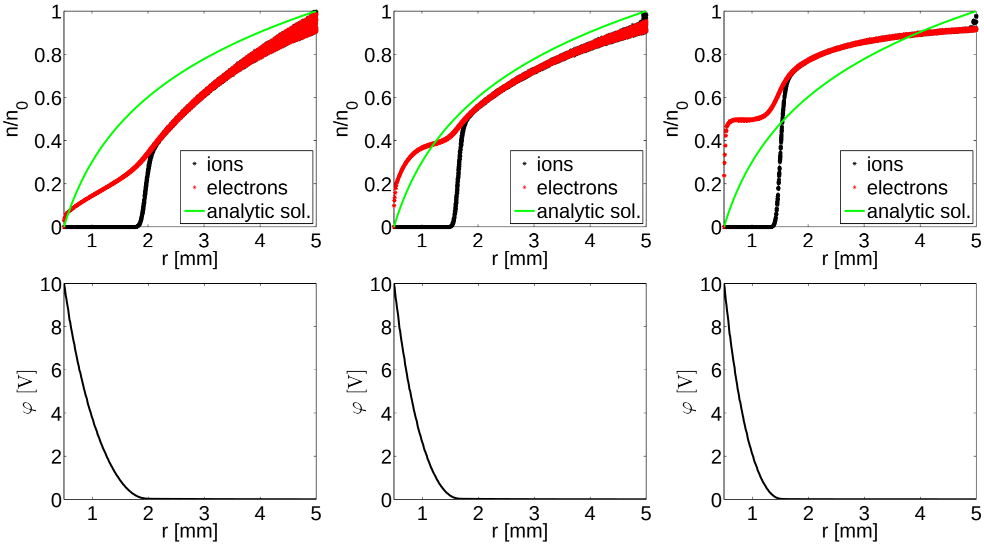

Figure 6.1: The radial dependence of the normalized plasma density n/n_0 (up) and the electric potential φ [V] (down) for a simulation with elastic scattering (left), a simulation with non-elastic collisions (middle) and a collisionless case (right). $R_\mathrm{p} = 5 \times 10^{-4}$ m, $p = 1000$ Pa, $B_x = 0$ T. Results of the PIC simulation.

and the coefficients a and b of the solution

$$n = a \ln r + b \tag{6.2}$$

are obtained applying boundary conditions $n = 0$ at the probe surface and $n = n_0$ at the outer boundary. The most realistic case with the non-elastic collisions is close to match the analytic solution. For the elastic scattering, which is realized as a random change of the velocity direction of a particle, the plasma density is lower than the analytic solution and the point of the charge separation is shifted below the analytic curve. It is important, however, that the result of the fluid model (Fig. 5.1 c) where only the elastic collisions are considered is close to the PIC result in Fig. 6.1 on the left.

6.2 Influence of pressure

Fig. 6.2 shows results of the fluid model at different pressures. At higher pressures, the plasma density is higher, collisions of electrons and ions with neutrals are more frequent and the width of the sheath region is smaller. The effect of the pressure on the sheath width corresponds quantitatively to the expression (2.2) in chapter 2. The values of the undisturbed plasma density n_0 and the mean collision frequencies $\overline{\nu}_\mathrm{e}$ and $\overline{\nu}_\mathrm{i}$ were derived experimentally and they are following: $n_0 = 1.9 \times 10^{15}$ m^{-3}, $\overline{\nu}_\mathrm{e} = 3.9 \times 10^9$ s^{-1} and $\overline{\nu}_\mathrm{i} = 2.0 \times 10^7$ s^{-1} for $p = 500$ Pa, $n_0 = 2.7 \times 10^{15}$ m^{-3}, $\overline{\nu}_\mathrm{e} = 7.8 \times 10^9$ s^{-1} and $\overline{\nu}_\mathrm{i} = 3.9 \times 10^7$ s^{-1} for $p = 1000$ Pa and $n_0 = 3.9 \times 10^{15}$ m^{-3}, $\overline{\nu}_\mathrm{e} = 1.6 \times 10^{10}$ s^{-1} and $\overline{\nu}_\mathrm{i} = 7.8 \times 10^7$ s^{-1} for $p = 2000$ Pa.

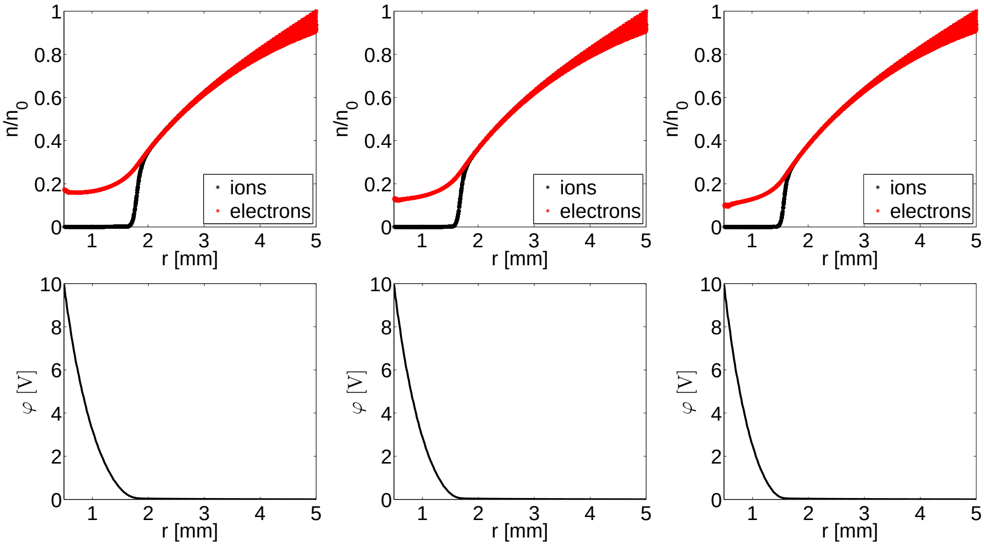

Figure 6.2: The radial dependence of the normalized plasma density n/n_0 (up) and the electric potential φ [V] (down) for $p = 500$ Pa (left), $p = 1000$ Pa (middle) and $p = 2000$ Pa (right). $R_\mathrm{p} = 5 \times 10^{-4}$ m, $B_x = 0$ T. Results of the fluid model.

6.3 Influence of magnetic field

It was already shown in the previous chapters that an external magnetic field influences the sheath shape and elongation. If the magnetic field is parallel with the x axis, the perturbed region is extended in the x direction. The elongation obviously depends on the strength of the magnetic field (Fig. 6.3).

For a collisionless case, even weak magnetic fields show a strong effect. In a weakly ionized low-temperature plasma, collisions of charged particles with neutrals become important and suppress the influence of the magnetic field. The combined effect of the magnetic field and the pressure (Fig. 6.4) shows that the influence of the magnetic field is not so significant at higher pressures as the plasma is denser and the charged particles collide with the neutrals more often. It should be stated that for a collisionless plasma in the presence of a magnetic field, it is characteristic to observe perturbations of the sheath and presheath region relatively far from the solid surface. In case

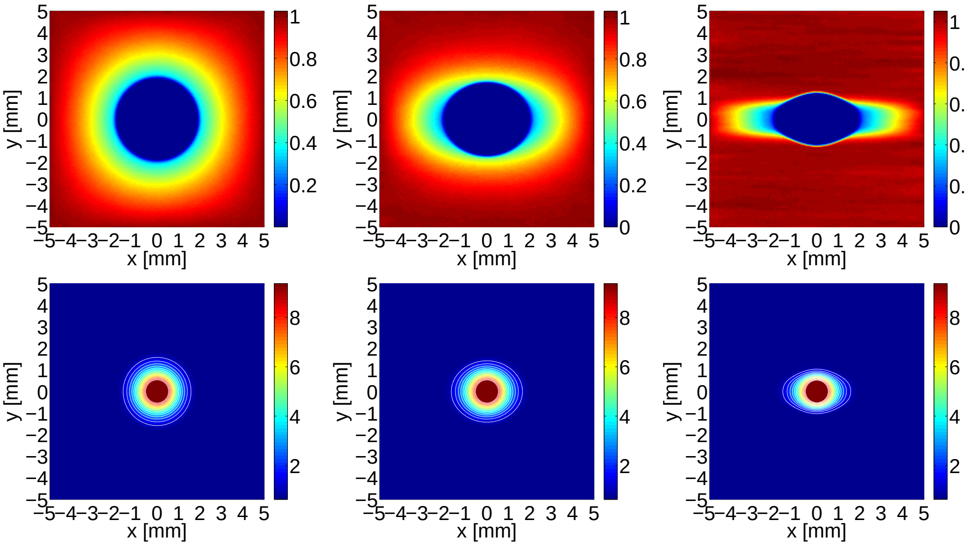

Figure 6.3: The distribution of the ion density n_i/n_0 (up) and the electric potential φ [V] (down) for $B_x = 0.01$ T (left), $B_x = 0.1$ T (middle) and $B_x = 1$ T (right). $R_\mathrm{p} = 5 \times 10^{-4}$ m, $p = 1000$ Pa. Results of the PIC simulation.

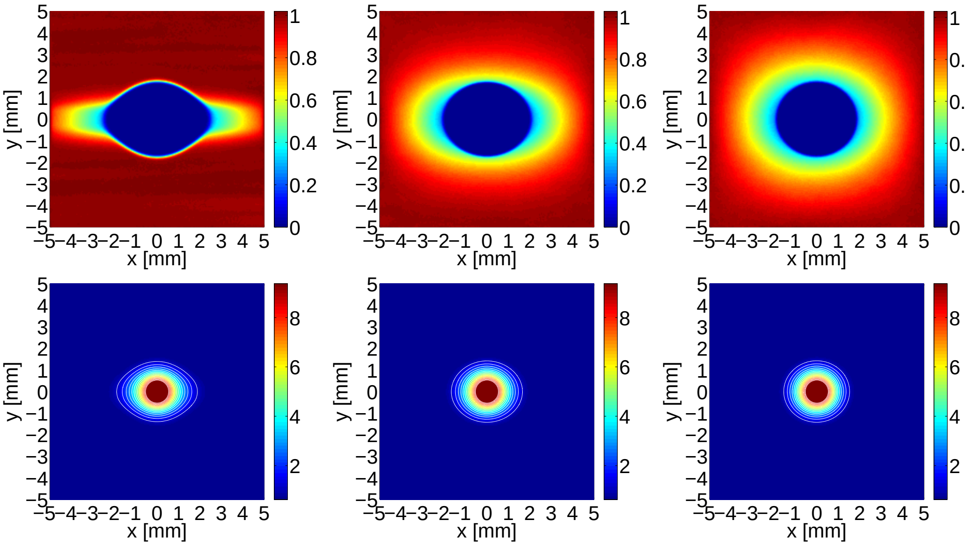

Figure 6.4: The distribution of the ion density n_i/n_0 (up) and the electric potential φ [V] (down) for $p = 100$ Pa (left), $p = 1000$ Pa (middle) and $p = 2000$ Pa (right). $R_\mathrm{p} = 5 \times 10^{-4}$ m, $B_x = 0.1$ T. Results of the PIC simulation.

of such strong extension of the sheath shape by the magnetic field, the ratio of the width of the perturbed region in the direction of the magnetic field lines and in the perpendicular direction can be even one order of magnitude.

6.4 Influence of geometry

Besides physical processes in the plasma, the sheath width and the potential drop correspond to the geometry of the embedded probe, its size and shape. Only the cylindrical geometry is involved here. Fig. 6.5 shows radial profiles of the plasma density and the potential distributions and their dependence on the probe radius. With increasing radius, the electron density on the probe surface decreases and the sheath region becomes larger. The third case in Fig. 6.5 is a result for the planar geometry and it was calculated by a one-dimensional fluid model as a limit case with $R_{\mathrm{p}} \to \infty$.

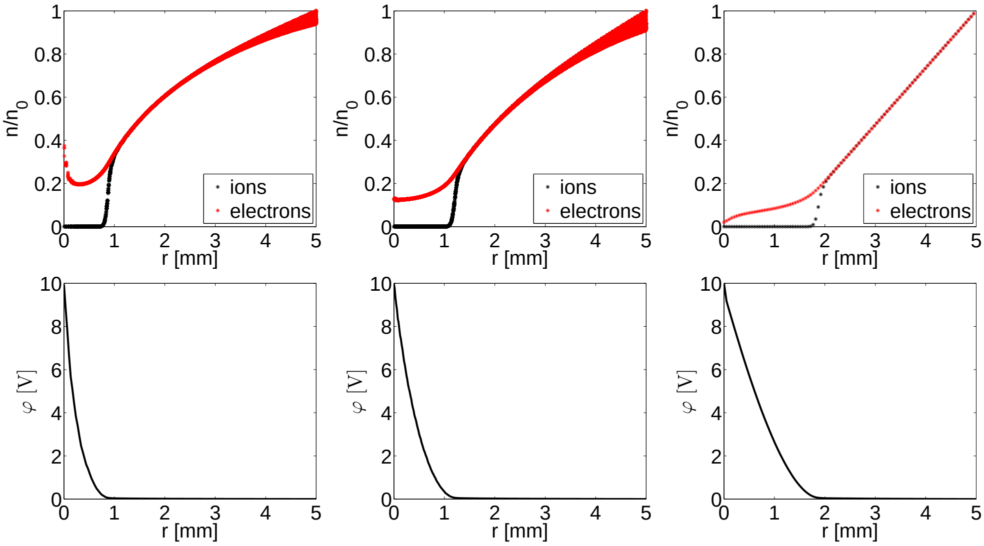

Figure 6.5: The radial dependence of the normalized plasma density n/n_0 (up) and the electric potential $\varphi\,[\mathrm{V}]$ (down) for $R_{\mathrm{p}} = 1 \times 10^{-4}\,\mathrm{m}$ (left), $R_{\mathrm{p}} = 5 \times 10^{-4}\,\mathrm{m}$ (middle) and a planar probe (right). $p = 1000$ Pa, $B_x = 0$ T. Results of the fluid model. A comment – to compare results for different probe radii, the distance r ranges here from the probe surface where $r = 0$ to the end of the computational region where $r = 5$ mm. The size of the domain in the two-dimensional model is then $L = 2R_{\mathrm{p}} + 10$ mm.

In a real plasma, the density saturates to the undisturbed plasma density n_0 at a certain distance from the solid surface. The model is an approximation where the undisturbed plasma conditions are fixed by boundary conditions at the outer boundary of the computational region. The size of the region L then determines the radial profile of the plasma density. Fig. 6.6 indicates that as the sheath becomes smaller for a larger computational region, the plasma density distribution matches the analytic solution better. It could be deduced that the disagreement of the solution with the analytic one comes mainly from the sheath, while in the presheath, the solution would coincide with the analytic curve. An explanation might be following. In the sheath region, the probe repels the ions and accelerates the electrons. The velocity distribution of the particles in the sheath is not Maxwellian due to the presence of a strong potential drop. Also collisions influence the velocity distribution and the assumption of a constant temperature and energy-independent collision frequencies is not valid. The energy distribution function surely affects the spatial distribution of the particles in the sheath and the radial profile of the plasma density. In [57], a fluid model is presented, in which the mean collision frequency is not constant, the energy dependence is evaluated and the result matches the analytic solution precisely. Further, the mean collision frequencies were obtained from measurements in a real plasma where also non-elastic collisions are present. Therefore it is possible that the rates of the elastic collisions are overestimated and the frequency should be actually lower than the frequency in the plasma where the non-elastic events are not neglected.

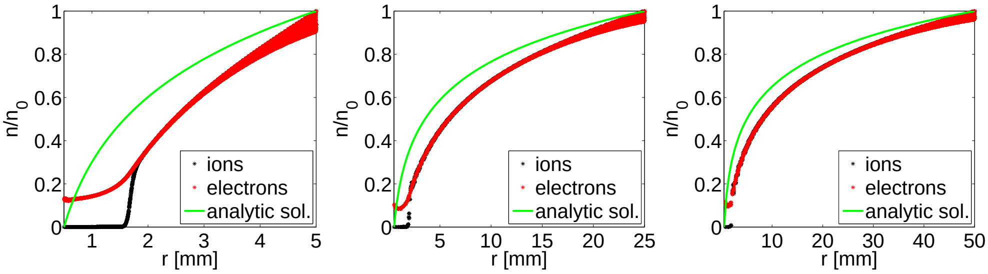

Figure 6.6: The radial dependence of the normalized plasma density n/n_0 for $L = 0.01$ m (left), $L = 0.05$ m (middle) and $L = 0.1$ m (right). $R_\mathrm{p} = 5 \times 10^{-4}$ m, $p = 1000$ Pa, $B_x = 0$ T. Results of the fluid model.

6.5 Discussion and comparison

The results of the fluid model (Fig. 5.1 and 5.2) have the same character as the results of the particle simulation (Fig. 4.3 and 4.4), especially the radial profiles of the density in the presheath coincide for the fluid model (Fig. 5.1 c) and for the particle model with elastic collisions (Fig. 4.3 c), while results of the PIC code with non-elastic collisions or for a collisionless case (Fig. 6.1) show a higher discrepancy compared to the fluid approach.

The influence of the magnetic field and other parameters on the sheath structure is qualitatively the same for both techniques, however, we have not achieved exact agreement in the quantitative sense. The sheath region is slightly larger in the PIC result (Fig. 4.3 c) and the electron density at the probe surface in the fluid result (Fig. 5.1 c) is higher than in Fig. 4.3 c. In the fluid approach, the boundary conditions characterize the steady-state solution and the particle flux at the probe surface is determined by conditions imposed on the plasma density and velocity. Some authors use Dirichlet boundary conditions $n_\mathrm{e} = 0$ and $n_\mathrm{i} = 0$ on the solid surface [30] and a different approach ($\mathbf{\Gamma}_\mathrm{e} \cdot \mathbf{n} = -n_\mathrm{e}\mu_\mathrm{e}E + \frac{1}{4}v_\mathrm{e}^\mathrm{th}n_\mathrm{e}$) is used e.g. in [58, 59]. Here the boundary conditions listed in Tab. 5.1 were applied, similarly as in [21]. Using these conditions, we have obtained smaller velocity of the electrons at the probe surface than in the particle simulation (compare Fig. 4.3 i and Fig. 5.1 i) and thus higher electron density.

For a given probe, there are two main parameters of the model controlling the thickness of the sheath and its extension in a magnetic field. Obviously, the first one is the strength of the magnetic field (Fig. 6.3) and the second parameter is the pressure or collision processes in general (Fig. 6.4 and 6.1). The treatment of collisions between charged particles and a neutral background is always inconsistent in the fluid description and in the particle model even for the same value of the collision frequency. The particle approach is based on the microscopic description and the scattering of the particles is simulated using the mean free path or the mean collision frequency. In the fluid code, we solve a set of partial differential equations with the collision frequency as a coefficient.

Concerning the question of the collision processes, the fluid description can be advanced and the atomic processes and collisions can be treated in a way similar to the particle code using the hybrid approach. A hybrid model, which is partly based on the fluid approach and partly on the particle technique, was introduced in [4] and used also in [60]. The fluid code in [60] is coupled with a non self-consistent particle code that simulates the trajectories of particles microscopically. The particle simulation does not solve for the electric potential and uses the electric potential calculated by the fluid code. Since the Poisson solver in the PIC method is the most intensive part of the particle simulation, the hybrid approach is more effective than a self-consistent particle technique. The particle part of the calculation combines a Molecular dynamics simulation of the trajectories of charged particles and the stochastic Monte Carlo treatment of the scattering of these particles from a neutral background. The Monte Carlo algorithm computes values of the reaction rate coefficients which are sent back to the fluid code. This procedure makes it possible to converge the collision processes in each time step when we run the scheme iteratively. Such method allows an inclusion of the collisions in the fluid description that is consistent with the particle approach. Applying this technique, the effect of collisions on the sheath structure should be in agreement with the self-consistent particle simulation and the discrepancy between the fluid and the particle approach might be further decreased. The described method is nevertheless beyond the scope of this thesis and it was a subject of interest in [60]. Here we focus on other aspects – the implementation of the fluid model, the solution of the full momentum equation, the choice of boundary conditions, the inclusion of the magnetic field into the models, etc.

In the presence of a magnetic field, the size and the extension of the sheath and presheath region can strongly depend on properties of the plasma and processes in the boundary layer. Fig. 6.4 demonstrates the effect of the pressure which determines the density and the rate of scattering events. It is characteristic that the perturbation caused by the magnetic field affects the concentrations of charged particles more significantly than the electric potential. It should be remarked that the fluid model presented here uses the assumption of the undisturbed plasma as the boundary condition on the exterior of the domain and prescribes the boundary value of the density to the undisturbed value n_0. In certain conditions, the sheath and presheath region in the presence of a magnetic field can be significantly extended along the magnetic field (see e.g. Fig. 6.4 on the left) compared to the perturbation perpendicular to the magnetic field (typical for a collisionless plasma where the elongation along the magnetic field lines can be even ten times larger than in the perpendicular direction). In such a case, the perturbed zone could extend enough to be far outside the computational domain and the assumption of the undisturbed plasma at the exterior boundary would not be valid anymore. Then the boundary condition imposed on the density should be correctly selected or the size and the form of the considered simulated region should be modified, e.g. using a rectangular region instead of the square one that would correspond to physical conditions and describe better the geometry of the problem.

The efficiency of the codes depends on considered physical aspects such as the magnetic field strength or the pressure. In addition, the influence of the physical conditions on the code performance can be of a different character in the two approaches. Specifically, in the particle simulation, one time step takes longer at higher pressures as the pressure determines the rate with which individual particles have to be collided, i.e. determines the number of scattering events in each time step. In the fluid code, the collision frequency represents a coefficient in PDEs and does not effect on the duration of one iteration. Further, the pressure influences the number of the time steps required to reach a steady state and calculations at higher pressures are computationally more intensive. The magnetic field seems to have no effect on the number of time steps needed to converge to a steady state in the particle simulation, while the time of the fluid computation becomes longer when a magnetic field is involved, since the time steps governed by the CFL conditions are smaller. A basic comparison of the code performance was done for a PIC and a fluid simulation without the magnetic field. One time step of the particle code (written in C++) for 6×10^6 charged particles on a grid with the resolution 200×200 and the parameters specified in Tab. 4.1 takes 3.6 s using the Intel compiler and running on an Intel Core 2 Quad 2.83 GHz CPU. It requires about 1×10^5 iterations to converge to a steady-state solution. One iteration of the fluid code (written in Fortran) running with the same parameters and the grid resolution 200×200 takes 0.07 s on the same machine. The sufficient number of time steps to reach a steady-state solution is 5×10^4. The most time-demanding part of the computation is the Poisson solver. The UMFPACK library was used in both cases to solve for the potential distribution. Even if the PIC code can be eventually further parallelized, it is much more intensive computation than the fluid code. In addition, for higher pressures, the time steps $\Delta t_{\mathrm{e}} = 1 \times 10^{-11}$ s and $\Delta t_{\mathrm{i}} = 1 \times 10^{-8}$ s, that were chosen in order to obtain results reasonably fast, might be too large and smaller time steps would be appropriate. In that case, the difference in the efficiency of the particle and fluid code would become substantial. At last, it should be mentioned that the results of the particle code, namely the plasma density and the electric potential, were obtained as an average over 5×10^4 iterations to reduce the noise and produce results comparable with the fluid approach.

In general, the fluid approach assuming the equilibrium distribution function is an approximate calculation giving correct results of a qualitative character. It is advisable to use the fluid approach for problems when obtaining effective and fast results is a priority rather than the accuracy of the calculation. Due to the principle of the fluid description, the fluid model has a limited predicative capability. It is not possible to obtain information about individual particles, e.g. the angular or energy distribution of the particles impinging on the probe surface. Such information might be useful or important in some plasma-based technologies. In that case, the particle or the hybrid technique must be used. The essential disadvantage of the particle codes are time demands. On the other hand, the solution is more accurate, there is no assumption limiting the distribution function and the model can be more easily modified to solve complicated experimental conditions, in particular, conditions at the boundary (the drift motion of charged particles in electric and magnetic fields), more complicated collision processes, physical and chemical processes on the electrode surfaces (the secondary emission, the charging of solid layers, etc) or dynamic processes in the sheath region. The fluid approach is an optimal way to solve problems if physics, the geometry and investigated conditions are less complex and if the efficiency is an important point. The particle method is preferable if a solution of the high accuracy is required and if the solved problem is too complex to be described by the fluid approach. The hybrid technique, in which some aspects are treated microscopically and some aspects macroscopically, could be applied as a compromise between the accuracy and the performance.

CHAPTER 7

Conclusions

The size and the shape of the sheath region surrounding a solid substrate embedded into a plasma depend on plasma properties and processes taking place in the sheath during the plasma-solid interaction. In particular, the magnetic field strength or collision processes strongly influence the sheath structure. Even in case of relatively weak magnetic field, the effect can be clearly seen. Various effects were analyzed by means of two computational techniques – the particle and fluid modelling and these two approaches were compared and discussed.

The presented models were simplified by neglecting non-elastic collisions and assuming a constant temperature and a constant mean frequency of plasma-neutral collisions. These aspects could influence the results quantitatively, but the qualitative effect and the tendency of the results under the influence of various conditions would remain the same. At least, it would be appropriate to use an energy-dependent cross-section of the elastic collisions (as it is shown in [57]), however, here a simplified model has been set in order to compare two different techniques on a basic level, while the issue of collisions is analyzed e.g. in [46] and [57]. In principle, the models could be extended to include non-elastic collisions and energy-dependent cross-sections. In case of the fluid approach, it would be rather straightforward to upgrade the model described here and improve the treatment of collision processes or eventually include also the energy balance, because the numerical implementation would remain the same.

After a modification (with different input parameters, e.g. a different temperature, different type of particles with appropriate collision processes, etc), the analysis could be used for similar problems in different types of plasma. Limiting assumptions used here are the undisturbed plasma with the Maxwell velocity distribution at the outer boundary and neglecting an external electric field. The latter assumption is justified for the investigated problem in the DC glow discharge.

The electrostatic interaction between particles is calculated by the PIC method. This method is obviously more efficient (the time complexity $O(N \log N)$) than the basic direct summation of the forces from all constituent particles ($O(N^2)$) and the algorithm is easier to implement than advanced techniques such as the Ewald summation or FMM ($O(N)$). A drawback of the PIC technique, which uses the interpolation on a grid, is that interactions of particles within a cell of the grid are neglected. Short-distance interactions are resolved for instance in hierarchical algorithms (e.g. Barnes-Hut algorithm), see [47] for more details.

The efficiency of both implemented techniques in two dimensions was compared. The PIC code could be eventually further optimized and the code performance could be increased. The considered studied problem was described by two-dimensional models. It would require, however, a three-dimensional modelling to describe more complicated geometry of immersed substrates or to involve an arbitrary magnetic field. Both codes could be extended into three dimensions in a straightforward manner, but in case of the particle code, a three-dimensional calculation would be computationally too intensive and would demand the parallelization or stronger algorithms for calculating the force field. Some aspects of the models could be also combined together into a hybrid approach or the particle simulation could use a prescribed electric potential calculated by the fluid model. In three dimensions, anyway, also memory requirements might be critical and a three-dimensional simulation, particularly its spatial resolution, might be limited by memory capabilities.

PART II

TOKAMAK PLASMA MODELLING

CHAPTER 8

Theoretical background

8.1 Tokamak configuration

The essence of plasma confinement in a tokamak device consists in introducing a magnetic field which limits the transport of charged particles in the direction perpendicular to the magnetic field and hence enormously slow down plasma losses on the walls of the machine.

A scrape-off layer (SOL) is formed at the boundary by embedding a solid surface (a limiter or divertor) into the device (Fig. 8.1). The solid material in a contact with plasma constitutes a sink since charged particles tend to stick to solid surfaces. The charged particles are transported to the solid surface in the quickest loss direction resulting in a rapid parallel transport along the magnetic field lines to the limiter or divertor plates. The plasma is scraped-off in a thin SOL which limits the radial extent of the plasma. One benefit of the thin SOL is that the contact of the plasma with the outer walls can be avoided, although the price paid is that the plasma surface interaction is highly localized at the targets which can therefore suffer from a severe erosion, melting or evaporation [61, 62].

Particles in the SOL follow a helical trajectory along the magnetic field lines to the targets. The typical parallel distance (the connection length) for a toroidal limiter or a poloidal divertor (Fig. 8.1) can be approximated as

$$L_\mathrm{c} \approx \pi R_\mathrm{t} q_\mathrm{s} \tag{8.1}$$

and it is defined to be such that the distance between two points of the contact with the solid surface is $2L_\mathrm{c}$. The geometric role of the safety factor

$$q_\mathrm{s} \approx \frac{R_\mathrm{p} B_\mathrm{t}}{R_\mathrm{t} B_\mathrm{p}} \tag{8.2}$$

is its relation to the helicity of magnetic field lines, but the principal significance lies in a stability condition imposed on the safety factor and hence on

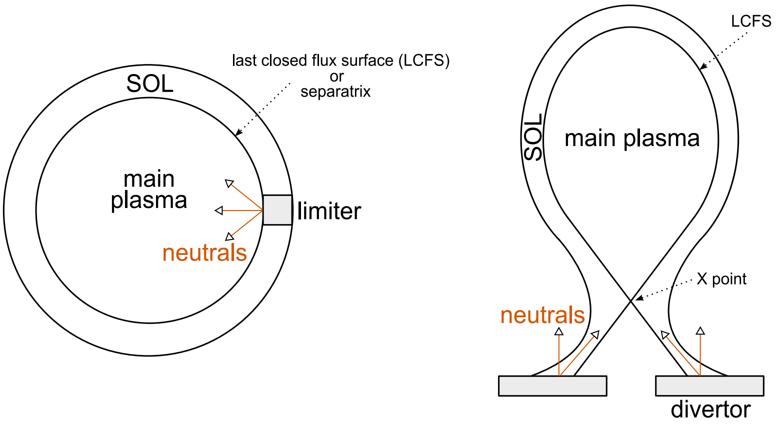

Figure 8.1: A scheme of the limiter and divertor configuration in the poloidal cross-section. A thin scrape-off layer is formed in the region of open field lines where the plasma is in a direct contact with a solid surface.

the configuration of the tokamak [2, 63]. The equation (8.2) is an approximation for a large aspect ratio $R_\mathrm{t}/R_\mathrm{p}$ and circular cross-section tokamak. R_t and R_p is the toroidal and poloidal radius, B_t and B_p is the toroidal and poloidal magnetic field (Fig. 8.2).

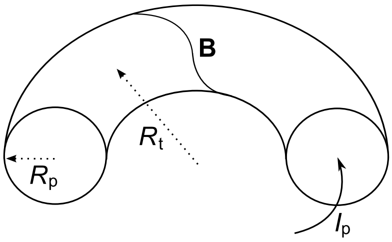

Figure 8.2: The geometric configuration of a tokamak – the poloidal radius R_p, the toroidal radius R_t, the magnetic field $\mathbf{B}$ and the total plasma current I_p.

8.2 Plasma-solid interaction

8.2.1 Sheath properties

Basic properties of a plasma and their establishment are dependent on the way the plasma interacts with a solid surface. The Debye sheath develops spontaneously at the interface, forming a region of a net charge with a substantial potential drop. In a simple picture of the sheath formation, the electrons, due to their lighter mass, spontaneously charge the solid surface negatively creating an electric field that retards the electron outflow and accelerates the ions and equilibrates to the ambipolar transport along the SOL where the plasma remains quasineutral. In the edge physics, the plasma parameters such as the plasma density and temperature are strongly influenced by the presence of the sheath. The sheath properties are the boundary conditions for the edge plasma.

The theory of the electrostatic sheath employs the Bohm criterion for the plasma velocity at the sheath-presheath interface

$$u_{\mathrm{i}} \geq c_{\mathrm{s}}. \tag{8.3}$$

The relation (8.3) gives the ion velocity at the sheath entrance corresponding to the sound speed

$$c_{\mathrm{s}} = \sqrt{\frac{k(T_{\mathrm{e}} + T_{\mathrm{i}})}{m_{\mathrm{i}}}} \tag{8.4}$$

characterized by the electron and ion temperatures T_{e} and T_{i} and the ion mass m_{i}. The Bohm criterion normally holds with the equality, but there are some situations where the ions enter the sheath with the supersonic speed.

The Bohm criterion specifies the particle outflux from the plasma to the surface

$$\Gamma_{\mathrm{i}} = n_{\mathrm{i}}\sqrt{\frac{k(T_{\mathrm{e}} + T_{\mathrm{i}})}{m_{\mathrm{i}}}}, \tag{8.5}$$

relates the flux to the plasma parameters (the density n_{i} and the temperatures T_{e} and T_{i}) and quantifies the particle sink caused to the plasma by its contact with the solid surface. Note that the outflux is independent of a potential drop in the sheath. Similarly, the energy balance of the sheath can be found, relating the electron and ion heat flux Q_{e} and Q_{i} at the sheath entrance to plasma conditions. The sheath heat transmission coefficients δ_{e} and δ_{i} are defined as

$$Q_{\mathrm{e}} = \delta_{\mathrm{e}} k T_{\mathrm{e}} \Gamma_{\mathrm{e}}, \tag{8.6}$$

$$Q_{\mathrm{i}} = \delta_{\mathrm{i}} k T_{\mathrm{i}} \Gamma_{\mathrm{i}} \tag{8.7}$$

and quantify the energy sink at the solid surface. The heat transmission factors can be deduced from a simple theoretical approach, a detailed treatment is described in [62].

The sheath theory for a solid surface at an oblique angle to the magnetic field involves the Chodura sheath [62]. The usual electrostatic Debye sheath where $n_{\mathrm{e}} < n_{\mathrm{i}}$ is followed by a quasineutral magnetic presheath (the Chodura sheath). The key result of Chodura's analysis is the relation for the velocity of the ions along the magnetic field at the magnetic presheath entrance

$$u_{\mathrm{i}\|} \geq c_{\mathrm{s}} \tag{8.8}$$

known as the Chodura criterion (or the Chodura-Riemann condition).

8.2.2 Plasma-surface processes

When plasma species reach a solid surface, they undergo series of collisions with atoms of the solid. The particles can be scattered back to the plasma or trapped in the solid or the atoms from the surface of the solid can be released as a result of the impact by particles [63].

The ions which are incident at the solid surface may be neutralized and backscattered to return to the plasma. The neutral atoms arriving from the solid surface are excited and ionized by collisions with the electrons and act in a process called the recycling. The efficiency of the recycling process is described by the ratio of the flux returning to the plasma to the incident flux, referred to as the recycling coefficient R.

The sputtering is a process giving rise to impurities that are released from the solid surface as a result of impinging ions or atoms. The sputtering can occur due to physical or chemical reactions and it leads to an erosion of the solid surfaces. The impurities can be neutral atoms or they are ionized. They enrich significantly the edge physics through atomic processes and a radiation and they can have both harmful and beneficial consequences [62]. In the core, they induce a fuel dilution and cooling of the main plasma. This points at an important advantage of the divertor configuration – the targets where the intense plasma surface interactions occur are away from the confined plasma. It was the original motivation for introducing divertors, however, other advantages are described below. The properties of the solid surface and how the impurities act in interactions with the plasma depend on the atomic number Z and therefore the choice of a material is of a scientific importance. A desirable effect of the presence of impurities in the SOL is a volumetric power loss, greatly preferable to the intensive and localized power deposition by a particle impact on the small area of the solid. Besides intrinsic impurities produced by the sputtering at the limiter or divertor target (as carbon), we have impurities that are injected to the machine (e.g. neon). The strength of the sputtering is characterized by the sputtering yield Y defined as the ratio of the number of eroded particles and the number of incoming projectiles.

8.3 Plasma transport

The nature of the plasma transport in tokamaks is very complex. Particles and energy flow from the core to the SOL by cross-field transport (Fig. 8.3) and theoretical and computational studies of the main plasma transport have been established with some success. An important issue is the plasma behaviour in the SOL playing an important role in questions of the confinement and stability. Charged particles in the SOL follow the magnetic field lines to the targets acting as a sink for the plasma, which results in a parallel pressure gradient along the SOL forcing the motion of the charged particles towards the solid surface. It implicates a rapid parallel motion (Fig. 8.3), typically of the order of the sound speed $u_\parallel \approx 10^5$ ms^{-1}. The cross-field transport ($u_\perp \ll u_\parallel$) is found to be anomalous and it is generally accepted to be due to a plasma turbulence.

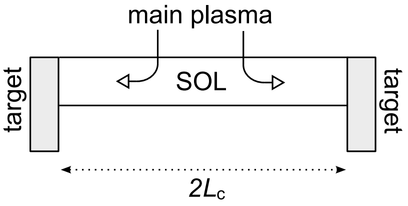

Figure 8.3: The SOL is straightened out in the direction of the magnetic field. The arrows indicate an energy and particles flow from the main plasma to the SOL.

Edge plasma models commonly follow an assumption of the classical plasma transport in the parallel direction and the fluid approach is widely used as the theoretical and computational description with certain constraints stated in sections 8.5 and 12.3. The radial transport is much larger than calculated from the classical theory and turbulence codes aim to describe its character on the basis of a turbulent motion, however, fluid edge models usually involve the convection-diffusion approximation

$$\Gamma_\perp = n v_{\mathrm{adv}} - D_\perp \frac{\partial n}{\partial r} \tag{8.9}$$

for the particle flux $\Gamma_\perp$ with an advective velocity v_{adv} and a coefficient of the diffusion $D_\perp$. The cross-field transport coefficients are obtained empirically.

The plasma impinging on the targets recombines on the surface and particles are subsequently released as neutrals. The neutral atoms are emitted into the plasma where they can be reionized, usually by an electron impact. Neutrals recycling from limiters tend to be ionized in the main plasma (Fig.

8.1), while in a divertor configuration, the ionization can primarily occur close to the targets below the X point. The transport of the neutrals is closely related to operational conditions of a machine.

8.4 Operational regimes

Operational conditions and the configuration of a tokamak device play an important role in physics of the edge. They affect the transport of neutrals along the SOL, the character of the plasma transport in the edge and plasma parameters (the density and temperature). Specific properties of the SOL (the distribution of particles, temperature gradients, the ionization of neutrals) indicate characteristic operational regimes. A basic insight can be gained from an analysis of the parallel transport. More information is provided in [61, 62, 64].

8.4.1 Simple SOL

If the parallel heat conductivity is small and the heat convection plays a large role in carrying the power along the SOL to the targets, the plasma tends to be isothermal with a constant temperature along the SOL. The SOL is in the sheath-limited regime. This regime is conceptually simple, however, not the most desirable one since it results in higher plasma temperatures at the target that can cause a strong sputtering, an erosion and a plasma contamination. The simple SOL is most typically encountered for geometric configurations involving limiters.

8.4.2 Complex SOL

Conditions when the parallel heat conduction becomes important and most of the exhaust power is carried by the conductive transport create the complex SOL with parallel temperature gradients that tend to arise when the conduction is high. The parallel temperature drop between the upstream location and the targets can be significant. Such conditions are more easily achieved using divertors.

8.4.3 Ionization of neutrals

The driving mechanism responsible for the establishment of particular conditions in the edge effecting on the character of the parallel transport, profiles of the plasma parameters and their gradients arises from a neutral production, transport and propagation across the SOL. The mechanism is principally governed by the configuration of a device and operational conditions (the average main plasma density and temperature and the total particle and power flow from the main plasma to the SOL).

In a simple SOL case, the ionization mean free path λ_{ion} is sufficiently high for neutrals to penetrate to the confined region and the ionization takes place primarily in the main plasma (Fig. 8.4). The neutrals recycling from limiters appear instantly in the confined region due to the direct contact of the limiter and the main plasma. The produced ions are dispersed rapidly along the field lines resulting in significant flows and a parallel heat convection along the SOL and introducing a source of particles which are distributed more or less uniformly in the parallel direction all along the length of the SOL. The main source of the electrons and ions in the SOL is a cross-field transport from the core and the sheath is the only important element in the edge influencing the transport of particles and energy from the confined region to the targets. The edge is in the sheath-limited (or the low-recycling) regime.

In the complex SOL, the ionization occurs in the SOL near the targets (Fig. 8.4) and it is an important source for particles. The ionization mean free path is small compared to the characteristic spatial scale of the system ($\lambda_{\text{ion}} \ll L$), a parallel heat conduction carry most of the exhaust power and the SOL is in the conduction-limited (or the high-recycling) regime.

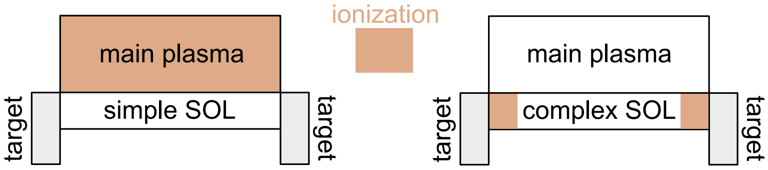

Figure 8.4: The SOL is straightened out in the parallel direction. The coloured areas indicate regions of the ionization for the simple SOL (left) and the complex SOL (right).

8.4.4 Detachment

The complex SOL is harder to understand and analyze, nevertheless it brings essential advantages. Let us summarize them briefly. A divertor configuration tends to the conduction-limited regime more naturally and its geometric advantage was described above. The ionization occurs mainly in the SOL, the role of the heat convection is reduced giving the temperature drop associated with the conduction. The temperature gradients in the SOL allow cool plasma in a contact with the solid surface, thus reducing its erosion.

Another important practical reason to operate a tokamak employing the complex SOL is a volume power loss taking place in the SOL in the high-recycling regime, while the high-recycling process is another consequence of a low target temperature (note that as the target temperature drops, the particle flux to the target increases). The volume power losses can occur due to a radiation of hydrogen or impurities or the charge-exchange and they are desirable because the power is deposited in a diffuse way instead of a deposition on the target to a small plasma-wetted area by a particle impact. Further, the recycling neutrals can cause a neutral frictional drag obstructing the plasma outflow and reducing the particle power deposition on the targets. A further benefit arises if the target temperature drops below a few eV. A volume recombination becomes strong, replaces the sink action of the solid target and contributes to the radiated power. Such regime can be achieved by decreasing the target density and temperature to low levels by an impurity injection and a radiative cooling or by raising the average density of the main plasma (see chapter 10).

For a detached regime, it is characteristic that the volume power loss processes remove most of the power that enters the SOL. For the lowest temperatures, the neutral frictional drag on the plasma flow and the volume recombination become important resulting in an essential feature of the detached divertor state with significantly reduced both the power and particle flux to the targets detaching the plasma from the targets. Experimentally, the divertor detachment is usually approached by ramping up the density at otherwise fixed discharge parameters. It is manifested as a drop of the particle flux (or the ion saturation current) onto the plate, an increase of the D_α signal, an increase of the neutral pressure in the divertor and a drop of the plasma density and plasma pressure at the plate. The divertor temperatures are found to be in a few eV range and the upstream separatrix densities typically show a moderate increase [62, 65, 66].

8.5 Edge plasma modelling

An initial modelling approach does not employ a combined system of the main plasma and the SOL in the self-consistent way, but takes as given the total particle and power flow from the main plasma into the SOL. The sources of energy and particles relate the SOL plasma parameters with the main plasma, specifically, with the average plasma density and temperature in the core. A self-consistent core-edge treatment is also possible, a simple model is introduced in chapter 10 with basic physics involved and using a zero-dimensional model of the core region and a one-dimensional model of the SOL. In this chapter, only models of the SOL follow.

The fluid modelling is the most common one in the SOL analysis. The justification of the fluid approach is a high level of collisionality. The SOL is collisional if the mean free path of electron-electron and ion-ion collisions is small compared to the macroscopic length scale $\lambda \ll L$ [62]. If the degree of collisionality is low, a kinetic treatment is required or a special approach based on kinetic corrections has to be introduced (see more in section 11.2.3).

8.5.1 Two-point model

A basic insight into the edge properties can be obtained from analytic models. The simplest model of a divertor SOL refers to two points along the SOL – the upstream location u (the half-way between the targets) and the target location t, and relates the plasma parameters at these positions. The two-point model neglects viscous effects, ignores a parallel source of the momentum (mainly the ion-neutral friction) and assumes equipartition $T_\mathrm{e} = T_\mathrm{i} = T$ together with the ambipolarity and the quasi-neutrality $n_\mathrm{e} = n_\mathrm{i} = n$. The momentum balance equation then restricts to the condition of a constant total pressure along the SOL

$$p + n m_\mathrm{i} u^2 = \mathrm{constant} \tag{8.10}$$

where $p = 2nkT$ is the plasma pressure. With boundary conditions for the plasma velocity $u_u = 0$ and $u_t = \sqrt{2kT_t/m_\mathrm{i}}$ (see section 8.2), we get the relation

$$2n_t T_t = n_u T_u. \tag{8.11}$$

The parallel heat conductivity can be calculated using the classical Spitzer expression [61, 67]

$$q_\parallel = -\kappa \frac{\partial}{\partial x}(kT) = -\kappa_0 T^{\frac{5}{2}} \frac{\partial T}{\partial x} \tag{8.12}$$

with the heat conduction coefficient κ. If all the exhaust power enters the SOL at the upstream point $x = L_\mathrm{c}$ and it is carried entirely by the conduction $q_\parallel$ to the target $x = 0$, we can integrate the equation (8.12) from 0 to L_c to get the relation

$$T_u^{\frac{7}{2}} = T_t^{\frac{7}{2}} + \frac{7 q_\parallel L_\mathrm{c}}{2\kappa_0}. \tag{8.13}$$

Using the boundary conditions for the heat flux at the target from section 8.2, we obtain the expression for the parallel heat flux

$$q_\parallel = \delta k T_t n_t c_\mathrm{st} \tag{8.14}$$

with the sheath heat transmission coefficient δ and the target sound speed c_{st}. The equations (8.11), (8.13) and (8.14) constitute the two-point model. Three unknowns T_t, T_u and n_t are specified by the control parameters n_u and $q_{\|}$ related to the principal parameters – the input power and the main plasma density. In general, we can relate the density and temperature at the target to any point in the parallel direction x sufficiently far from the target, while the target values are the boundary conditions. The form of the model is useful since we can take the target values from measurements and calculate the upstream values using accessible experimental data. A simplest approximation ignores radial variations of the plasma parameters across the SOL. A more refined approach, the onion-skin method, uses a concept of individual flux tubes and apply the equations (8.11), (8.13) and (8.14) to each flux tube across the SOL.

8.5.2 One-dimensional fluid model

In the one-dimensional fluid description, the SOL is straightened out along the magnetic field and the model describes parallel profiles of the plasma parameters between the solid surfaces. The transport in the parallel direction is solved, while the cross-field transport is included in source terms of fluid equations. The standard fluid formulation follows Braginskii [68] and in a stationary state, the continuity, momentum and energy equations for the plasma density n, the parallel velocity u and the electron and ion temperatures T_{e} and T_{i} take form

$$\frac{\mathrm{d}}{\mathrm{d}x}(nu) = S^n, \tag{8.15}$$

$$\frac{\mathrm{d}}{\mathrm{d}x}\left(m_{\mathrm{i}}nu^2 + p_{\mathrm{i}} + \pi_{\mathrm{i}}\right) = enE + R + m_{\mathrm{i}}S^u, \tag{8.16}$$

$$\frac{\mathrm{d}}{\mathrm{d}x}\left[\left(\frac{5}{2}nkT_{\mathrm{i}} + \frac{1}{2}m_{\mathrm{i}}nu^2\right)u + \pi_{\mathrm{i}}u + q_{\mathrm{i}}\right] = (enE - R)u - Q + S_{\mathrm{i}}^E, \tag{8.17}$$

$$\frac{\mathrm{d}}{\mathrm{d}x}\left(\frac{5}{2}nkT_{\mathrm{e}}u + q_{\mathrm{e}}\right) = (R - enE)u + Q + S_{\mathrm{e}}^E \tag{8.18}$$

assuming the ambipolarity $u_{\mathrm{e}} = u_{\mathrm{i}} = u$ and no net current $n_{\mathrm{e}} = n_{\mathrm{i}} = n$. R are the thermal losses and the friction force due to collisions between the electrons and ions, Q is the energy exchange term between the electrons and ions, p_{i} is the ion static pressure, π_{i} is the parallel viscous stress, q_{e} and q_{i} are the parallel thermal heat fluxes, E is the electric field and S^n, S^u and S^E are net sources of the mass, momentum and energy.

8.5.3 Two-dimensional fluid model

The two-dimensional edge modelling commonly assumes a toroidal symmetry and the two spatial directions are the radial and poloidal projection of the motion along the magnetic field. Multifluid two-dimensional models involve complex physics of the plasma transport, the impurity transport and the transport of neutrals including the Monte Carlo treatment of the neutrals, kinetic effects, involving the sheath theory and describing atomic and molecular processes, boundary processes, etc. An introduction to the two-dimensional edge codes is given in chapter 12.

CHAPTER 9

Introduction

9.0.4 Present status

Numerical simulations and modelling of the tokamak plasma are an important part of the fusion research. A variety of numerical codes exists based on different numerical techniques and different approaches of the theoretical description. The complexity of tokamak physics involving processes on profoundly different temporal scales ($\sim$ 100 GHz – 1000 s) and with broad spatial range ($\sim$ 10 μm – 10 m) makes impossible to develop an integrated model of the tokamak plasma and one simulation never covers the whole temporal and spatial range (Fig. 9.1).

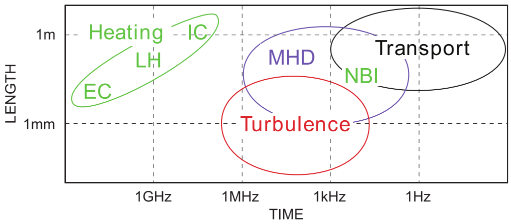

Figure 9.1: Temporal and spatial scales in the tokamak physics. Reprinted from [69].

A number of codes have been developed to describe separately different regions in a tokamak device (the core, the edge, the divertor, the walls) and a number of codes have been constructed to solve particular aspects of the tokamak physics (the edge physics, the transport in the core, the turbulent transport, the equilibrium, the heating, etc). A summary of areas where the modelling is applied is listed in Fig. 9.2. Let us mention some of the codes and the simulation areas: the core transport – ASTRA, CRONOS, JETTO, RITM, TRANSP [70–73], the edge multifluid codes – SOLPS-B2/EIRENE, EDGE2D/NIMBUS, UEDGE, TECXY [66, 74–76], the edge kinetic codes –

BIT1 [77, 78], the impurity tranport – ERO, SANCO [79, 80], the equilibrium reconstruction – EFIT, EQUINOX, CEDRES, CLISTE [81], the high-resolution equilibrium – CAXE, CHEASE, HELENA [81], the linear MHD stability – KINX, MISHKA, CASTOR, ILSA, ELITE, IDBALL [81], the turbulence and microinstability – GENE, GEM, GKW, ORB5, ELMFIRE, GYSELA, CUTIE, ESEL, KINEZERO, GS2 [82], the heating, current drive and past particle physics – NBI deposition codes, antenna codes, wave codes, Fokker-Planck codes, fast particle instability codes [83–86], the non-linear MHD and disruptions – M3D, NIMROD [87–89]. The numerical treatment is always a question of the specific application and employs e.g. the fluid method, the kinetic approach or the gyrokinetic technique.

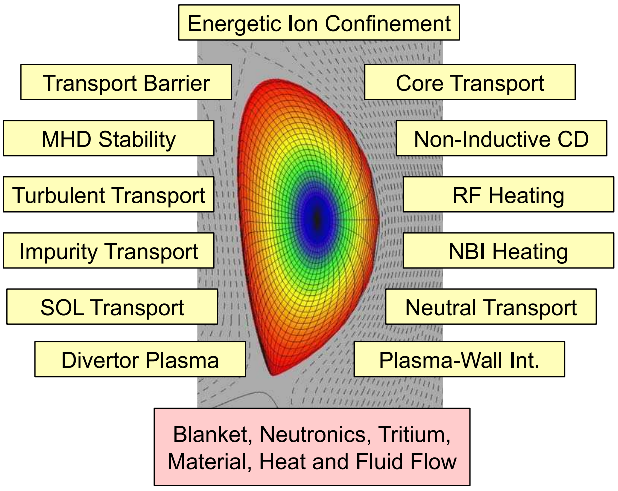

Figure 9.2: Simulation areas in the tokamak plasma research. Reprinted from [69].

Several numerical codes exist for each part of the tokamak physics, however, in experiments, these different parts clearly influence each other suggesting that there is a need to include and couple all the possible phenomena also in numerical simulations. This is a concern of European activity. The aim of the integrated tokamak modelling (ITM) project [90] is to combine and integrate existing numerical tools to interact each other and to provide a suite of codes necessary for analyzing the tokamak physics with a special interest in the future ITER scenario [91]. An example of the integrated approach can be the COCONUT code [92] combining the Monte Carlo code for neutrals (NIMBUS, EIRENE), the two-dimensional SOL code EDGE2D, the core transport code JETTO and using SANCO for impurities. Another example is the American FACETS project [93] for coupled core-edge transport simulations using UEDGE.

9.0.5 Outline of presented work

In chapter 10, a numerical investigation of plasma parameters in a divertor configuration of the COMPASS tokamak is presented. The plasma parameters in the device are analyzed in the frame of a self-consistent description of the central plasma and the edge region and a possibility of achieving high recycling and detached regimes in the boundary layer of the COMPASS tokamak is discussed.

Chapters 11 and 12 are devoted to the edge plasma modelling. A one-dimensional fluid code has been developed to solve the plasma and neutral transport in the SOL (chapter 11). Concerning the complexity, it represents a halfway between the simple analytic model described in section 8.5.1 and the complex two-dimensional edge codes that are available in the fusion community (chapter 12).

The model introduced in sections 11.1–11.3 provides a basic insight into the edge physics and into more sophisticated two-dimensional tools. The attention is given to the transport of plasma species and neutrals along the magnetic field, results for different operational regimes are presented and the influence of operational conditions on the transport properties is explained (section 11.4). The code has been validated (section 11.5) and a benchmark with the B2 code is in progress. The code was further modified to solve also time-dependent problems and it is being prepared for coupling with the ESEL code [94] to provide a better description of the parallel transport in ESEL and improve match of ESEL simulation results with measured data.

An introduction to the two-dimensional edge codes follows in chapter 12 which has a character of a synopsis only. It gives a summary of the available codes, it briefly describes the background of physics and the computational techniques and it provides a number of references. A future aim is to apply such code to the COMPASS tokamak.

The work presented in Part II was a subject of an international collaboration within the fusion community in Europe. Details are specified at the end of Part II (chapter 13).

CHAPTER 10

Numerical investigation of plasma parameters in COMPASS tokamak

10.1 COMPASS device

The COMPASS tokamak has been transferred from UKAEA to IPP Prague in 2007 [95]. The new device has replaced the CASTOR tokamak and its reinstallation has been planned in several steps. First, new power supplies consisting of two flywheel generators were developed and basic facilities for diagnostics were installed. The first discharge was achieved on 9th December 2008 and on 19th February 2009, the COMPASS officially started to operate. The tokamak has been put in a routine operation in the Ohmic regime with the toroidal magnetic field around 1 T. In the next step, an installation of the NBI system (2 x 300 kW) will be done together with a redeployment of the existing LH system (400 kW) and the toroidal magnetic field will be increased up to 2.1 T. The COMPASS tokamak has an ITER-like plasma shape and with the NBI heating system, it will be able to access plasma parameters relevant in many aspects to ITER. Further, it allows to investigate regimes with large normalized Larmor radius ρ^* (the Larmor radius normalized by the minor radius $\rho^* = \rho/R_\mathrm{p}$) and collisionality ν^* (the ratio of the characteristic length scale and the mean free path of collisions $\nu^* = L/\lambda$).

In order to analyze plasma parameters in the COMPASS device under different operating scenarios, a modelling activity has been undertaken. The plasma performance in the COMPASS tokamak has been analyzed in the frame of the self-consistent treatment of the core and edge plasma. The numerical tool was provided by R. Zagórski (Institute of Plasma Physics and Laser Microfusion, EURATOM Association, Warsaw, Poland) and the model was previously applied to the FTU tokamak [96].

The issue of global simulations is to assess a range of plasma parameters we can expect in the device as well as to determine plasma conditions when high recycling or detached regimes (section 8.4) would develop in the divertor of the COMPASS tokamak.

10.2 Numerical model

The global self-consistent description of the core and edge plasma behaviour is based on a zero-dimensional model of the plasma transport in the centre and a one-dimensional model of plasma dynamics in the scrape-off layer. A detailed description of the model and physics it involves is given in [97].

10.2.1 Core region

Plasma parameters in the core (the plasma temperature $T_\mathrm{e} = T_\mathrm{i} = T$, the ion density n_i and the plasma current j_θ) are assumed to have radial profiles in the form of generalized parabolas

$$T(r) = T_0 \left[1 - \left(\frac{r}{R_\mathrm{p}}\right)^2\right]^{\alpha_T} + T_s, \tag{10.1}$$

$$n_\mathrm{i}(r) = n_{\mathrm{i}0} \left[1 - \left(\frac{r}{R_\mathrm{p}}\right)^2\right]^{\alpha_n} + n_{\mathrm{i}s}, \tag{10.2}$$

$$j_\theta(r) = j_{\theta 0} \left[1 - \left(\frac{r}{R_\mathrm{p}}\right)^2\right]^{\alpha_j} \tag{10.3}$$

with exponents $\alpha_T = 2.0$, $\alpha_n = 1.5$ and $\alpha_j = 1.5\alpha_T$ consistent with old COMPASS experimental profiles [95]. R_p is the plasma radius, T_0, $n_{\mathrm{i}0}$ and $j_{\theta 0}$ are values in the centre and T_s and $n_{\mathrm{i}s}$ are values at the separatrix. The profile of impurities is prescribed as

$$n_\mathrm{z} = \left(\frac{n_\mathrm{e}}{n_{\mathrm{e}s}}\right)^{\alpha_\mathrm{z}} n_{\mathrm{z}s} \tag{10.4}$$

with $\alpha_\mathrm{z} = 0.5$ corresponding to a flat profile of the effective charge Z_eff. The effective charge of the plasma is defined as

$$Z_\mathrm{eff} = \frac{\sum\limits_j n_j Z_j^2}{\sum\limits_j n_j Z_j} \tag{10.5}$$

where the summation is over ionic species (also impurities) and the densities satisfy the quasi-neutrality $n_\mathrm{e} = \sum_j n_j Z_j$. The plasma parameters at the separatrix (index s) which result from the SOL model described below are required as input data to this part of the model. The plasma temperature in the centre is calculated from the energy balance equation

$$\frac{3\langle n_\mathrm{e} T\rangle}{\tau_E} = P_\mathrm{aux} + P_\mathrm{OH} - f_\mathrm{rad} P_\mathrm{lin} = P_\mathrm{core} \tag{10.6}$$

where P_core is the total power in the core composed of the auxiliary heating power P_aux, the ohmic power P_OH and the line radiation power P_lin. These parameters are determined according to expressions given in [98] and the energy confinement time τ_E corresponds to ITER98(y2)-ELMy H mode scaling law [99]. The coefficient f_rad is the ratio between the power radiated in the core and the total radiated power. The power flowing to the SOL is defined as $P_\mathrm{inp} = P_\mathrm{aux} + P_\mathrm{OH} - P_\mathrm{lin}$.

10.2.2 Boundary region

The simulation of the plasma behaviour in the SOL is based on the standard two-point model (section 8.5.1). The energy balance in the SOL defines the equation for the temperature at the target plate (index p)

$$P_\mathrm{plate}(T_p) = P_\mathrm{inp}(T_p) - P_\mathrm{rad}^\mathrm{SOL}(T_p) \tag{10.7}$$

where $P_\mathrm{rad}^\mathrm{SOL}$ is the line radiation in the SOL and the power flowing to the SOL P_inp is calculated in the core part of the model. The plasma density at the plate and the plasma temperature and density at the separatrix are evaluated according to expressions corresponding to the two-point model relating values at the separatrix to values at the plate

$$n_{\mathrm{e}s} T_s \approx 2 n_{\mathrm{e}p} T_p, \tag{10.8}$$

$$n_{\mathrm{i}p} = \frac{\Gamma_\mathrm{inp}}{c_\mathrm{s} S_\mathrm{eff}(1-R)}, \tag{10.9}$$

$$T_s \approx T_p \left(1 - \frac{7 Q_\mathrm{inp} L_\mathrm{c}^2}{2\kappa_0 T_s^{7/2} V_\mathrm{SOL}}\right)^{-1} \tag{10.10}$$

using the particle flux to the SOL Γ_inp, the effective area of the divertor plates S_eff, the recycling coefficient R, the sound speed c_s, the energy flux to the SOL Q_inp, the connection length L_c, the heat conduction coefficient κ_0 and the SOL volume V_SOL. An impurity model includes both sputtered and additional impurities and it is described in [97] in more detail. Radiation losses in the core and the SOL regions are calculated assuming corona equilibrium [100].

Physics of the model has been implemented into a numerical code in which an iterative scheme is used in order to achieve a steady-state solution and the numerical method solves for the plasma characteristics in the SOL and in the core region with the last close flux surface (LCFS) being an interface. A similar model was successfully applied to a poloidal limiter configuration of the FTU tokamak and it was verified by a comparison with an experiment [96].

10.3 Results

The self-consistent core-edge model has been applied to assess the plasma performance in the reinstalled COMPASS tokamak. Basic parameters of the device used in the simulations are as follows: the toroidal radius $R_\mathrm{t} = 0.56$ m, the poloidal radius $R_\mathrm{p} = 0.21$ m, the elongation $\kappa = 1.8$, the auxiliary heating power $P_\mathrm{aux} = 0.7$ MW (which takes into account the NBI and LH heating). We assume that the anomalous radial diffusion is of the order of Bohm diffusion ($D_\perp = \frac{1}{3} D_\mathrm{Bohm}$) and we take $R = 0.975$ as the recycling coefficient in the SOL, the same value as reported in [97]. In the model, carbon is a sputtered impurity and we take into account both the physical and the chemical sputtering. In some simulations, neon is considered as an additional (injected) impurity.

We have investigated operational regimes with the toroidal magnetic field $B_\mathrm{t} = 1.2$ T (corresponding to a standard COMPASS configuration) as well as the higher magnetic field $B_\mathrm{t} = 2$ T which is predicted as a future upgrade of the COMPASS device [95]. For every magnetic field B_t, two plasma currents I_p are considered (Tab. 10.1).

	case 1	**case 2**	**case 3**	**case 4**
B_t[T]	1.2	1.2	2.0	2.0
I_p[kA]	100	200	200	350
$n_\mathrm{G}[10^{20}\mathrm{m}^{-3}]$	0.72	1.44	1.44	2.53

Table 10.1: Investigated operational regimes.

First, we analyze global plasma parameters in COMPASS by changing the average plasma density $\langle n_\mathrm{e} \rangle$ in the device in the range $0.1 n_\mathrm{G} \leq \langle n_\mathrm{e} \rangle \leq 0.85 n_\mathrm{G}$ where n_G is the Greenwald density (a measure of the density limit for tokamaks $n_\mathrm{G} = I_\mathrm{p}/\pi R_\mathrm{p}^2$ with the plasma current expressed in MA and

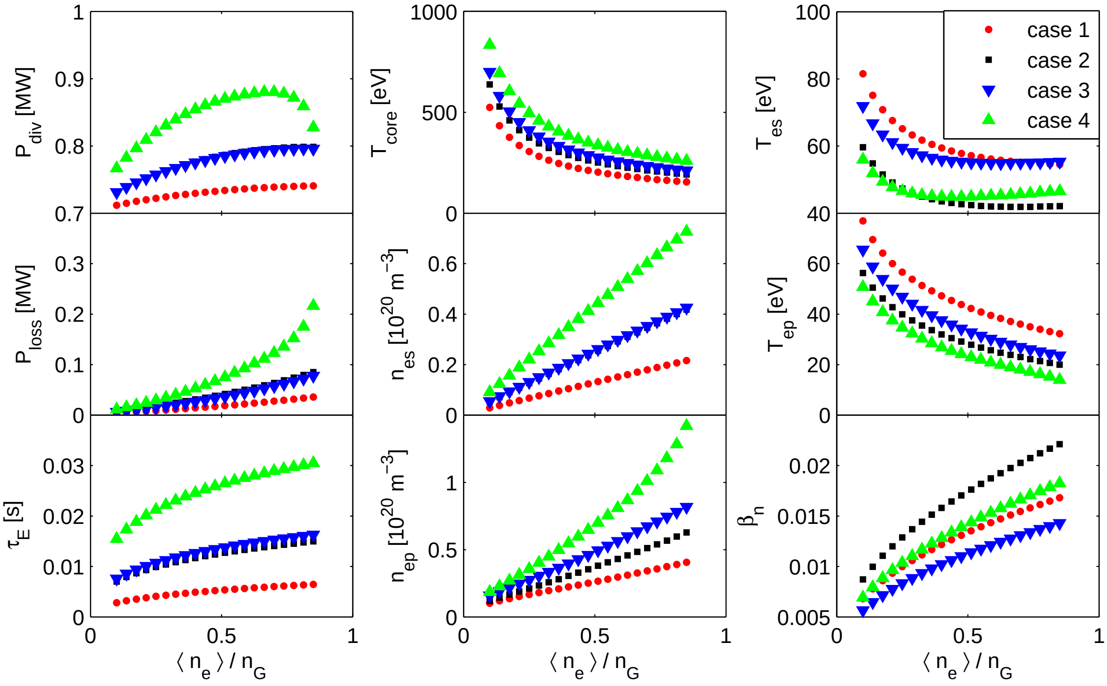

Figure 10.1: The power to the target plate P_{div}, the total energy losses P_{loss}, the energy confinement time τ_E, the average plasma temperature T_{core}, the plasma density at the LCFS n_{es}, the plasma density at the plate n_{ep}, the plasma temperature at the LCFS T_{es}, the plasma temperature at the plate T_{ep} and the normalized parameter β_{n} as functions of the normalized volume average density $\langle n_{\mathrm{e}} \rangle / n_{\mathrm{G}}$ for different configurations specified in Tab. 10.1. The scaling B).

the density in 10^{20} m^{-3}). Since the scaling for the edge plasma density n_{es} for the COMPASS tokamak is not available, three different expressions were considered: A) $n_{es} = \frac{1}{2}\langle n_{\mathrm{e}} \rangle$, B) $n_{es} = \frac{1}{3}\langle n_{\mathrm{e}} \rangle$, C) $n_{es} = \frac{1}{4}\langle n_{\mathrm{e}} \rangle$.

Results of the simulations for all four cases (Tab. 10.1) and for the medium scaling of the edge density B) are shown in Fig. 10.1. It can be seen that with increasing plasma density, the confinement time increases (according to the energy scaling law) and the plasma temperature in the core decreases, however, the normalized beta β_{n} ($\beta_{\mathrm{n}} = \beta R_{\mathrm{p}} B_{\mathrm{t}} / I_{\mathrm{p}}$ with the plasma current expressed in MA) increases and for the highest densities we approach the ballooning limit $\beta_{\mathrm{n}} \sim 0.25$ (the maximum beta attainable due to the ballooning instability that can develop when the plasma pressure exceeds a critical value). Since the Ohmic heating is small, changes to the heating power are weak and the same refers to the power transmitted to the divertor plates. It should be noted that plasma radiation losses are relatively small even for the highest plasma densities. In fact, the edge plasma pa-

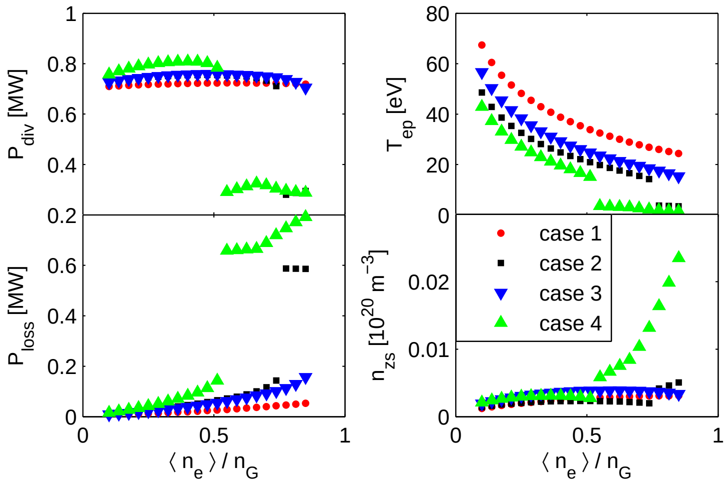

Figure 10.2: The power to the target plate P_{div}, the total energy losses P_{loss}, the plasma temperature at the plate T_{ep} and the sputtered impurity density at LCFS n_{zs} as functions of the normalized volume average density $\langle n_{\mathrm{e}}\rangle/n_{\mathrm{G}}$ for different configurations. The scaling A).

rameters correspond to the simple SOL picture (see section 8.4) with weak temperature and density gradients. For the highest edge densities, the plate temperature is well above the 5 eV level at which we can expect a development of detached regimes in the divertor. The plasma contamination is low and Z_{eff} is below 1.8 even for the lowest densities.

Very similar picture is obtained for the case C) with lower edge plasma densities. In the case of high edge densities (the scaling A)), a new regime could develop in the SOL if the plasma density was large enough (the cases 2 and 4, note that n_{G} is proportional to the plasma current), as it can be seen in Fig. 10.2. If the plasma density exceeds some threshold value, then

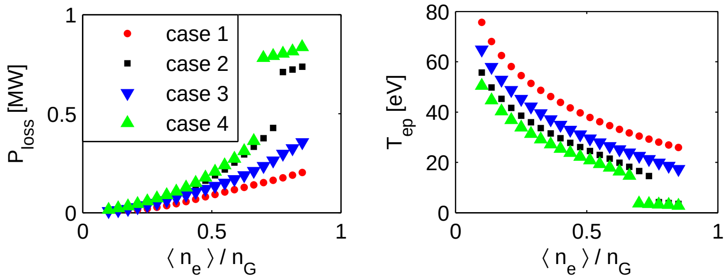

Figure 10.3: The total energy losses P_{loss} and the plasma temperature at the plate T_{ep} as functions of the normalized volume average density $\langle n_{\mathrm{e}}\rangle/n_{\mathrm{G}}$ for different configurations. The scaling B).

the temperature at the plate drops below 5 eV, a high density plasma is formed in the divertor and energy losses due to the impurity radiation are significant. We note that the core parameters are almost not affected by the transition to the detached mode. It should be remarked that such desirable strongly radiating regime develops only at high plasma densities. In a real device, it could be very difficult to operate with so large separatrix density n_{es}. However, it appears that the access threshold to the detached regime could be lowered by introducing additional impurities. This is illustrated in Fig. 10.3 where we show results corresponding again to the scaling B) (see Fig. 10.1), but with an addition of the injected impurities (neon).

It comes out from the simulations that the achievement of the detached regime depends strongly on three parameters – the average plasma density $\langle n_{\mathrm{e}} \rangle$, the separatrix plasma density n_{es} and the impurity concentration n_{z}. In order to analyze the transition to the detached regime in more detailed way, we have separated combined effects of these parameters. First, we made a scan changing the separatrix plasma density n_{es} at a constant average plasma density $\langle n_{\mathrm{e}} \rangle$. We consider cases without an injected impurity and with some concentration of neon. Results for $B_{\mathrm{t}} = 2$ T and $I_{\mathrm{p}} = 350$ kA (the case 4) are shown in Fig. 10.4. It can be seen that for the lower plasma density ($\langle n_{\mathrm{e}} \rangle = 0.2 n_{\mathrm{G}}$), it is impossible to achieve the detached regime independently of the edge plasma density as well as the impurity concentration, however, the transition appears for the higher density ($\langle n_{\mathrm{e}} \rangle = 0.7 n_{\mathrm{G}}$) for relatively large range of the edge plasma densities. In order to investigate the effect of additional impurities, we show the results of simulations for the same case (the case 4, $\langle n_{\mathrm{e}} \rangle = 0.7 n_{\mathrm{G}}$), but for different concentrations of neon (Fig. 10.5). Two branches of solution corresponding to an attached and a detached plasma are clearly seen in Fig. 10.5. It is interesting to point out that in the

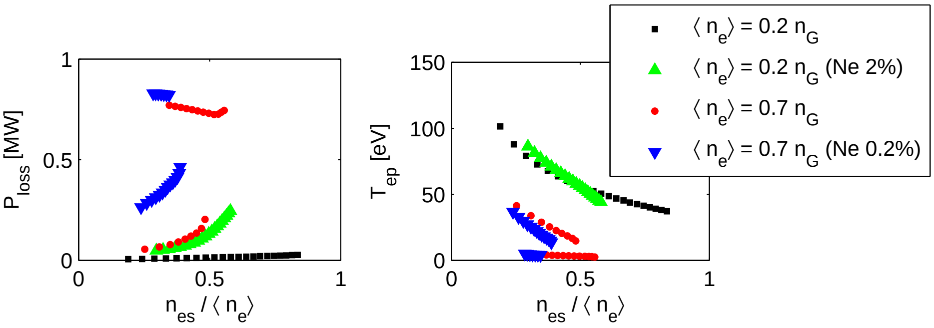

Figure 10.4: The total energy losses P_{loss} and the plasma temperature at the plate T_{ep} versus the normalized plasma density at the LCFS $n_{es}/\langle n_{\mathrm{e}} \rangle$ for two different volume average densities $\langle n_{\mathrm{e}} \rangle$ and neon concentrations.

detached regime, the plasma parameters are almost independent on the edge density and the impurity concentration. The threshold density is reduced when the concentration of neon increases. It should be mentioned that in the detached regime, there is a significant production of carbon due to the chemical sputtering, while for the attached regimes, the physical sputtering is responsible for the carbon release.

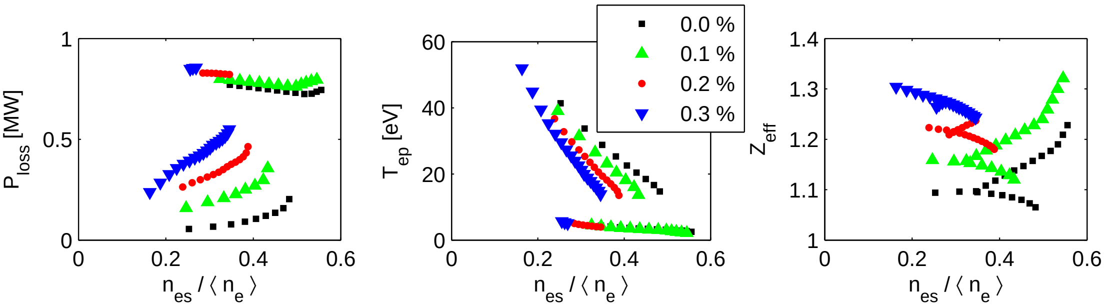

Figure 10.5: The total energy losses $P_{\rm loss}$, the plasma temperature at the plate T_{ep} and the average effective charge $Z_{\rm eff}$ versus the normalized plasma density at the LCFS $n_{\rm es}/\langle n_e \rangle$ for different concentrations of additional impurities.

10.4 Summary

Plasma parameters in the divertor of the COMPASS tokamak have been investigated by means of a global model which couples the central region of the main plasma and the scrape-off layer in a self-consistent way. Simulations have been done for different operating scenarios of the COMPASS device in order to estimate conditions for developing high recycling and detached regimes. It has been found that the operational space of the tokamak is relatively broad in terms of available plasma densities, plasma currents and magnetic fields. At a high plasma density, operations with high $\beta_{\rm n}$ values are possible, but with a relatively low core plasma temperature. It appears that detached conditions in the divertor can be created only if the plasma density is high enough and/or if an additional (injected) impurity is present.

CHAPTER 11

One-dimensional model of edge plasma transport

11.1 Basic features

To study fundamental transport processes in the scrape-off layer of a divertor tokamak, a one-dimensional fluid code has been developed. The computational region is schematically shown in Fig. 11.1. We consider a one-dimensional computational domain parallel with magnetic field lines with divertor plates at the boundaries and the magnetic field does not explicitly appear in the model.

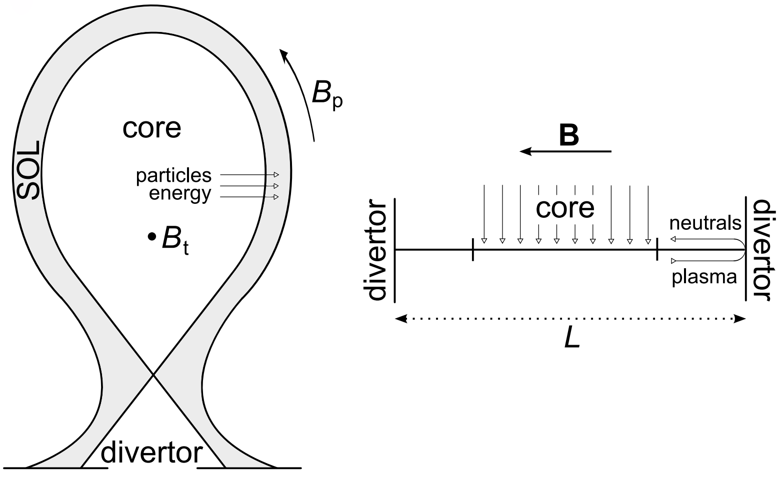

Figure 11.1: A scheme of the divertor configuration in the poloidal cross-section (left) and a one-dimensional computational domain (right). The SOL is straightened out in the parallel direction along the magnetic field with the divertor targets at the boundaries.

A transport of particles is simulated by the fluid approach taking into account three types of species – electrons, main ions and neutrals. In a real device, impurity atoms or impurity ions in various charge states are present, being either sputtered on the solid surface or injected into the machine. These species broaden the range of atomic and molecular processes and they may influence stability and transport properties. On one hand, they can dilute and contaminate the plasma and effect negatively on the plasma confinement, on the other hand, they can positively influence the transition to a high-recycling or a detached regime (chapters 8 and 10). The impurities are not present in the model, nevertheless, even with a simple model including the main plasma species and neutrals, it is possible to analyze basic transport phenomena and get an essential insight into the SOL physics. In principle, to extend the model and add other species would be rather straightforward concerning both the numerics and the adaptation of the solvers. Also the physical aspects and the description by fluid equations would not change significantly and the range of collision processes would broaden with regard to the knowledge of atomic data.

Collision processes, which are a source or a sink of particles and energy, play an important role in the edge region. The model involves the ionization of neutrals, the charge exchange, the excitation and the recombination.

Simulated conditions are illustrated in Fig. 11.1. The model is solved along the SOL between two targets. The mass and energy balance of plasma species is determined by collision processes and a particle and energy input from the core region. Neutrals are produced either by the recombination or during a recycling process at the divertor targets, while the ionization constitutes a sink action. There is no source of the neutrals from the main plasma or a cross-field sink.

The development of the model was supported by discussions with R. Zagórski.

11.2 Mathematical description

11.2.1 Fluid equations

The model of plasma species is based on Braginski-like equations [68]. The same system was used in [101]. The fluid description involves the continuity equation for ions, the momentum equation for ions and the energy equation both for ions and electrons. The electron density and velocity follow an assumption of the charge neutrality $n_\mathrm{e} = n_\mathrm{i}$ and the ambipolar transport (the absence of an electric current). The initial set of the fluid equations solved for the ions and electrons is constituted by the mass, momentum and energy balance

$$\frac{\partial n_\mathrm{i}}{\partial t} + \frac{\partial}{\partial x}(n_\mathrm{i} u_\mathrm{i}) = S_\mathrm{i}^n, \tag{11.1}$$

$$\frac{\partial}{\partial t}(m_\mathrm{i} n_\mathrm{i} u_\mathrm{i}) + \frac{\partial}{\partial x}\left(m_\mathrm{i} n_\mathrm{i} u_\mathrm{i}^2 - \eta_\mathrm{i}\frac{\partial u_\mathrm{i}}{\partial x}\right) = -\frac{\partial p_\mathrm{i}}{\partial x} + e n_\mathrm{i} E + R_\mathrm{i} + m_\mathrm{i} S_\mathrm{i}^u, \tag{11.2}$$

$$\frac{\partial}{\partial t}\left(\frac{3}{2} n_\mathrm{e} k T_\mathrm{e}\right) + \frac{\partial}{\partial x}\left(\frac{5}{2} u_\mathrm{e} n_\mathrm{e} k T_\mathrm{e} + q_\mathrm{e}\right) = -e n_\mathrm{e} u_\mathrm{e} E + u_\mathrm{e} R_\mathrm{e} + Q_\mathrm{e} + S_\mathrm{e}^E, \tag{11.3}$$

$$\frac{\partial}{\partial t}\left(\frac{3}{2} n_\mathrm{i} k T_\mathrm{i} + \frac{1}{2} m_\mathrm{i} n_\mathrm{i} u_\mathrm{i}^2\right) + \frac{\partial}{\partial x}\left(\frac{5}{2} u_\mathrm{i} n_\mathrm{i} k T_\mathrm{i} + \frac{1}{2} m_\mathrm{i} n_\mathrm{i} u_\mathrm{i}^3 + q_\mathrm{i} - u_\mathrm{i}\eta_\mathrm{i}\frac{\partial u_\mathrm{i}}{\partial x}\right) = \\ e n_\mathrm{i} u_\mathrm{i} E + u_\mathrm{i} R_\mathrm{i} + Q_\mathrm{i} + S_\mathrm{i}^E \tag{11.4}$$

and solves for parallel profiles of plasma parameters – the ion density n_i, the parallel ion velocity u_i, the electron temperature T_e and the ion temperature T_i. S_i^n, S_i^u, S_e^E and S_i^E are sources of the mass, momentum and energy of electrons or ions, p_i is the ion pressure and q_e and q_i are the thermal heat fluxes. R_e and R_i ($R_\mathrm{e} = -R_\mathrm{i}$) are the thermal and friction forces, E is the parallel electric field and Q_e and Q_i ($Q_\mathrm{e} = -Q_\mathrm{i}$) is the heating due to electron-ion collisions. The equations (11.2) and (11.4) allow for viscous effects described by the ion viscosity η_i. According to a standard description, the kinetic terms of the electron energy balance are negligible and they are not included.

A final system of the equations solved in the code follows from the equations (11.1)–(11.4) by applying further modifications. We use the generalized Ohm's law for the calculation of the parallel electric field (the momentum equation neglecting inertia)

$$e n_\mathrm{e} E = -\frac{\partial p_\mathrm{e}}{\partial x} + R_\mathrm{e}. \tag{11.5}$$

Together with already mentioned assumption of the ambipolarity $u_\mathrm{e} = u_\mathrm{i}$ it is possible and desirable to modify the equations so that the electric field E and the friction terms R_e and R_i will not appear explicitly in the solved system. The equations can be further modified and schematically rewritten to the following form

$$\frac{\partial}{\partial t}\left(a^n n_\mathrm{i}\right) + b^n \frac{\partial}{\partial x}\left(v^n n_\mathrm{i}\right) = S^n_\mathrm{EXP} - n_\mathrm{i} S^n_\mathrm{IMP}, \tag{11.6}$$

$$\frac{\partial}{\partial t}\left(a^u u_\mathrm{i}\right) + b^u \frac{\partial}{\partial x}\left(v^u u_\mathrm{i}\right) + c^u \frac{\partial}{\partial x}\left(d^u \frac{\partial u_\mathrm{i}}{\partial x}\right) = S^u_\mathrm{EXP} - u_\mathrm{i} S^u_\mathrm{IMP}, \tag{11.7}$$

$$\frac{\partial}{\partial t}\left(a^{T_\mathrm{e}} T_\mathrm{e}\right) + b^{T_\mathrm{e}} \frac{\partial}{\partial x}\left(v^{T_\mathrm{e}} T_\mathrm{e}\right) + c^{T_\mathrm{e}} \frac{\partial}{\partial x}\left(d^{T_\mathrm{e}} \frac{\partial T_\mathrm{e}}{\partial x}\right) = S^{T_\mathrm{e}}_\mathrm{EXP} - T_\mathrm{e} S^{T_\mathrm{e}}_\mathrm{IMP1} - T_\mathrm{i} S^{T_\mathrm{e}}_\mathrm{IMP2}, \tag{11.8}$$

$$\frac{\partial}{\partial t}\left(a^{T_\mathrm{i}} T_\mathrm{i}\right) + b^{T_\mathrm{i}} \frac{\partial}{\partial x}\left(v^{T_\mathrm{i}} T_\mathrm{i}\right) + c^{T_\mathrm{i}} \frac{\partial}{\partial x}\left(d^{T_\mathrm{i}} \frac{\partial T_\mathrm{i}}{\partial x}\right) = S^{T_\mathrm{i}}_\mathrm{EXP} - T_\mathrm{i} S^{T_\mathrm{i}}_\mathrm{IMP1} - T_\mathrm{e} S^{T_\mathrm{i}}_\mathrm{IMP2}, \tag{11.9}$$

which is more convenient and easier to solve. The equations are non-linear and the coefficients a, b, c, d, v and sources S_EXP and S_IMP are functions of the density, velocity and temperature. S_EXP and S_IMP denotes that a part of the sources is treated explicitly (EXP), while a part is handled implicitly (IMP) and it will be further discussed in section 11.3.

11.2.2 Source terms

The source terms of the equations (11.1)–(11.4) describe changes of the mass, momentum and energy of the plasma species due to atomic processes – the ionization, charge exchange, recombination and excitation. In addition, they also comprise external terms describing the amount of energy and mass flows from the core region to the edge. The sources are defined as follows:

$$S^n_\mathrm{i} = n_0 n_\mathrm{i} \langle\sigma v\rangle_\mathrm{ION} - n_\mathrm{i}^2 \langle\sigma v\rangle_\mathrm{REC} + S^n_\mathrm{EXT}, \tag{11.10}$$

$$S^u_\mathrm{i} = n_0 n_\mathrm{i} u_0 \langle\sigma v\rangle_\mathrm{ION} + n_0 n_\mathrm{i}(u_0 - u_\mathrm{i})\langle\sigma v\rangle_\mathrm{CX} + n_\mathrm{i}^2 (u_0 - u_\mathrm{i})\langle\sigma v\rangle_\mathrm{REC}, \tag{11.11}$$

$$S^E_\mathrm{e} = -n_0 n_\mathrm{i} \langle\sigma v\rangle_\mathrm{ION} k I_\mathrm{H} - n_0 n_\mathrm{i} k Q_\mathrm{H} + S^E_\mathrm{EXT}, \tag{11.12}$$

$$\begin{aligned} S^E_\mathrm{i} &= n_0 n_\mathrm{i} \langle\sigma v\rangle_\mathrm{ION} \left(\frac{3}{2} k T_0 + \frac{1}{2} m_0 u_0^2\right) \\ &\quad + n_0 n_\mathrm{i} \langle\sigma v\rangle_\mathrm{CX} \left[\frac{3}{2} k (T_0 - T_\mathrm{i}) + \frac{1}{2} m_0 (u_0^2 - u_\mathrm{i}^2)\right] \\ &\quad + n_\mathrm{i}^2 \langle\sigma v\rangle_\mathrm{REC} \left(\frac{3}{2} k T_\mathrm{i} + \frac{1}{2} m_0 u_\mathrm{i}^2\right) + S^E_\mathrm{EXT}. \end{aligned} \tag{11.13}$$

S^n_EXT and S^E_EXT are external cross-field sources of particles and energy, I_H is the ionization potential ($I_\mathrm{H} = 13.6$ eV for hydrogen ions), Q_H is the cooling rate due to the excitation and the terms $\langle\sigma v\rangle_\mathrm{ION}$, $\langle\sigma v\rangle_\mathrm{CX}$ and $\langle\sigma v\rangle_\mathrm{REC}$

describe rates of the ionization, charge exchange and recombination, respectively. The reaction rate coefficients are, in general, functions of the electron temperature and density. Atomic data implemented in the code were provided by R. Zagórski and the dependence of the reaction rate coefficients on the electron temperature is plotted in Fig. 11.2.

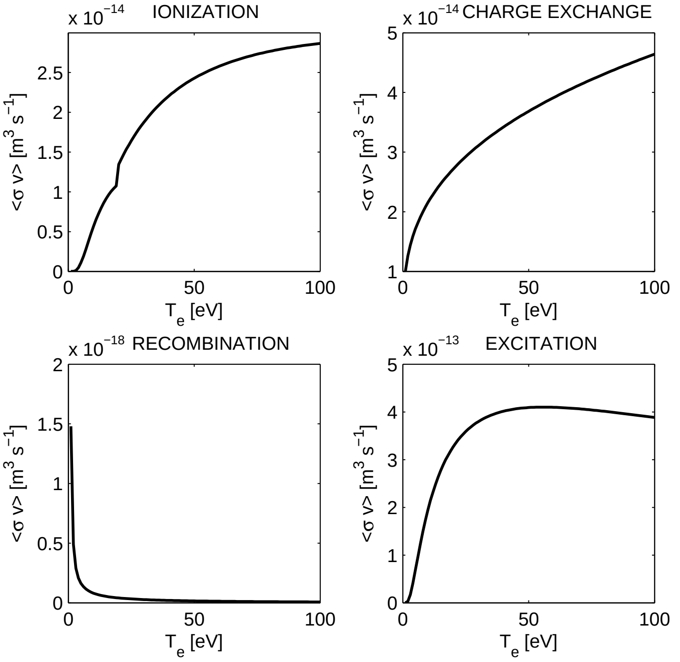

Figure 11.2: The reaction rate coefficients $\langle \sigma v \rangle$ for the ionization, charge exchange, recombination and excitation as functions of the electron temperature T_e.

11.2.3 Transport properties

The classical transport is assumed and all transport coefficients used in the model follow expressions given in [67]. The formulas for the ion viscosity η_i, the thermal gradient heat fluxes q_e and q_i and the ion heating Q_i are as follows:

$$q_\mathrm{e} = -\kappa_\mathrm{e} \frac{\partial}{\partial x} \left(k T_\mathrm{e} \right), \tag{11.14}$$

$$q_\mathrm{i} = -\kappa_\mathrm{i} \frac{\partial}{\partial x} \left(k T_\mathrm{i} \right), \tag{11.15}$$

$$Q_\mathrm{i} = \frac{3 m_\mathrm{e}}{m_\mathrm{i}} \frac{n_\mathrm{i} k}{\tau_\mathrm{e}} \left(T_\mathrm{e} - T_\mathrm{i} \right), \tag{11.16}$$

$$\eta_\mathrm{i} = 0.96 n_\mathrm{i} k T_\mathrm{i} \tau_\mathrm{i} \tag{11.17}$$

with the thermal conductivities κ_{e} and κ_{i} and the collision times τ_{e} and τ_{i}

$$\kappa_{\mathrm{e}} = 3.2\frac{n_{\mathrm{e}}kT_{\mathrm{e}}\tau_{\mathrm{e}}}{m_{\mathrm{e}}}, \tag{11.18}$$

$$\kappa_{\mathrm{i}} = 3.9\frac{n_{\mathrm{i}}kT_{\mathrm{i}}\tau_{\mathrm{i}}}{m_{\mathrm{i}}}, \tag{11.19}$$

$$\tau_{\mathrm{e}} = \frac{3\sqrt{m_{\mathrm{e}}}(kT_{\mathrm{e}})^{3/2}}{4\sqrt{2\pi}n_{\mathrm{e}}\lambda e^4} = 3.44\times 10^{11}\frac{T_{\mathrm{e}}^{3/2}}{n_{\mathrm{e}}\lambda}\mathrm{sec}, \tag{11.20}$$

$$\tau_{\mathrm{i}} = \frac{3\sqrt{m_{\mathrm{i}}}(kT_{\mathrm{i}})^{3/2}}{4\sqrt{\pi}n_{\mathrm{i}}\lambda e^4} = 2.09\times 10^{13}\frac{T_{\mathrm{i}}^{3/2}}{n_{\mathrm{i}}\lambda}\sqrt{\frac{m_{\mathrm{i}}}{m_{\mathrm{p}}}}\mathrm{sec} \tag{11.21}$$

where m_{p} is the proton mass. The coulomb logarithm λ is a function of the density and temperature. The dependence can be found in [67] or [62], however, for the sake of simplicity, we take the value $\lambda = 17$ without loss of generality, although expressions from [67] and [62] are also implemented in the code. The model works with the SI units except for the temperature expressed in electronvolts and the Boltzmann constant $k = 1.6\times 10^{-19}$ J/eV.

Following a standard approach of the fluid modelling, kinetic corrections in the form of flux limiters were included. The classical value of the thermal heat flux q_{CL} both for electrons and ions is modified as

$$q = \left(\frac{1}{q_{\mathrm{lim}}} + \frac{1}{q_{\mathrm{CL}}}\right)^{-1} \tag{11.22}$$

using the maximum acceptable flux $q_{\mathrm{lim}} = \alpha n v^{\mathrm{th}} kT$ and thus limiting the heat conductivity as the classical heat conductivity would diverge for large temperatures. The modified expression for the heat conductivity can be easily derived from the equation (11.22) as

$$\kappa = \left(1 + \frac{\kappa_{\mathrm{CL}}\left|\frac{\partial T}{\partial x}\right|}{\alpha n v^{\mathrm{th}} T}\right)^{-1}\kappa_{\mathrm{CL}}. \tag{11.23}$$

Similarly, a modified expression can be derived for the ion viscosity using the limit βnkT_{i}. As a result of kinetic studies, values of the heat flux limiters are observed in the range $0.03 \leq \alpha \leq 0.6$ with the average value $\langle\alpha\rangle \approx 0.15\pm0.05$ and $\langle\beta\rangle \approx 0.5\pm0.1$ for the viscosity. The limiters are functions of the parallel coordinate x as well as they change in a time-dependent case (the turbulent transport, ELMs, etc) and their precise estimation requires a kinetic analysis. Therefore in the work presented in this chapter, the flux limiters are not used and the transport coefficients follow the classical Braginskii expressions. One exception has been made in case of the ion viscosity which was artificially lowered as it will be mentioned later.

11.2.4 Model of neutrals

The model of neutral atoms is governed by the fluid description. A different possible approach is described in chapter 12. The fluid model comprises the continuity and momentum transfer equation

$$\frac{\partial n_0}{\partial t} + \frac{\partial}{\partial x}(n_0 u_0) = S_0^n, \tag{11.24}$$

$$\frac{\partial}{\partial t}(m_0 n_0 u_0) + \frac{\partial}{\partial x}\left(m_0 n_0 u_0^2\right) = -\frac{\partial p_0}{\partial x} + m_0 S_0^u \tag{11.25}$$

for the density of the neutrals n_0 and their parallel velocity u_0. The set of equations is complete with an assumption about the energy of the neutrals that are considered to have the temperature locally equal to the ion temperature $T_0 = T_\mathrm{i}$. In plasma conditions in the edge region, it is expected that the neutrals are close to a local thermal equilibrium with the ions due to the dominant charge exchange process [102]. The source and sink terms S_0^n and S_0^u define changes of the density and momentum of the neutrals caused by collisions with the plasma species. Finally, p_0 is the pressure of the neutrals and m_0 is their mass. The sources are defined as

$$S_0^n = -n_0 n_\mathrm{i} \langle \sigma v \rangle_\mathrm{ION} + n_\mathrm{i}^2 \langle \sigma v \rangle_\mathrm{REC}, \tag{11.26}$$

$$S_0^u = -n_0 n_\mathrm{i} u_0 \langle \sigma v \rangle_\mathrm{ION} - n_0 n_\mathrm{i} (u_0 - u_\mathrm{i}) \langle \sigma v \rangle_\mathrm{CX} - n_\mathrm{i}^2 (u_0 - u_\mathrm{i}) \langle \sigma v \rangle_\mathrm{REC}. \tag{11.27}$$

There is no external source or sink for neutrals, the core plasma is fully ionized and besides collision events, the neutral atoms are generated only at the divertor targets during the recycling. The recycling appears in the model through a boundary condition imposed on the neutral density (see section 11.3.3).

11.3 Computational method

The equations in the model are strongly coupled and nonlinear. In order to solve the system, an algorithm based on the finite difference approach (section 2.4) has been implemented. The equations are linearized and discretized on a non-uniform staggered grid using traditional numerical schemes.

Some terms are treated implicitly to maintain the stability. The time step is calculated automatically and its value is limited to satisfy the Courant-Friedrichs-Lewy stability condition and varies during a run of the code according to dynamics of the system. The condition applied to the time step limits the time interval with respect to the plasma velocity u_i and the grid spacing Δx. We use a rough estimate

$$\Delta t_\mathrm{limit} \approx \frac{\Delta x}{u_\mathrm{i}}. \tag{11.28}$$

To resolve steep gradients of the functions that may develop close to the boundaries, a non-uniform exponential grid is used with higher resolution in regions near the targets. In addition, the variables are discretized on a staggered grid to prevent oscillations that might occur in a non-staggered case. Different variables are placed on different grids which are shifted half a grid point.

11.3.1 Technique of discretization

The equations are solved one by one in a semi-implicit way with the forward time-stepping until the system converges to a steady-state solution. Different algorithms are applied to discretize the equations in the spatial coordinate. The discretization technique for converting the spatial derivatives to algebraic expressions is of the second-order accuracy. The second-order upwind scheme (the donor cell scheme) is used to transform the convective terms of the equations (11.6)–(11.9), even though e.g. the FCT algorithm (see section 5.2.2) could be used too. Let us assume an advection equation for a function f and an advective velocity v of the form

$$\frac{\partial}{\partial t}(af) = b\frac{\partial}{\partial x}(vf) \tag{11.29}$$

and a grid with a uniform spacing Δx. The discretization using the upwind scheme for the spatial derivative and the forward time-stepping (index k) results in the following difference equation for a nodal point i of the grid

$$\frac{a^{k+1}f^{k+1} - a^k f^k}{\Delta t} = b^k \frac{F^k_{i+\frac{1}{2}} - F^k_{i-\frac{1}{2}}}{\Delta x} \tag{11.30}$$

where

$$F_{i+\frac{1}{2}} = \begin{cases} f_i v_{i+\frac{1}{2}} & v_{i+\frac{1}{2}} > 0 \\ f_{i+1} v_{i+\frac{1}{2}} & v_{i+\frac{1}{2}} < 0 \end{cases}, \tag{11.31}$$

$$F_{i-\frac{1}{2}} = \begin{cases} f_{i-1} v_{i-\frac{1}{2}} & v_{i-\frac{1}{2}} > 0 \\ f_i v_{i-\frac{1}{2}} & v_{i-\frac{1}{2}} < 0 \end{cases}. \tag{11.32}$$

The diffusive terms of the equations (11.7)–(11.9) are discretized using the standard Crank-Nicholson scheme [22]. Let us assume a diffusion equation of the form

$$\frac{\partial}{\partial t}(af) = c\frac{\partial}{\partial x}\left(d\frac{\partial f}{\partial x}\right). \tag{11.33}$$

With the Crank-Nicholson technique, we can replace the partial differential equation (11.33) by corresponding finite difference expressions

$$\frac{a^{k+1}f^{k+1} - a^k f^k}{\Delta t} = \lambda c_i^{k+1}\frac{F^{k+1}_{i+\frac{1}{2}} - F^{k+1}_{i-\frac{1}{2}}}{\Delta x} + (1-\lambda)c_i^k\frac{F^k_{i+\frac{1}{2}} - F^k_{i-\frac{1}{2}}}{\Delta x} \tag{11.34}$$

where

$$F \equiv d\frac{\partial f}{\partial x} \tag{11.35}$$

and

$$F_{i+\frac{1}{2}} = d_{i+\frac{1}{2}}\frac{f_{i+1} - f_i}{\Delta x}, \tag{11.36}$$

$$F_{i-\frac{1}{2}} = d_{i-\frac{1}{2}}\frac{f_i - f_{i-1}}{\Delta x}. \tag{11.37}$$

The parameter λ ranges from 0 (the explicit case) to 1 (the fully implicit case). Here the semi-implicit approach with $\lambda = \frac{1}{2}$ is applied.

To avoid the numerical instability, the implicit approach is also used for a part of the source terms which can be written in the form $S = -fS_{\text{IMP}}$ with $S_{\text{IMP}} > 0$, see the equations (11.6)–(11.9). It means that S_{IMP} is expressed in the updated $(k+1)$ time level in the discretized equations.

11.3.2 Algorithm for solving system of linear equations

Once the equations are discretized, a system of algebraic equations must be solved. While solving the momentum equation (11.7) leads to a system of linear equations with a simple tridiagonal matrix, the temperature equations must be handled more carefully. The implicit treatment of the source terms in the equations (11.8) and (11.9) couple both equations together so that they must be solved as a one system in each time step.

The linear system with the three-diagonal matrix is solved by the Progonka method that is similar to the well-known Thomas algorithm. For a tridiagonal system of unknown functions f of the form

$$A_i f_{i-1} + B_i f_i + C_i f_{i+1} = R_i \tag{11.38}$$

with coefficients A_i, B_i, C_i and the right-hand side terms R_i, the Progonka prescribes the recursive formula

$$f_i = \alpha_{i+1} f_{i+1} + \beta_{i+1} \tag{11.39}$$

with coefficients

$$\alpha_{i+1} = -\frac{C_i}{A_i \alpha_i + B_i}, \tag{11.40}$$

$$\beta_{i+1} = \frac{R_i - A_i \beta_i}{A_i \alpha_i + B_i}. \tag{11.41}$$

The algorithm is based on two cycles. At first, the coefficients α_{i+1} and β_{i+1} are computed at each point i from the expressions (11.40) and (11.41) starting at the left boundary with a boundary condition and going to the right boundary point. In the second cycle, the unknowns f_i are computed at each point i according to the recurrent formula (11.39). The procedure starts at the right boundary, where the solution is given by a boundary condition, and runs back to the left boundary point.

To solve the system of linear equations given by the difference form of the temperature equations (11.8) and (11.9), the Matrix Progonka (a matrix formulation of the Progonka method) was applied. The algorithm and the recursive formulation is the same as described above, but the coefficients $\mathbb{A}_i$, $\mathbb{B}_i$, $\mathbb{C}_i$, α_{i+1} and β_{i+1} are 2×2 matrices and the unknowns $\mathbf{f}_i$ and the right-hand side terms $\mathbf{R}_i$ are vectors. The system

$$\mathbb{A}_i \mathbf{f}_{i-1} + \mathbb{B}_i \mathbf{f}_i + \mathbb{C}_i \mathbf{f}_{i+1} = \mathbf{R}_i \tag{11.42}$$

is solved using analogical recursive formulas in the matrix representation

$$\mathbf{f}_i = \alpha_{i+1} \mathbf{f}_{i+1} + \beta_{i+1}, \tag{11.43}$$

$$\alpha_{i+1} = -\left(\mathbb{A}_i \alpha_i + \mathbb{B}_i\right)^{-1} \mathbb{C}_i, \tag{11.44}$$

$$\beta_{i+1} = \left(\mathbb{A}_i \alpha_i + \mathbb{B}_i\right)^{-1} \left(\mathbf{R}_i - \mathbb{A}_i \beta_i\right). \tag{11.45}$$

11.3.3 Boundary conditions

The description of the fluid model is closed by boundary conditions required for the equations (11.1)–(11.4) and (11.24)–(11.25). The boundary conditions imposed on the ion density n_i, the ion velocity u_i, the ion and electron temperatures T_i and T_e, the neutral density n_0 and the neutral velocity u_0 are summarized in Tab. 11.1. The standard sheath boundary conditions were applied for the plasma species (section 8.2). The boundary value of the

function	boundary condition
n_i	open
u_i	Dirichlet
T_i	Newton
T_e	Newton
n_0	Dirichlet
u_0	Dirichlet

Table 11.1: Boundary conditions of the model.

density n_i is an extrapolated value calculated from values at neighbouring points inside the computational domain. The boundary value of the velocity u_i is equal to the sound speed

$$c_\mathrm{s} = \sqrt{\frac{k(T_\mathrm{e} + T_\mathrm{i})}{m_\mathrm{i}}} \tag{11.46}$$

which agrees with the Bohm criterion (section 8.2). The boundary conditions for the temperatures T_i and T_e are nonlinear and should be treated carefully. A general Newton form can be derived after linearization from the assumed sheath boundary conditions from section 8.2 specifying the boundary value of the total heat fluxes Q_i and Q_e

$$Q_\mathrm{i} = \delta_\mathrm{i} k T_\mathrm{i} n_\mathrm{i} u_\mathrm{i}, \tag{11.47}$$

$$Q_\mathrm{e} = \delta_\mathrm{e} k T_\mathrm{e} n_\mathrm{e} u_\mathrm{e}. \tag{11.48}$$

The constant values $\delta_\mathrm{i} = 3.5$ and $\delta_\mathrm{e} = 5.0$ are assumed for the energy transmission coefficients, the same values were used e.g. in [103].

The neutral model uses boundary conditions determined by the recycling process (section 8.2). The plasma is neutralized on the solid surface and resulting neutrals are soon ionized again in the divertor so that the plasma species and the neutrals act in a repetitive process (the recycling). The neutral influx Γ_0 from the divertor targets to the plasma is specified by the recycling coefficient R. It follows the expression

$$\Gamma_0 = -R\Gamma_\mathrm{i}. \tag{11.49}$$

The boundary value of the neutral velocity is assumed to be equal to the thermal speed

$$v_0^\mathrm{th} = \sqrt{\frac{kT_0}{m_0}}. \tag{11.50}$$

11.4 Results

11.4.1 Input parameters

Main input parameters of the model are the size of the computational region L (the parallel length, see Fig. 11.1) and the sources of particles and energy from the main plasma S^n_{EXT} and S^E_{EXT}, see equations (11.10)–(11.13). For a basic analysis or testing purposes, some ad hoc values of these parameters can be chosen, nevertheless, in a real situation, the parallel length L is a function of the geometry of the device and its operational regime. Further, it is convenient to work with total sources Q^n [s^{-1}] and Q^E [W] (the total particle and power flow rates from the main plasma into the SOL) instead of the differential sources S^n_{EXT} [m^{-3}s^{-1}] and S^E_{EXT} [kgm^{-1}s^{-3}]

$$S^E_{\mathrm{EXT}} = \frac{Q^E}{V_{\mathrm{SOL}}}, \tag{11.51}$$

$$S^n_{\mathrm{EXT}} = \frac{Q^n}{V_{\mathrm{SOL}}}. \tag{11.52}$$

The volume of the SOL $V_{\mathrm{SOL}} = 4\pi^2 R_{\mathrm{t}} R_{\mathrm{p}} \lambda_{\mathrm{SOL}}$ is estimated using the approximative formula

$$\lambda_{\mathrm{SOL}} = \sqrt{\frac{D_\perp L}{u_\parallel}} \tag{11.53}$$

for the radial width of the SOL λ_{SOL} [62]. For a JET configuration, we can consider typical values of the cross-field particle diffusion coefficient $D_\perp \approx 0.5$ m^{2}s^{-1} and the parallel velocity $u_\parallel \approx 10^5$ ms^{-1}. R_{t} and R_{p} is the major and minor radius (Fig. 8.2).

The following expressions are taken into account to link the model to a real device. The distance along the magnetic field line between the target plates

$$L \approx 2\left(\pi q_{\mathrm{s}} R_{\mathrm{t}} + L_{\mathrm{X}}\right) \tag{11.54}$$

is estimated using the safety factor q_{s}. L_{X} is the distance from the target plate to the X point approximated as $L_{\mathrm{X}} \approx 0.25\pi q_{\mathrm{s}} R_{\mathrm{t}}$. The value of the safety factor depends on geometric properties of the machine – the major and minor radius R_{t} and R_{p} and on operational conditions – specifically on the toroidal magnetic field B_{t} and the total plasma current I_{p}. The equation (8.2) in section 8.1 together with Ampere's law $B_{\mathrm{p}} \approx \mu_0 I_{\mathrm{p}}/2\pi R_{\mathrm{p}}$ [62] implies the approximative estimate for the safety factor

$$q_{\mathrm{s}} \approx \frac{R_{\mathrm{p}}^2}{R_{\mathrm{t}}} \frac{2\pi B_{\mathrm{t}}}{\mu_0 I_{\mathrm{p}}}. \tag{11.55}$$

The expressions for L and q_s can be easily modified in the code. Additional input data are the sheath heat transmission factors $\delta_\mathrm{i} = 3.5$ and $\delta_\mathrm{e} = 5.0$. The recycling coefficient $R = 0.975$ has been taken by analogy with the previous chapter. The energy source S^E_EXT is assumed to be equal for electrons and ions as default, however, two different values are allowed as well. The sources of the mass and energy S^n_EXT and S^E_EXT can either be constants, i.e. uniformly distributed along the SOL, or a dependence on the parallel coordinate x can be prescribed. Note that the equations (11.51) and (11.52) give constant values of the source for uniformly distributed sources, while in general, $Q^n = \int\limits_\mathrm{SOL} S^n_\mathrm{EXT}\,\mathrm{d}V$ and $Q^E = \int\limits_\mathrm{SOL} S^E_\mathrm{EXT}\,\mathrm{d}V$.

11.4.2 Basic plasma model

A hydrogen plasma composed of electrons and protons is considered. The geometry of the model corresponds to the JET tokamak with the toroidal radius $R_\mathrm{t} = 2.96$ m and the poloidal radius $R_\mathrm{p} = 1$ m and we assume the safety factor $q_\mathrm{s} = 3$. The integral sources of the mass and energy are $Q^n = 5 \times 10^{22}\ \mathrm{s}^{-1}$ and $Q^E = 5 \times 10^6$ W and a uniform distribution of these fluxes along the SOL is assumed.

Fig. 11.3 shows profiles of the plasma density, velocity and temperature in the SOL in the direction parallel to the magnetic field. The solution corresponds to a simple SOL picture (section 8.4) that is characterized by flat temperature profiles and a parabolic-like profile of the density. The temperature goes to relatively high values, while the density is low. In such a case, the plasma pressure at the stagnation point (the upstream position) is roughly twice the value of the pressure at the boundary. It is in agreement with a simplified source-free form of the momentum equation assuming a flat temperature profile and neglecting viscous effects. The simple SOL conditions are typically observed in tokamaks employing limiters and correspond to the low-recycling (or the sheath-limited) regime (section 8.4). The transport is dominated by the convection, there is no ionization in the SOL and no zones of strong recycling develop close to the targets. The sheath region is the only sink for particles and heat, no radiative or charge-exchange cooling is present. The energy exchange between the electrons and ions due to collisions is rather small, thermal equipartition is weak and the electrons and ions are thermally de-coupled from each other. From a numerical point of view, the absence of strong gradients allow to use an equidistant grid.

It should be noted that in a real case, the ion viscosity is smaller than the value calculated from the classical expression (11.17). Therefore the viscosity has been artificially decreased 100 times compared to the value determined

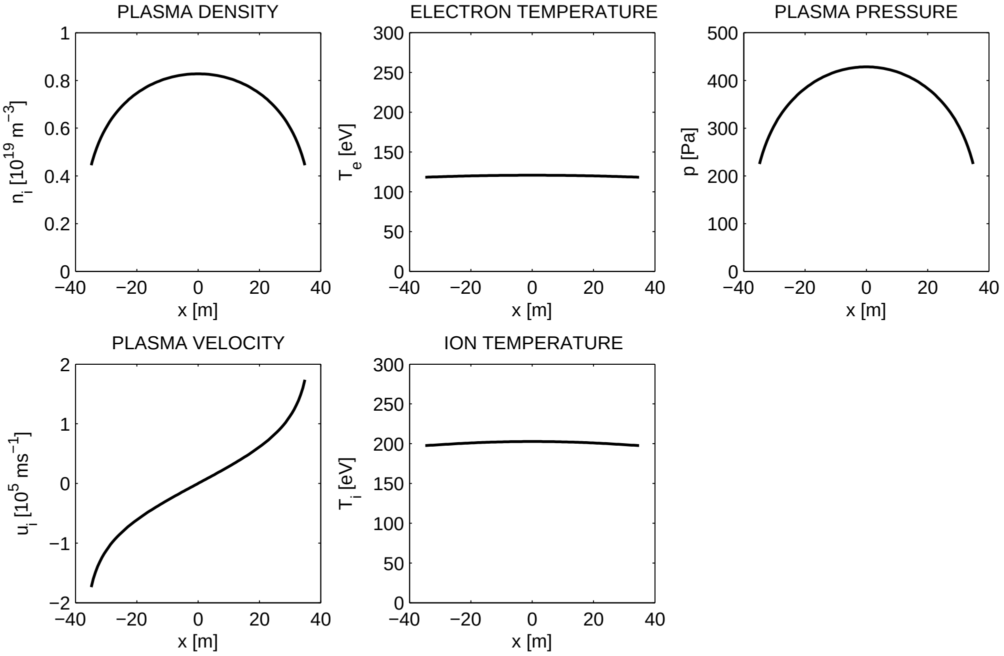

Figure 11.3: Profiles of the ion density n_{i}, the ion velocity u_{i}, the electron temperature T_{e}, the ion temperature T_{i} and the total plasma pressure $p = p_{\mathrm{e}} + p_{\mathrm{i}}$ along the magnetic field line. A model without neutrals and a result corresponding to the simple SOL.

by the formula (11.17) for all calculations presented in this chapter, unless stated otherwise.

11.4.3 Influence of neutrals

The effect of plasma-neutral collisions, mainly the ionization, on the plasma transport in the SOL and the character of parallel profiles of the plasma parameters is significant (section 8.4). The solution in Fig. 11.4 was obtained with the same input parameters as in the previous case ($R_{\mathrm{t}} = 2.96$ m, $R_{\mathrm{p}} = 1$ m, $q_{\mathrm{s}} = 3$, $Q^n = 5 \times 10^{22}$ s^{-1} and $Q^E = 5 \times 10^6$ W) and the code was solving both the model of plasma species and the model of neutrals. The recycling coefficient was $R = 0.975$.

The solution in Fig. 11.4 can be typically observed in divertor devices and it corresponds to a complex SOL picture (section 8.4). The ionization length is much smaller than the spatial scale of the system ($\lambda_{\mathrm{ion}} \ll L$) and the neutrals are concentrated in a region close to the targets where they are almost immediately ionized. The transport is dominated by the con-

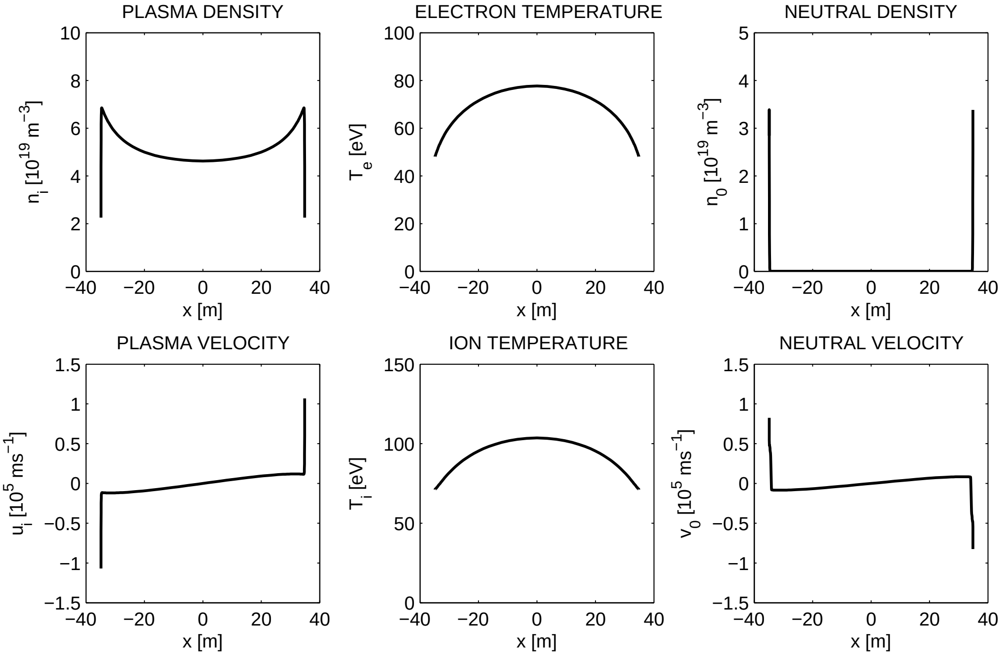

Figure 11.4: Profiles of the ion density n_i, the ion velocity u_i, the electron temperature T_e, the ion temperature T_i, the neutral density n_0 and the neutral velocity u_0 along the magnetic field line. A model with neutrals and a result corresponding to the complex SOL.

duction and recycling zones develop near the targets. The recycling process plays an important role and the machine works in the high-recycling (or the conduction-limited) regime. The ionization in the SOL is an important source of particles. A radiation occurs in the SOL in the divertor and together with the charge exchange cools the plasma. Another feature of the conduction-limited regime is a strong thermal coupling of the electrons and ions. The complex SOL solution is characterized by low target temperatures and high target densities. The temperature profile is not flat any more and steep gradients of the plasma parameters occur at the targets. A non-uniform grid (exponential here) is now necessarily required to obtain a stable solution.

The efficiency of the code depends on considered physical conditions – the input power and the particle source, initial conditions and obviously on numerical aspects – the grid refinement and non-uniformity. The code performance differs for the basic plasma model excluding the neutral atoms and atomic processes and for the full model including the neutral model and calculating rates of the plasma-neutral collisions. One time step of the simulation presented in Fig. 11.3 written in Fortran takes 0.4 ms on a grid with 100 nodal points using the Intel compiler and running on an Intel Core2 Duo 2.4 GHz CPU (a plain code without graphics and output). The time step was roughly $\Delta t = 0.4 \times 10^{-6}$ s and about 1×10^{4} iterations were required to converge to a steady-state solution. One time step of the calculation in Fig. 11.4 takes 0.6 ms. The exponential grid was needed. The time step was approximately $\Delta t = 0.2 \times 10^{-7}$ s and the relaxation required 5×10^{5} iterations. A similar efficiency was achieved also with a second version of the code written in C++.

11.4.4 Dependence on operational conditions

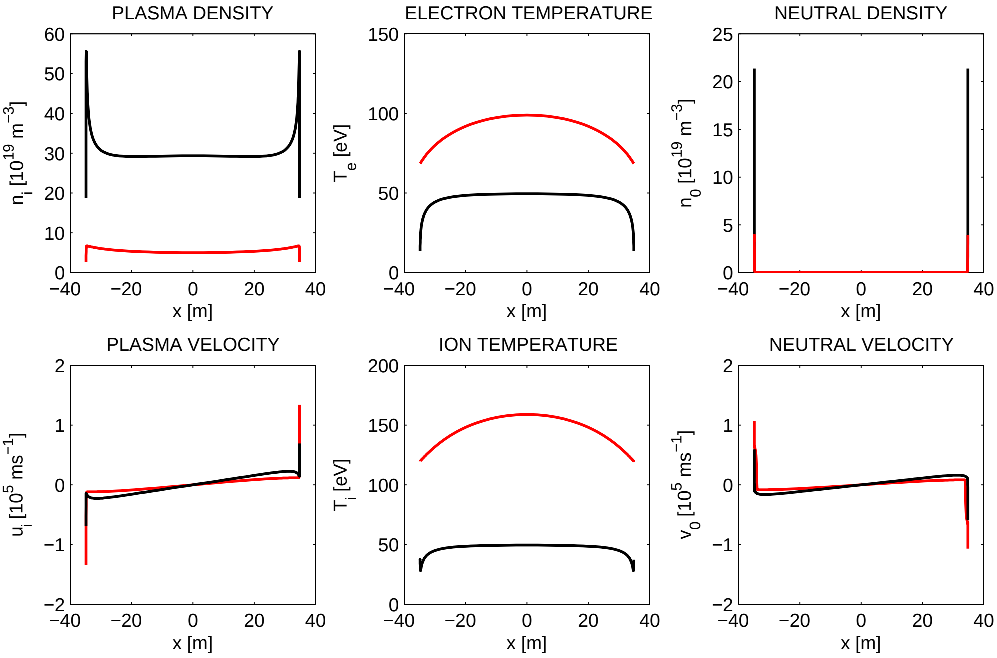

Figure 11.5: Profiles of the ion density n_{i}, the ion velocity u_{i}, the electron temperature T_{e}, the ion temperature T_{i}, the neutral density n_0 and the neutral velocity u_0 along the magnetic field line for $Q^E = 10$ MW and $Q^n = 5 \times 10^{22}$ s^{-1} (red) or $Q^n = 5 \times 10^{23}$ s^{-1} (black).

Operational conditions control the SOL regime of a device and the SOL can be found in a low-recycling state or in a high-recycling regime, eventually a detachment (section 8.4). In chapter 10, the operational conditions were controlled by the toroidal magnetic field B_{t} and the total plasma current I_{p} and it was stated that high values of the magnetic field and the plasma current are desirable concerning the question of achieving a detached regime.

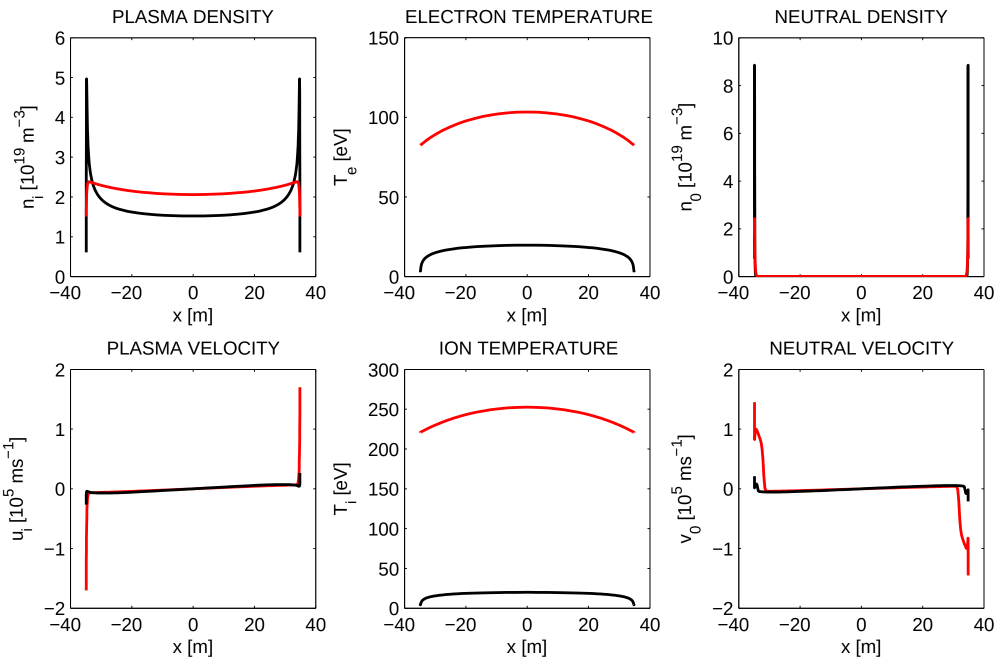

Figure 11.6: Profiles of the ion density n_{i}, the ion velocity u_{i}, the electron temperature T_{e}, the ion temperature T_{i}, the neutral density n_0 and the neutral velocity u_0 along the magnetic field line for $Q^n = 1 \times 10^{22}$ s^{-1} and $Q^E = 1$ MW (red) or $Q^E = 0.1$ MW (black).

Besides these factors, the main plasma density and the total input power are important. The following simulations show the effect of the power and plasma input from the core region Q^E and Q^n on transport properties of the SOL. In Fig. 11.5 and 11.6, solutions for two different values of Q^n and Q^E are plotted and illustrate what happens when we increase or decrease either the particle or the energy source.

In general, we move more to a high-recycling or closer to a detached regime increasing the particle flux and decreasing the energy flux. The plasma density at the targets increases, while the temperature decreases and temperature gradients arise in the divertor. Note that the density and temperature behave inversely, the particle flux to the targets increases as the target temperature drops and the relation $n_{\mathrm{i}u} < n_{\mathrm{i}t}$ for the target and upstream values indexed as t and u corresponds to $T_{\mathrm{i}u} > T_{\mathrm{i}t}$, see the equation (8.11). Neutrals recycling at the targets are localized close to the boundaries. The ionization mean free path decreases and the recycling becomes stronger. The SOL radiation is higher as the electron temperature T_{e} decreases (at a lower T_{e}, more excitations occur before the ionization and the amount of the radiative power loss increases). The conduction-limited regimes can be initiated by increasing the particle source Q^n, thus they can be experimentally achieved at high average densities in the core. See more in [62] about the operational regimes.

Parameters of the model were again: the toroidal radius $R_\mathrm{t} = 2.96$ m, the poloidal radius $R_\mathrm{p} = 1$ m, the safety factor $q_\mathrm{s} = 3$ and the recycling coefficient $R = 0.975$. It should be remarked that the model does not work at temperatures lower than 1 eV. The limit originates from the set of atomic data which provides valid data for $T_\mathrm{e} > 1$ eV only.

11.5 Validation and benchmark

11.5.1 Symmetry verification

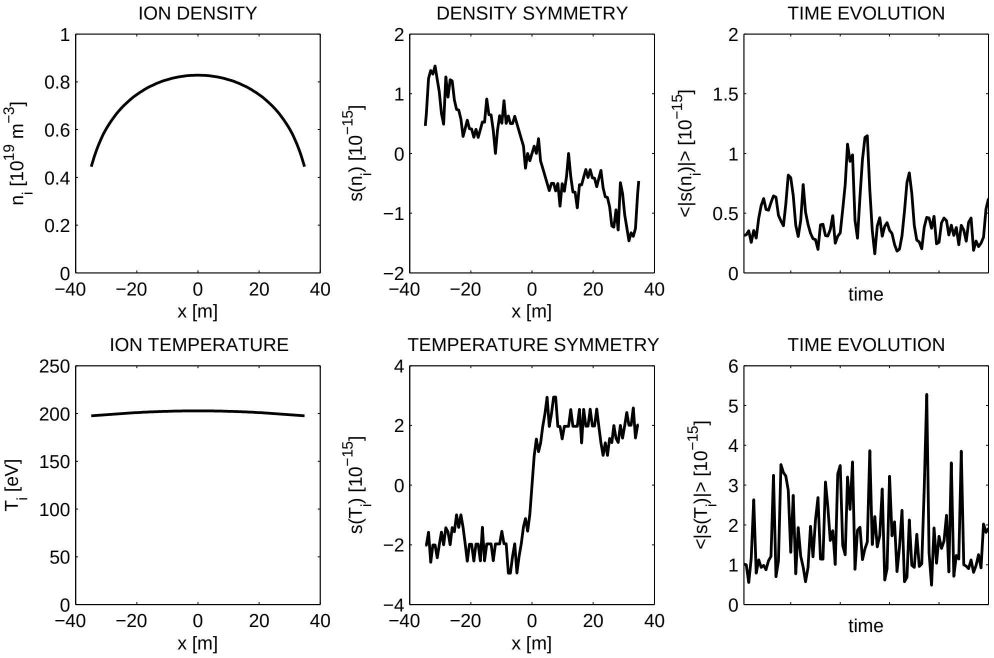

Figure 11.7: The ion density n_i and the ion temperature T_i, the symmetry of the density and temperature and the time evolution of the average value of the density and temperature symmetry. A model without neutrals.

The model has been carefully tested and validated. At first, the symmetry of the solvers has been tested, i.e. it was checked that a symmetric solution is obtained for a symmetric problem. A purpose of this test was to estimate the level of asymmetry regarding troubles with the symmetry that have been

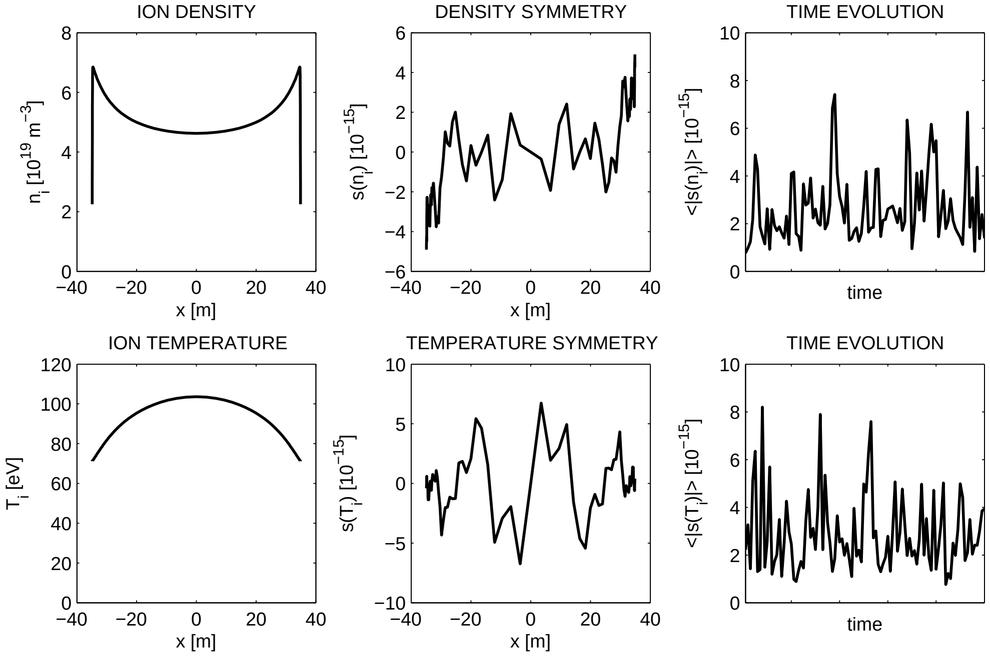

Figure 11.8: The ion density n_i and the ion temperature T_i, the symmetry of the density and temperature and the time evolution of the average value of the density and temperature symmetry. A model with neutrals.

encountered in the one-dimensional version of B2. The solution in Fig. 11.7 and Tab. 11.2 was obtained for a symmetric input and it shows an asymmetry in the order of the machine precision. This asymmetry can be explained by the semi-implicit approach and the algorithms used to solve the system of linear equations. For an explicit technique, the exact symmetry could be achieved in case an exactly symmetric grid is used. Fig. 11.7 shows the level of symmetry of the ion density and temperature in a steady-state solution and the time evolution of a parameter controlling the symmetry to check there is no growing tendency in time.

plasma parameter	**left boundary**	**right boundary**
the ion density n_i [10^{19} m^{-3}]	0.4446984473202611	0.4446984473202609
the ion temperature T_i [eV]	0.1975983112447529	0.1975983112447533

Table 11.2: The boundary values of the ion density and temperature.

The code was run on an equidistant grid with 100 grid points assuming constant and uniform sources of particles and energy ($Q^n = 5 \times 10^{22}$ s^{-1}

and $Q^E = 5 \times 10^6$ W). The grid was exactly symmetric. The parameter of the symmetry plotted in Fig. 11.7 is calculated as a normalized subtract of corresponding values of the variable f on the left and the right side

$$s_i(f) = \frac{f_i - f_{N-i+1}}{f_i} \tag{11.56}$$

where $i = 1, ..., N$ is the index of the spatial discretization.

The symmetry has been tested also for a full model with neutrals using an exponential grid (Fig. 11.8) and also for a time-dependent case, concluding that again, a symmetric solution has been obtained in the order of the computer precision.

11.5.2 Test of conservation

Another essential check of the code is if the mass and energy are conserved in the solved system. Specifically, the input particle and energy sources should balance the outflow at the target plates. The particle and energy balance of the plasma model (a model without neutrals) has been verified for the grid resolutions 100, 200, 400 and 800 nodal points (Fig. 11.9 black squares) and a mesh-independent value (Fig. 11.9 red circle) was estimated by Richardson extrapolation.

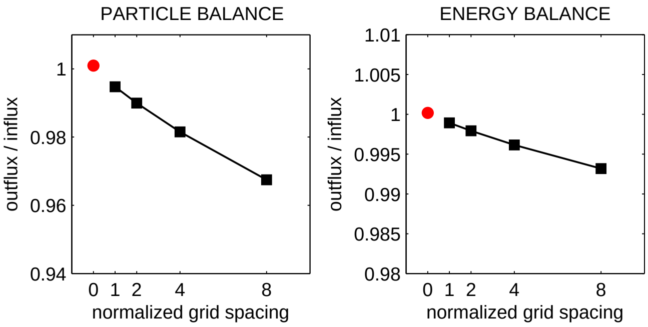

Figure 11.9: Particle and energy balance of the model.

Richardson extrapolation is a method for obtaining a higher-order estimate of the continuum value of a quantity f (the value at zero grid spacing) from series of lower-order discrete values. For a p-th order method and a grid ratio r, Richardson extrapolation gives the mesh-independent value at zero grid spacing Δx using the two finest grids

$$f_{\Delta x=0} \approx f_1 + \frac{f_1 - f_2}{r^p - 1}. \tag{11.57}$$

Traditionally, Richardson extrapolation is being used with the grid refinement ratios $r = 2$. The order of the grid convergence p can be obtained from three solutions using a constant grid refinement ratio r as

$$p = \frac{\ln\left(\frac{f_3 - f_2}{f_2 - f_1}\right)}{\ln(r)}. \tag{11.58}$$

Fig. 11.9 shows the particle and energy balance for various grid resolutions. The value plotted is the ratio of the flux coming into the SOL from the main plasma (which corresponds to $Q^n = 5 \times 10^{22}$ s^{-1} and $Q^E = 5 \times 10^6$ W in this case) and the flux leaving the SOL at the targets. The normalized grid spacing in Fig. 11.9 means a spacing normalized by the spacing of the finest grid. The equation (11.57) gives the mesh-independent value 1.0009371 for the particle balance and 1.0001752 for the energy conservation.

11.5.3 Benchmark with B2

A simple case has been set to compare results of the code with results from another fluid model, the one-dimensional version of B2 [66]. The model described in Tab. 11.3 was considered with identical parameters in both codes.

plasma	a hydrogen plasma
neutral model	no neutrals
transport	classical
grid	an equidistant grid, $L = 15$ m
sources	uniform and constant sources $S^n = 3 \times 10^{23}$ m^{-3}s^{-1}, $S^E = 1 \times 10^7$ kg m^{-1}s^{-3}

Table 11.3: Parameters of the model.

Since the full model is rather complex, the benchmark has been started step by step, first for a simplified case when the temperature is fixed to the constant value 60 eV and only the continuity and momentum equations are solved. The boundary conditions were tested in this case taking into account different grid refinements. Using Richardson extrapolation to estimate a mesh-independent value of the density at the boundary, we have obtained good agreement in the boundary conditions. The tested code gives the value 2.100448×10^{19} m^{-3} and B2 gives 2.09863×10^{19} m^{-3}. It was found that perfect agreement of solutions (Fig. 11.10) can be obtained if flux limiters are switched off in B2 and if the grid resolution is fine enough. Fig. 11.11 shows

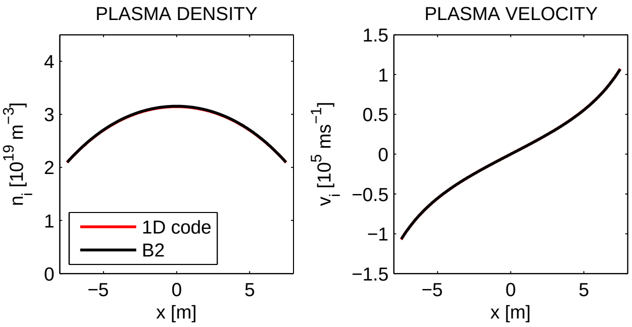

Figure 11.10: A comparison of the plasma density and velocity from the one-dimensional tested code and from B2 for 400 grid points.

solutions for three different grid refinements. The ion viscosity was fixed to the constant value $\eta_\mathrm{i} = 0.01$ kg m^{-1}s^{-1}, because the codes do not use exactly the same expressions for transport coefficients and at higher temperatures, the viscous effects could visibly influence the solution. The next step is to compare solutions of the full system of equations including the electron and ion energy balance.

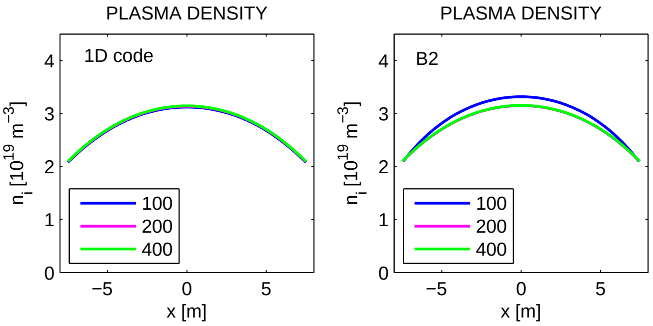

Figure 11.11: The density profiles for three different grid refinements (100, 200 and 400 grid nodes).

11.6 Application to time-dependent problems

The model has been initially developed to solve steady state problems, however, it is possible to apply it also to time-dependent problems if the time step is small enough to resolve the dynamics of the studied phenomenon. It further extends the area where the code can be applied and makes the code usable for various kinds of transient studies. One possible application is to study parallel flows of plasma particles and energy and response on targets of a tokamak if intermittent structures known as plasma blobs develop in the edge, representing transient cross-field flows of the mass and energy.

The anomalous radial transport in the edge in not well-understood yet, but it is accepted to be caused by a plasma turbulence. Experimental investigations and modelling of rapid turbulent flows and intermittent structures in the tokamak edge region contribute to better understanding of these phenomena and a number of codes has been developed to study the turbulent transport (see chapter 9).

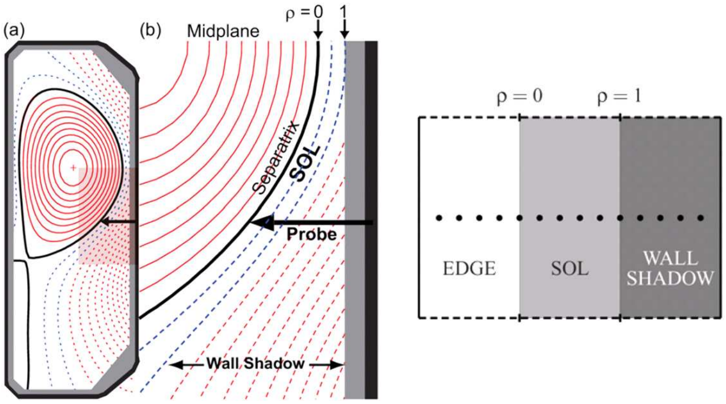

Figure 11.12: A sketch of the simulation domain in ESEL.

The ESEL code [104] simulates electrostatic interchange turbulence in two-dimensional geometry in poloidal cross-section at the outboard midplane of a tokamak (Fig. 11.12). The computational region involves the SOL and the wall region where magnetic field lines are open and cross divertor targets. In these regions, the transport of particles and energy along the magnetic field to the targets is simplified in the form of an analytic model valid for steady-state and simple SOL conditions [105]. The description of the parallel transport is considered as the main weakness of the ESEL model. The analytic model assumes that the energy transport is due to the heat conduction and at low collisionalities, when the power is not carried only by the heat conduction and convective transport may become important, a kinetic correction known as the heat flux limiter is introduced (see section 11.2.3). The assumption of the sheath-limited regime makes further constrains and physics can change under complex SOL conditions when we can observe a strong recycling of neutrals at the targets. In addition, an important point is the influence of dynamics on parallel losses which can be significant and a comparison with experimental observations shows that more precise treatment of parallel flows in ESEL is desirable. The following work aims to prepare the one-dimensional fluid code for future coupling with ESEL, to replace the simple analytic description of the parallel transport and calculate parallel losses of particles and energy dynamically and consistently with the radial transport of ESEL.

11.6.1 Comparison with analytic model for steady state

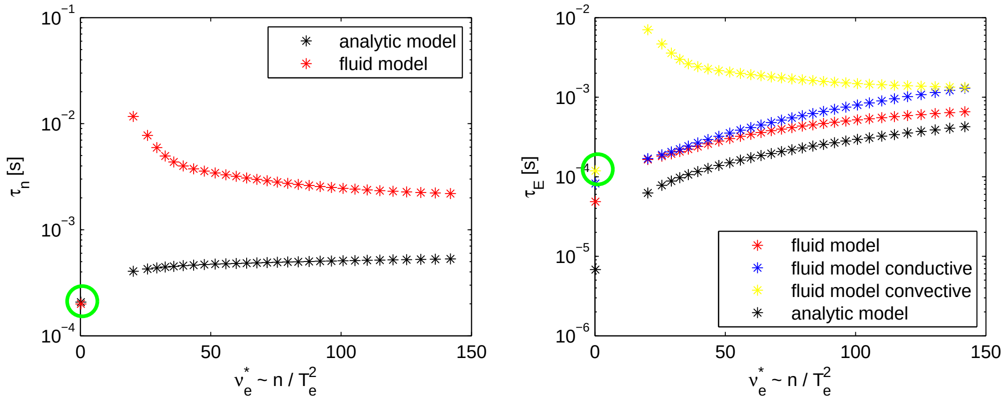

Figure 11.13: The parallel particle density and energy loss times τ_n and τ_E as functions of the electron collisionality ν_e^*. A comparison of the fluid and analytic models.

The transport along the magnetic field lines to the divertor targets can be characterized by parallel particle density and energy loss times τ_n and τ_E

$$\frac{\partial n_\mathrm{e}}{\partial t} \sim \frac{n_\mathrm{e}}{\tau_n}, \tag{11.59}$$

$$\frac{\partial}{\partial t}\left(\frac{3}{2} n_\mathrm{e} k T_\mathrm{e}\right) \sim \frac{\frac{3}{2} n_\mathrm{e} k T_\mathrm{e}}{\tau_E}. \tag{11.60}$$

The ESEL model calculates the parallel loss times for particles and energy from values of the density and temperature at the outer midplane and assumes a steady state. Parallel losses and transport are described as subsonic advection

$$\tau_n \approx \frac{L_\parallel}{M c_\mathrm{s}} \tag{11.61}$$

with the sound speed c_s and Mach number M ($M \approx 0.5$ derived from the two-point model) and the Spitzer-Härm diffusion

$$\tau_E \approx \frac{\frac{3}{2} L_\parallel^2 n_\mathrm{e}}{\kappa_\mathrm{e}^\mathrm{lim}} \tag{11.62}$$

with modified heat conductivity $\kappa_{\mathrm{e}}^{\mathrm{lim}}$ using heat flux limits to satisfy all SOL collisionality regimes. The length scale of parallel density and temperature variations $L_{\|}$ (in general distinct for the density and temperature) is assumed equal to the connection length L_{c}.

The fluid model was compared with the simple analytic model as a first approach to estimate a possible impact on the parallel damping for various collisionality regimes. Several scans were made over values of the cross-field sources S_{EXT}^{n} and S_{EXT}^{E} and steady-state solutions were used to calculate corresponding parallel loss times. Uniform cross-field sources were considered along the SOL and the equations

$$\frac{\partial}{\partial x}(n_{\mathrm{i}}u_{\mathrm{i}}) \approx \frac{n_{\mathrm{i}}}{\tau_n}, \tag{11.63}$$

$$\frac{\partial}{\partial x}\left(\frac{5}{2}u_{\mathrm{e}}n_{\mathrm{e}}kT_{\mathrm{e}} - \kappa_{\mathrm{e}}k\frac{\partial T_{\mathrm{e}}}{\partial x}\right) \approx \frac{\frac{3}{2}n_{\mathrm{e}}kT_{\mathrm{e}}}{\tau_E} \tag{11.64}$$

evaluated at the midplane (the upstream location in the model) were used as the definition for the parallel particle density and energy loss times, a more general form from which the equations (11.61) and (11.62) can be easily derived under the simple SOL picture. The condition of quasi-neutrality $n_{\mathrm{e}} = n_{\mathrm{i}}$ is assumed in the whole section. Note that the equations (11.63) and (11.64) do not take into account collision terms as their contribution to the parallel transport is negligible at the midplane.

One scan was selected to be discussed here. The results presented in Fig. 11.13 show the dependence of the parallel loss times on the electron collisionality

$$\nu_{\mathrm{e}}^{*} = \frac{L_c}{v_{\mathrm{e}}^{\mathrm{th}}\tau_{\mathrm{e}}}, \tag{11.65}$$

an important parameter characterizing the operational regime of a tokamak defined as the ratio of the connection length L_{c} and the electron self-collisionality length. We have obtained fair agreement for the parallel energy loss time τ_E in the investigated collisionality range and it seems that the analytic model based on the assumption of the heat diffusion is a good approximation in a steady state. The power to the targets is carried mostly by the conduction (compare the yellow and red points in Fig. 11.13), only at very weak collisionalities (green circle), the convection also plays a role. A remarkable difference appears in the comparison of the parallel density loss times τ_n in the whole collisionality range and the analytic model seems to be too rough estimate. We observe a departure from the analytic solutions especially at low densities and high temperatures, which could possibly explain why the model has not been successfully applied to a JET low-collision

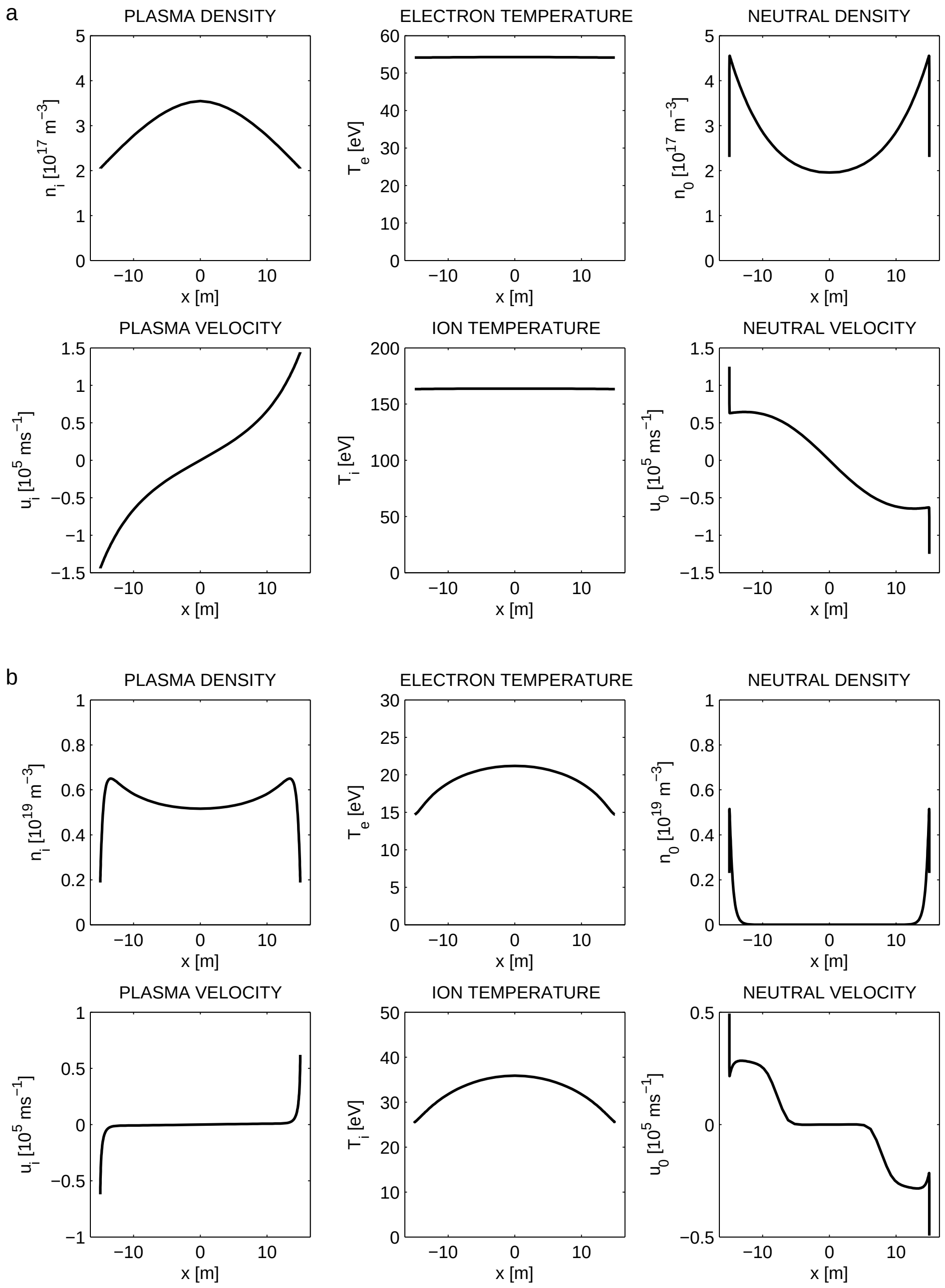

Figure 11.14: Profiles of the ion density n_i, the ion velocity u_i, the electron temperature T_e, the ion temperature T_i, the neutral density n_0 and the neutral velocity u_0 along the magnetic field line. A transition from the simple SOL (a) (the first run with the SOL in the sheath-limited regime) to the complex SOL (b) (the second run with the recycling at the targets).

Ohmic plasma [105]. The discrepancy is, however, remarkable even for a collisional SOL, that has been extensively studied with ESEL and reported e.g. in [106]. In Fig. 11.13, one run corresponding to very low collisionality coincides precisely with the analytic model (green circle). If we look at steady-state parallel profiles of the plasma parameters for this first run (Fig. 11.14 a) and the second run (Fig. 11.14 b), we can notice a transition from a recycling regime with typical higher plasma density at the targets and physics influenced by the ionization in the SOL to a simple SOL regime with characteristic flat profile of the temperature and parabolic profile of the density (see section 8.4). This simple SOL run is also in agreement with the two-point model (section 8.5.1) where the upstream plasma pressure is twice the value of the pressure at the target (Fig. 11.15), which corresponds to constant total pressure along the SOL. For higher collisionalities, we do not match the two-point model assumptions as the SOL plasma is in a high-recycling or detached state with a parallel source of momentum due to plasma-neutral collisions.

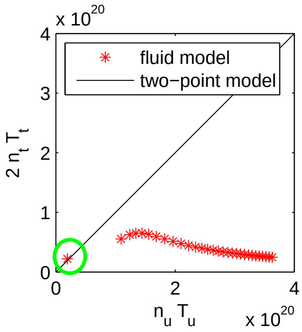

Figure 11.15: The pressure at the upstream location u and at the target t. A comparison with the two-point model.

ESEL has been applied to JET and TCV plasma discharges so far [105]. It has been found that for a low-collision L-mode plasma of a JET experiment, the parallel damping of the density is too weak to match experimental data and the parallel transport requires improvements. The simple analytic description of the steady-state parallel transport, at least for the particle losses, is not adequate as it was indicated by the comparison with the fluid approach. In the sheath-limited regime, we typically observe parabolic profiles of the density in the parallel direction. This assumption was used to derive the approximate expression for the parallel density loss time, however, in conduction-limited or detached regimes (e.g. the investigated regime of TCV that will be discussed in the following sections), strong gradients of the density and temperature develop at the boundaries, affecting the length scale of density variations. Consistently with the assumption $L_\parallel = L_\mathrm{c}$, uniform cross-field sources were considered in the fluid model. In real experiments, radial flows are predominantly concentrated around the outboard midplane (due to poloidal asymmetries) and the parallel profiles of the sources should be better described by a gaussian function localized at the midplane. This would influence also the parallel profiles of the plasma parameters, the length scales of parallel variations of the density and temperature and the strength of parallel losses. Specifically, using a simple approach, one might expect that τ_n is proportional to $L_\parallel / c_\mathrm{s}$ and τ_E scales as $\tau_E \sim L_\parallel^2 n_\mathrm{e} / \kappa_\mathrm{e}$. The fluid model could eventually provide a precalculated table of steady-state parallel loss times for ESEL in the collisionality range typically observed in tokamaks, however, we expect that the behaviour changes in a time-dependent case. In the following sections, the geometry and assumptions of the fluid model copy better realistic observations and the parallel transport is investigated under transient conditions of the turbulent radial transport.

11.6.2 Transient studies

Data from ESEL

To test the applicability of the one-dimensional fluid code to time-dependent problems and its stability for realistic fluctuations of the density and temperature, data from ESEL has been prepared from the most reported run 116, a simulation of interchange turbulence in the TCV tokamak [104]. Several assumptions were taken into account about the connection length ($L_\mathrm{c} = 15$ m) and profiles of the sources S^n_EXT and S^E_EXT according to typical conditions found in discharges of the TCV device. The parallel profiles of the cross-field sources are not uniform as in the previous section, but gaussian profiles are prescribed, which is more realistic and appropriate assumption because of poloidal asymmetries observed in tokamaks. Experiments show that radial flows of particles and energy are observed around the midplane with the poloidal angle approximately ±30° [107].

Results of ESEL provide realistic fluctuations of the density and temperature and corresponding cross-field sources S^n_EXT and S^E_EXT in time at each point of the ESEL domain. The following input data has been obtained for the parallel transport code (Fig. 11.16), calculated from the ESEL output at the selected radial position $\rho = 0.20$ (ρ is the normalized radial coordinate, see Fig. 11.12). The average plasma density and electron temperature at this position are $\langle n_\mathrm{i} \rangle = 1.5 \times 10^{19}$ m^{-3} and $\langle T_\mathrm{e} \rangle = 12.8$ eV. The cross-field

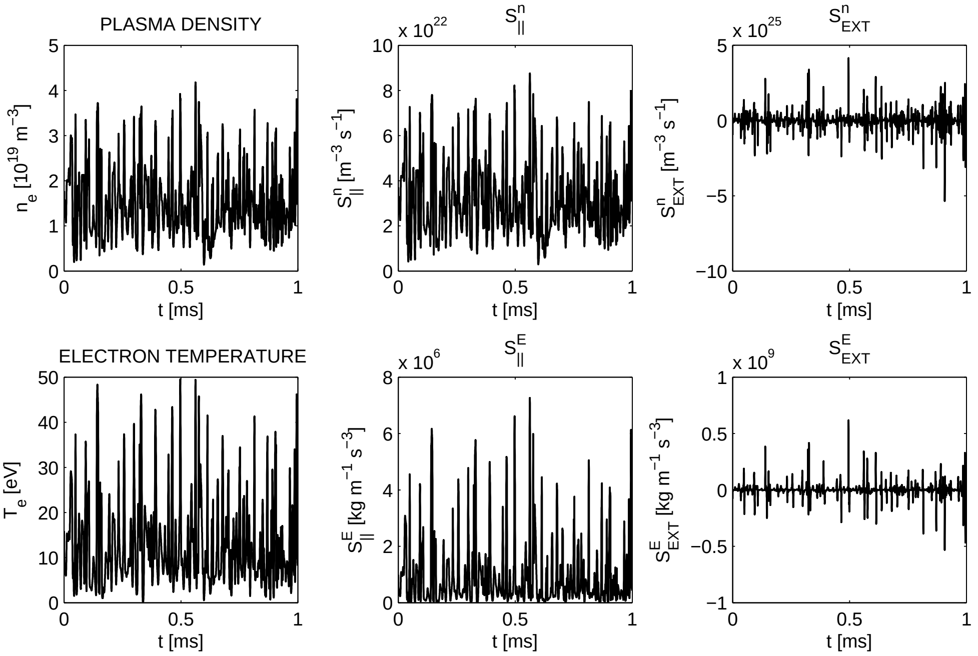

Figure 11.16: Time series from the ESEL run 116 used as input for the parallel transport code – the plasma density n_{e}, the electron temperature T_{e}, the total parallel particle and energy losses $S^n_{\|}$ and $S^E_{\|}$ and corresponding cross-field terms S^n_{EXT} and S^E_{EXT}.

sources S^n_{EXT} and S^E_{EXT} were evaluated from the equations

$$\frac{\partial n_{\mathrm{e}}}{\partial t} + S^n_{\mathrm{EXT}} + S^n_{\|} = 0, \tag{11.66}$$

$$\frac{\partial}{\partial t}\left(\frac{3}{2} n_{\mathrm{e}} k T_{\mathrm{e}}\right) + S^E_{\mathrm{EXT}} + S^E_{\|} = 0 \tag{11.67}$$

and the parallel damping terms were calculated from ESEL parallel loss times as

$$S^n_{\|} = \frac{n_{\mathrm{e}}}{\tau_n}, \tag{11.68}$$

$$S^E_{\|} = \frac{3}{2} n_{\mathrm{e}} k T_{\mathrm{e}} \left(\frac{1}{\tau_n} + \frac{1}{\tau_T}\right), \tag{11.69}$$

$$S^T_{\|} = \frac{T_{\mathrm{e}}}{\tau_T}. \tag{11.70}$$

Note that ESEL works with the temperature equation and the parallel electron cooling time τ_T, while the fluid code requires cross-field sources in terms of the density and energy. The obtained values S^n_{EXT} and S^E_{EXT} are radial sources at the outer midplane, the interface of the two codes, which is modelled as the central upstream location in the parallel direction. Gaussian profiles of the sources are assumed along the magnetic field (Fig. 11.17) with the gaussian width in conformity with observations. The same power input S^E_{EXT} is considered for electrons and ions.

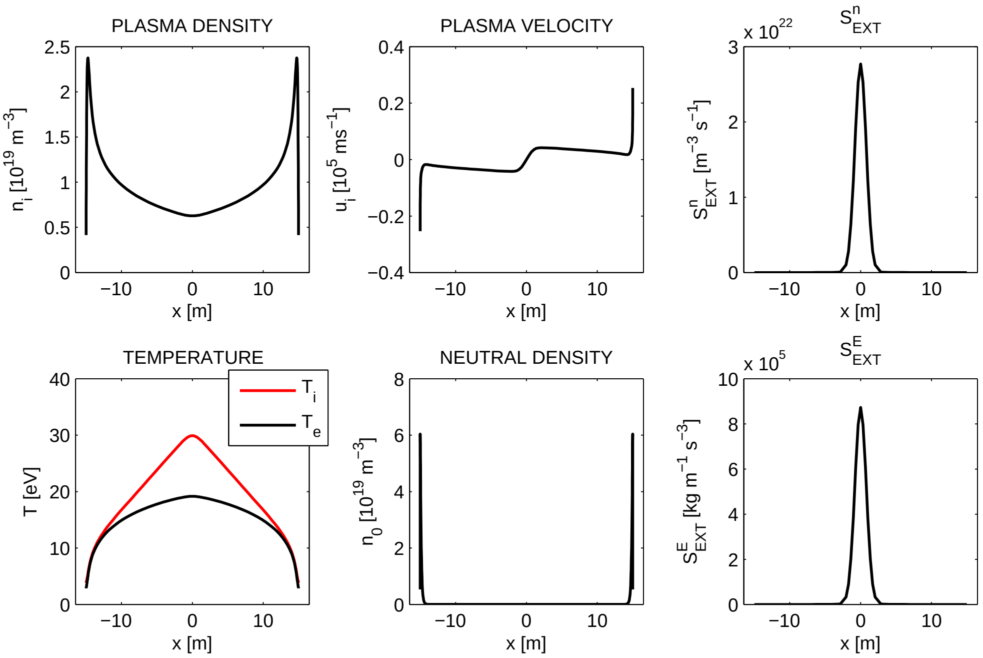

Figure 11.17: Profiles of the ion density n_{i}, the ion velocity u_{i}, the electron and ion temperature T_{e} and T_{i}, the neutral density n_0 and the sources of the mass and energy S^n_{EXT} and S^E_{EXT} along the magnetic field line. A steady-state solution.

Sources averaged over the whole investigated time interval were used for obtaining a steady-state solution (Fig. 11.17) and the profiles of the plasma parameters in the steady state were used as the initial condition that is required at the beginning of the calculation. The steady-state profiles were found in a range of realistic values. The upstream density ($n_{\mathrm{i}} = 6.8 \times 10^{18}\ \mathrm{m}^{-3}$) is lower than the average density calculated by ESEL and the electron temperature ($T_{\mathrm{e}} = 19.2$ eV) is higher. The ion temperature in the centre is approximately 1.5 times higher than the temperature of electrons for the same amount of energy S^E_{EXT} going to the electron and ion component. Note that an assumption about the distribution of the sources along the SOL is needed and their parallel profile is an optional parameter. The density and also the temperature would be higher if we extended the gaussian width.

It should be also remarked that the average value of the sources used to obtain the steady-state solution is almost exclusively determined by parallel damping terms approximated by simple analytic formulas. In the run 116, even a cruder model of parallel losses was used assuming constant parallel loss times τ_n and τ_T across the SOL with values related to the density and temperature at the separatrix. Fig. 11.18 shows individual contributions of all calculated terms to the total parallel losses $S_{\|}^n$ and $S_{\|}^T$. In a steady state, these should balance exactly the corresponding cross-field terms S_{EXT}^n and S_{EXT}^T. We can see that collision terms are negligible at the midplane, particles are convected, while the conduction dominates in the heat transport.

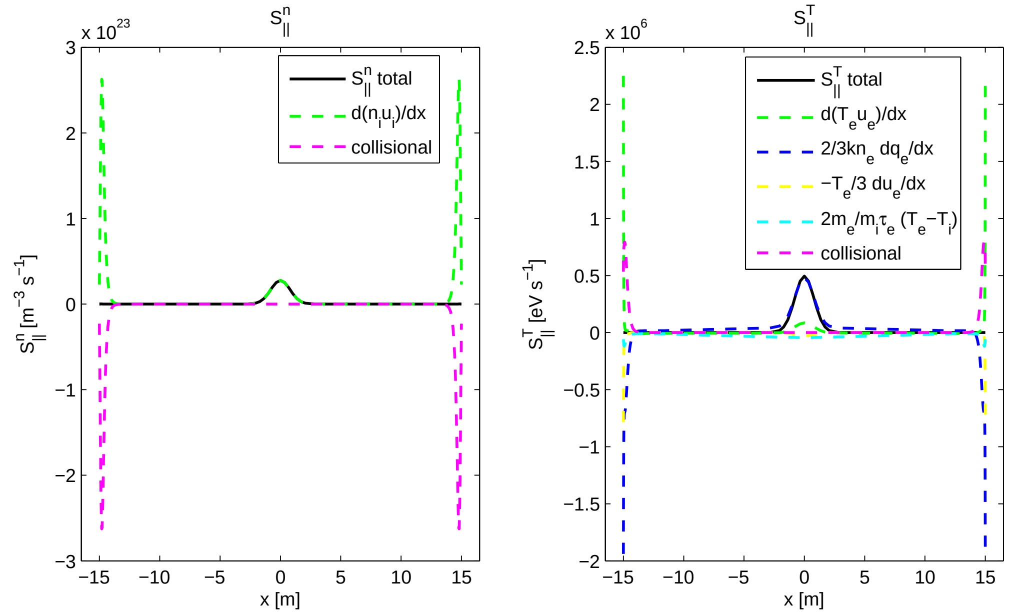

Figure 11.18: The total parallel particle and temperature losses $S_{\|}^n$ and $S_{\|}^T$ and contributions of all individual terms in a steady state.

After reaching the steady state, the precalculated time-dependent sources simulating turbulent plasma flows (Fig. 11.16) were applied giving rise to fluctuations of the plasma parameters along the SOL. Passing intermittent blob structures represent input sources of particles and energy into the flux tube and we observe their damping as the particles and power are transported to the targets. The intensity of upstream density variations was found in fair agreement with ESEL data (Fig. 11.19), however, there is one visible difference. If the cross-field flux S_{EXT}^n decreases significantly, the density falls down as well, consequently rising the temperature. Drops of the density are stronger than in ESEL (which is consistent with observed stronger parallel losses in the fluid code) and during the strongest negative peaks, the density tends to go below zero and the temperature increases to unphysical levels (Fig. 11.20). To avoid negative values, certain limits had to be imposed on the density and temperature. Note that we do not aim and expect agreement with ESEL data, but we would like to estimate differences in the parallel transport in both approaches. It is important to realize that the average values of the density and temperature in the transient state differ from the initial steady-state values, while the average values of the sources S^n_{EXT} and S^E_{EXT} were used to reach the steady state.

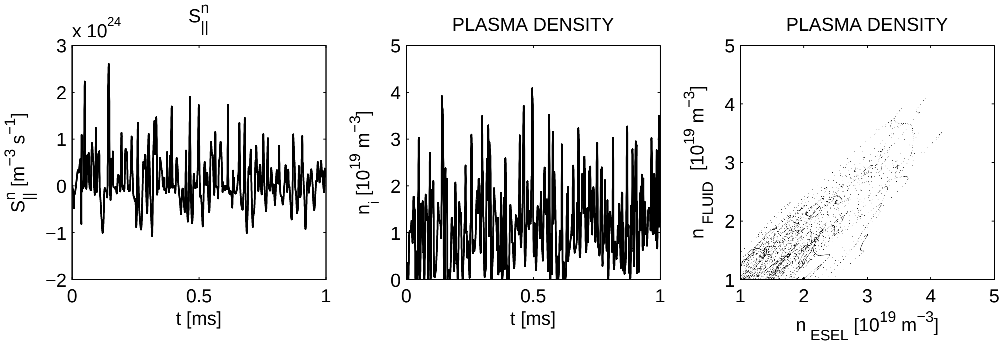

Figure 11.19: The total parallel density losses $S^n_{\parallel}$ and the plasma density n_{i} at the midplane calculated in the fluid code and a comparison of the density with ESEL values.

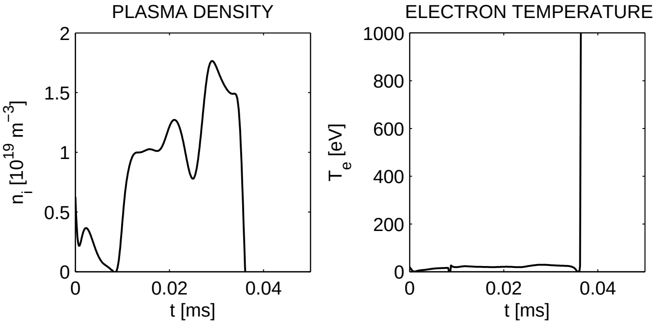

Figure 11.20: Fluctuations of the plasma density n_{i} and electron temperature T_{e} at the midplane.

The resulting parallel damping terms (Fig. 11.19) are stronger, i.e. the parallel loss times are shorter compared to the model which has been implemented in ESEL (Fig. 11.16) and the plasma density reaches lower values as a consequence of stronger particle losses. The problematic drops of the density and temperature below zero are caused by the inconsistency of the parallel transport and they are, hopefully, not expected to be observed in the coupled system of the two codes.

Step function

One transient event based on data selected from the ESEL series (Fig. 11.21) has been studied. For the sake of simplicity, the inflow of particles and energy to the flux tube from a passing blob is simulated as a step function in time with the duration and intensity corresponding to realistic conditions provided by the ESEL output. The initial condition is again a steady state calculated as in the previous case (Fig. 11.17).

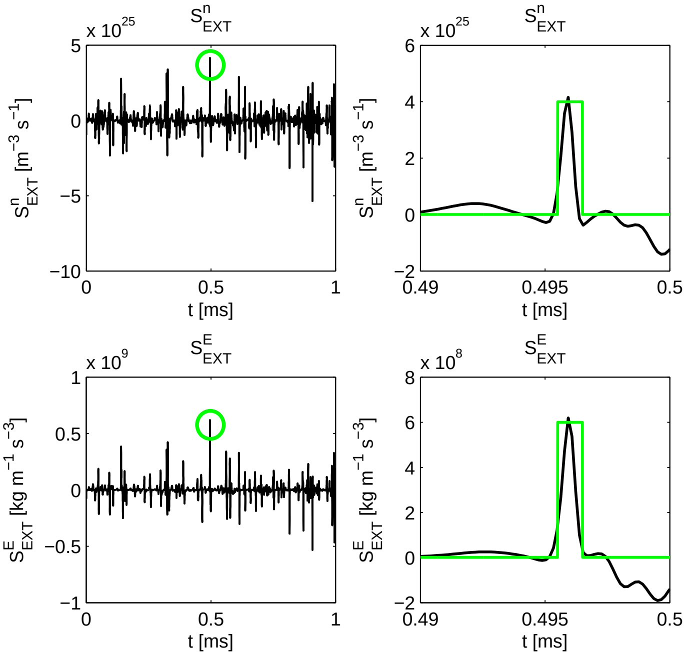

Figure 11.21: One peak in time series from ESEL (green circle) has been replaced by a step-function and analyzed.

The transient burst appears at 0.03 ms with the duration 1 μs. The upstream density and temperature at the midplane immediately jump up as the sources are highly localized at the midplane and a response at the targets is observed later (Fig. 11.22). A detailed view in Fig. 11.23 shows parallel density and energy losses and contributions of the conduction and convection to the power transport.

In Fig. 11.24, we can see parallel profiles of the plasma density, velocity and electron temperature at three selected moments: 0.025 ms (the steady

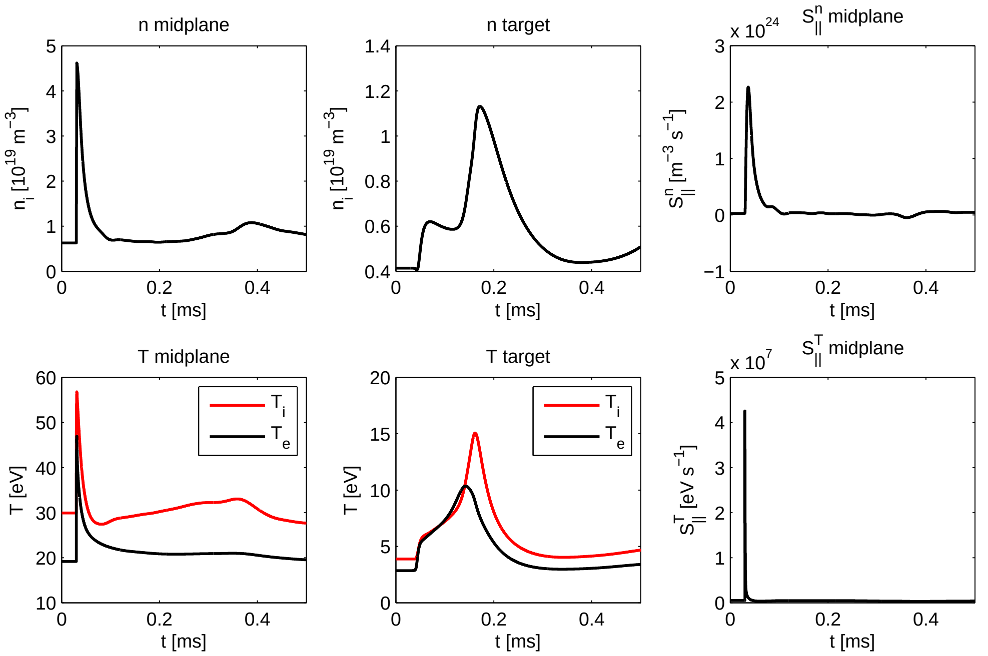

Figure 11.22: Temporal profiles of the plasma density n_i and temperature T_e and T_i at the midplane and target and corresponding parallel density and temperature losses $S_{||}^{n}$ and $S_{||}^{T}$.

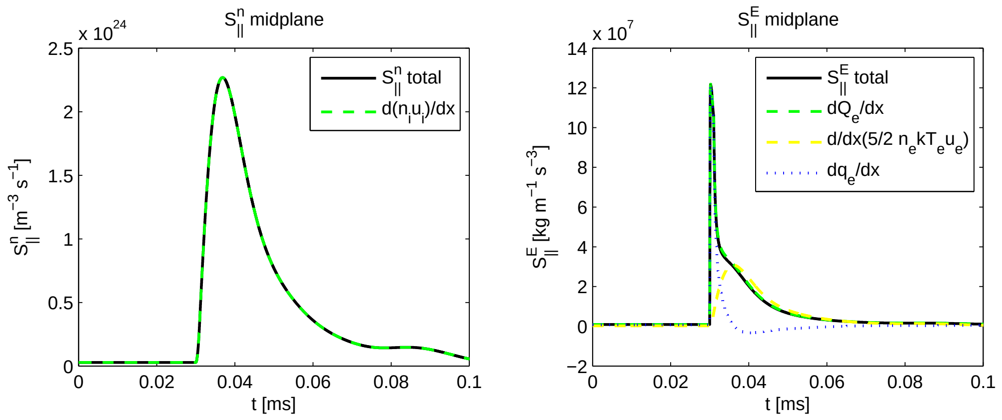

Figure 11.23: The total parallel density and energy losses $S_{||}^{n}$ and $S_{||}^{E}$ and the conduction and convection contribution to the energy transport.

state), 0.031 ms (the maximum density and temperature) and 0.075 ms. The radial influx of particles and energy around the midplane raises rapidly the density and temperature in the centre. We observe that the temperature tends to flatten out faster than the density (see the red curve) as the power is quickly transported to the targets by the heat diffusion. The first observable increase of the density at the target (see Fig. 11.22) which appears before the incoming particles reach the boundary (the main peak) is a consequence of the compression under the pressure gradient due to changes of the temperature or the ionization which becomes stronger at higher temperatures. The particles and energy propagate to the targets (see the green curve and the two density peaks) and we can notice that the plasma velocity increases compared to the steady-state value. A slow relaxation back to the steady-state solution follows.

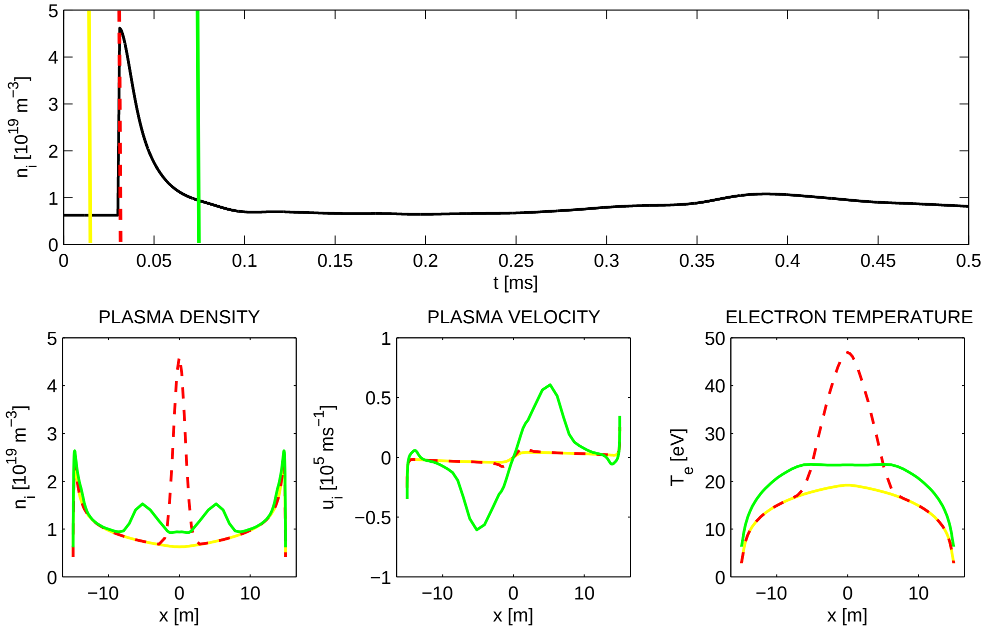

Figure 11.24: Parallel profiles of the plasma density n_i, the plasma velocity u_i and the electron temperature T_e at three selected moments.

We are in particular interested in temporal scales of this process which characterize the dynamics of the parallel transport. The temporal scale of the propagation of the particles and power along the SOL can be characterized by time intervals between the moments when we observe the maximum values at the midplane and at the target. The time when the particles reach the targets with respect to the moment when the plasma blob appears at the midplane (modelled as a sudden increase of cross-field sources fueling the flux tube with particles and energy) is $\Delta t_n = 0.14$ ms and for the temperature $\Delta t_T = 0.11$ ms. The value normalized by the characteristic parallel loss time defined as $\tau_{n_0} = L_\mathrm{c}/c_\mathrm{s}$ and evaluated at the midplane in the steady state is $\Delta t_n/\tau_{n_0} = 0.64$. According to this estimate, it might seem that the blob is propagating with a velocity higher than the ion sound speed. However, in Fig. 11.25, where the sound speed is calculated in the actual blob location, we observe a subsonic transport and a slowing down close to the target due to the plasma-neutral friction.

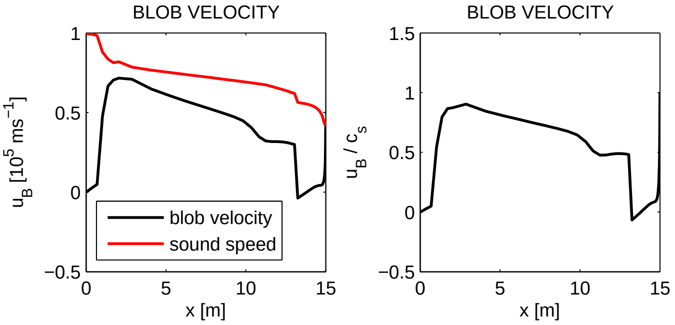

Figure 11.25: The parallel velocity of the blob u_{B} and the normalized value $u_{\mathrm{B}}/c_{\mathrm{s}}$ at each passed parallel position x calculated as the plasma velocity u_{i} at t_{max} when the density at x reaches the maximum. The sound speed c_{s} is calculated at the position x at t_{max}.

The strength of the parallel losses of particles and energy can be described by parallel loss times defined by the equations (11.68) and (11.70). The parallel particle density loss time τ_n and the electron cooling time τ_T are plotted in Fig. 11.26 as functions of time and their values are compared with the analytic model defined by the equations (11.61) and (11.62) and the constant values which were used in the ESEL run 116.

Further, Fig. 11.26 shows the total parallel density and temperature losses $S_{\|}^{n}$ and $S_{\|}^{T}$ as functions of the density and temperature and we can see that the assumption of constant parallel loss times in ESEL (meaning that $S_{\|}^{n}$ scales linearly with the density and $S_{\|}^{T}$ is proportional to the temperature) is a crude approximation. Note that $S_{\|}^{n}$ in Fig. 11.26 goes anti-clockwise in time, while $S_{\|}^{T}$ goes clockwise, which can be deduced from Fig. 11.27. $S_{\|}^{T}$ reaches the maximum before the maximum temperature as the heat is instantly being transported to the target by the diffusion. From Fig. 11.27 and also the illustrations above (Fig. 11.24, 11.23 and 11.18), an important statement follows. Due to the fact that the energy is relatively fast conducted to the targets, the assumption $L_{\|} = L_{\mathrm{c}}$ in the analytic model is more relevant for the temperature than for the convective particle transport. This observation may explain why good agreement between the simulation and experiment for the JET plasma in [105] has been achieved for the temperature radial profiles, while the length scale of density variations should be shorter to observe a match with experiment also for the density.

The right part of Fig. 11.26 shows the strength of density and temperature fluctuations in terms of times defined as

$$\tau_n^{\mathrm{dyn}} = \frac{n}{\frac{\partial n}{\partial t}}, \tag{11.71}$$

$$\tau_T^{\mathrm{dyn}} = \frac{T_\mathrm{e}}{\frac{\partial T_\mathrm{e}}{\partial t}} \tag{11.72}$$

and we would expect a relation between τ_n and τ_n^{dyn} or τ_T and τ_T^{dyn}.

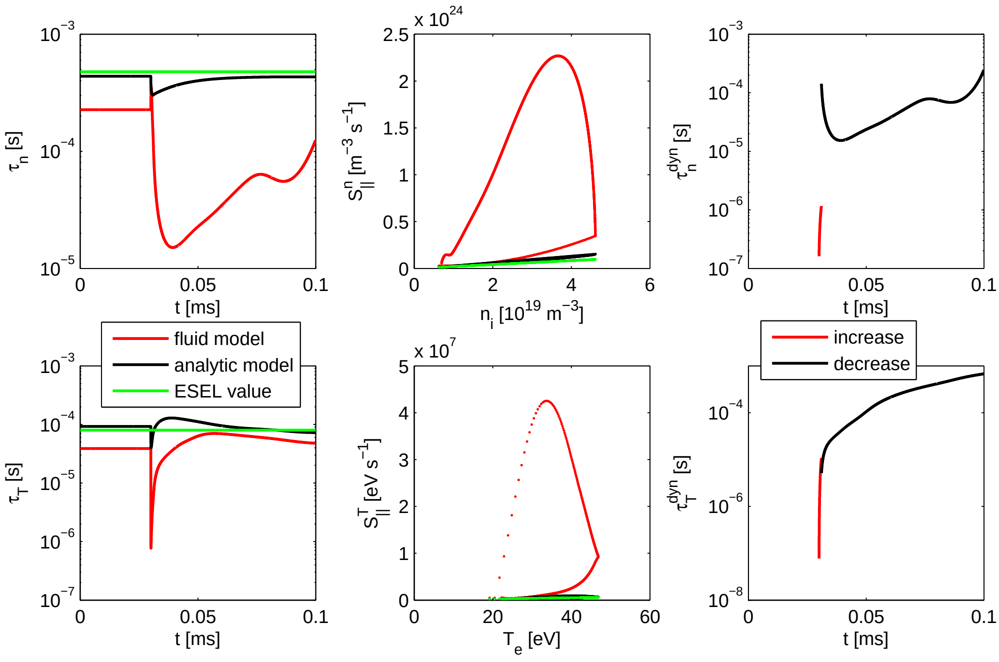

Figure 11.26: The parallel particle density loss time τ_n, the electron cooling time τ_T, the total parallel losses $S_{\|}^n$ and $S_{\|}^T$ as functions of the density n_i and temperature T_e and temporal scales of the density and temperature perturbations τ_n^{dyn} and τ_T^{dyn}.

The parallel transport has been analyzed for a simple case when cross-field sources of particles and energy were represented by a step-function. A real blob would be realized as a rapid increase of the sources followed by a sink of particles and energy as the blob passes across the flux tube. Anyway, the analysis given here provides a useful insight into the parallel dynamics. In spite of the complexity, we can conclude that the analytic model underestimates the parallel losses in the analyzed transient case. We have now introduced two additional parameters having effect on the strength of parallel damping compared to the steady-state analysis in section 11.6.1. These

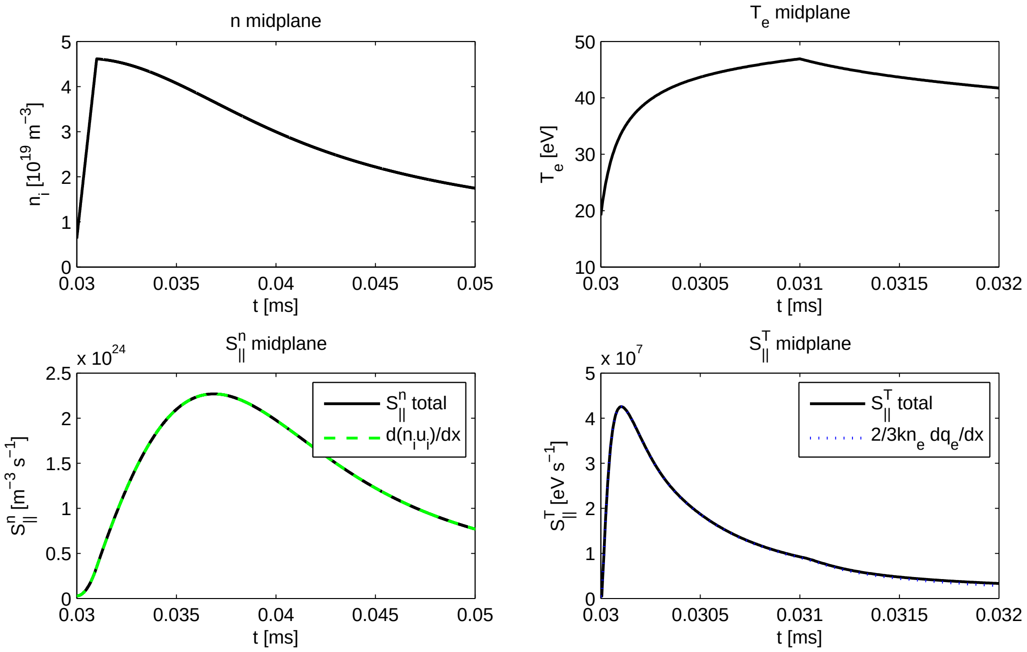

Figure 11.27: A detailed view to temporal evolution of the plasma density n_i, the electron temperature T_e and the total parallel losses $S_\parallel^n$ and $S_\parallel^T$ shortly after the burst appears.

parameters are the spatial distribution of the cross-field sources S_EXT^n and S_EXT^E (the gaussian width) and the strength of temporal density and temperature variations expressed by τ_n^dyn and τ_T^dyn. We observe that the discrepancy between values calculated by the fluid model and loss times estimated by the analytic expressions under simplifying assumptions grows after the sudden burst appears with respect to the steady-state values. In context of the analysis presented here, the large turbulent transport seems to be a dominant source of plasma in the flux tube and the plasma is fueled by passing intermittent structures around the midplane. Processes at the targets (the recycling and the ionization as a source for plasma) become less relevant than in the steady-state analysis. Therefore the form of the cross-field sources is important and the spatial scales of parallel density and temperature variations and the parallel damping are dependent on their distribution in the parallel direction and the intensity of their fluctuations (causing perturbations of the density and temperature). In general, the parallel damping is stronger for a source localized in a narrow region close to the midplane, while for a source that extends to the targets, we observe slower parallel losses. It is difficult, however, to estimate how the parallel profiles of the sources change radially across the SOL and we would expect their broadening with increasing radial coordinate as the plasma tends to form filaments that extend along the SOL.

11.6.3 Final coupling

It was stated in [105] that a mismatch of the radial density profile in a JET Ohmic plasma calculated by ESEL with the measured one has been observed and an advanced approach for the description of the parallel transport based on coupling ESEL with a parallel transport fluid model would be appreciated. The presented work indicates that such approach could increase the steepness of the radial density profile. One can easily deduce, how radial profiles of the density and temperature would be affected by stronger parallel damping. Shorter parallel loss times result in shorter e-folding lengths (the radial decay length), thus reducing broadening of the radial profiles.

It is believed that parallel transport investigations can provide useful information about the parallel dynamics and losses to the targets in transient conditions and that an improvement of the parallel transport model in ESEL and especially the time-dependent coupling of the two codes can reduce the discrepancy between ESEL simulation results and experiment.

The joint model will be a quasi three-dimensional simulation. In each nodal point of the ESEL grid (see Fig. 11.12), we need to calculate total parallel losses of particles and energy, i.e. the parallel transport code will be applied on a number of flux tubes which are coupled together by the cross-field transport calculated within ESEL.

Such simulation is going to be computationally intensive. Both codes use comparable time steps $\Delta t \approx 1 \times 10^{-8}$ s and typical temporal scale of intermittent structures is roughly 1×10^{-5} s. If the real time of one iteration of the parallel transport code is 0.6 ms (see section 11.4.3), then for 1×10^{5} grid points, we get 60 s in total per one ESEL iteration, while ESEL itself is only 0.1 s. The ESEL simulation is typically run for 1-2 million time units and we need at least few hundred thousands iterations ($\sim$ 10 blob realizations) to obtain reasonable statistics and valuable results. Even if the parallel transport is proposed not to be updated in every iteration of ESEL (at least as a first approximation) or to be calculated on a coarser grid, the code parallelization and distribution of computational power among CPUs is necessary anyway.

The most straightforward way to couple both codes is to exchange information about total cross-field sources (the input for the parallel transport code) and total parallel losses (required by ESEL). One could object that we can not guarantee to have the same densities and temperatures in both codes and the total parallel losses calculated by the parallel transport code could be related to different values of the density and temperature than ESEL uses. Therefore, the parallel transport model has been modified and the new version uses the density and electron temperature at the midplane as input parameters instead of the cross-field sources. In this approach, however, corresponding radial sources must be calculated in each time step and their adjustment requires a couple of additional iterations. Therefore the exact implementation of the quasi three-dimensional model is still subject of discussions.

CHAPTER 12

Introduction to two-dimensional edge modelling

12.1 Plasma edge and numerical tools

The edge region plays an important role in questions of the confinement of plasma in tokamaks and substantial part of the fusion research is focused on the study of phenomena in the scrape-off layer such as turbulent structures, instabilities, detached regimes or plasma-solid interactions. Experimental investigations and diagnostics are supported by the computational approach. The edge physics is very complex and involve a variety of processes and phenomena. The modelling effort concerns a study of individual processes or individual regions (see chapter 9) or simulates the entire SOL and global transport.

The following summary focuses on two-dimensional multifluid codes for a steady-state analysis of the SOL and chapter 12 provides an overview of numerical tools such as B2, EDGE2D etc, which were previously mentioned in section 9.0.4. The models gather aspects of the numerical mathematics and physics with contributions from many areas combining the fluid theory, the kinetic theory, the atomic and molecular physics, the theory of plasma-solid interaction (Fig. 12.1). Charged main plasma species as well as charged impurities are described within the fluid approach. The models treat all ionic species in different charge states as separate fluids. Interactions of the charged species with a neutral background are also taken into account using various techniques of the inclusion of collisions (see section 12.4). The codes should be equivalent in physics that is involved and they describe the edge plasma transport on a computational domain restricted to two dimensions in poloidal cross-section. They have been applied on different machines in the past and now there is an effort to utilize these tools.

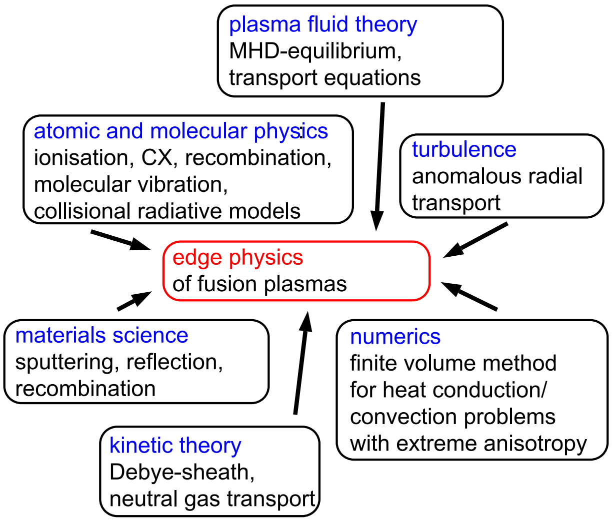

Figure 12.1: The complexity of the tokamak edge physics. Research areas related to the multifluid edge modelling. Reprinted from [66].

12.2 Grid and geometry

The two-dimensional transport models assume a perfect toroidal symmetry and work on a computational domain in the poloidal cross-section. The fluid motion of the plasma along the magnetic field is projected to the poloidal plane and described using the toroidal coordinates φ (toroidal), θ (poloidal) and r (radial). The computational coordinate system x, y and z coincides with the magnetic coordinates (an example in Fig. 12.2) to which a system of equations governing the transport of plasma species is transformed. This is done using the metric coefficients $\mathrm{d}x = h_\theta \mathrm{d}\theta$, $\mathrm{d}y = h_r \mathrm{d}r$, $\mathrm{d}z = 2\pi R_\mathrm{t}$. In case of a limiter machine, the grid is simpler since circular magnetic flux surfaces are commonly assumed and thus the radial and poloidal coordinates r and θ match the magnetic coordinate system. In addition, there is no X point that would complicate the numerical implementation.

The orthogonal grid (an example in Fig. 12.3) is a result of a process known as the magnetic reconstruction. The equilibrium reconstruction is performed by a special software (e.g. EFIT [109]) as a preprocessing procedure. The magnetic configuration is scanned on the basis of data from detectors and their positions and the Grad-Shafranov equation [63] is solved to obtain a map of magnetic flux surfaces. The equilibrium solver is followed by orthogonalization techniques [110, 111] to construct the full grid.

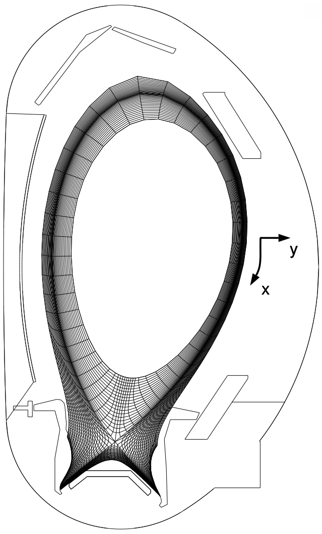

Figure 12.2: The magnetic topology and coordinates – x varies along flux surfaces, y varies perpendicular to the flux surfaces and z is the toroidal direction. Reprinted from [108].

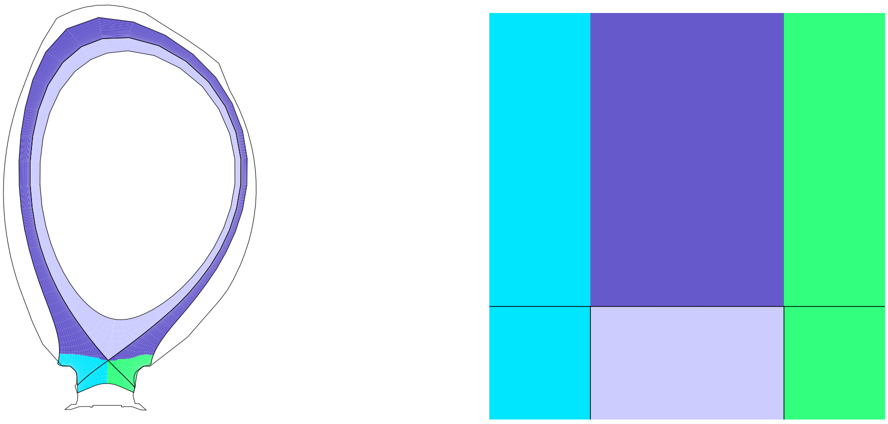

Figure 12.3: The physical (left) and computational (right) plane. Reprinted from [108].

12.3 Fluid model and mathematical description

Charged species are treated as a fluid. The mathematical description of the transport parallel to the magnetic field is based on fluid equations commonly following the set introduced by Braginskii [68] and the transport is supposed to be classical or neoclassical. The continuity and momentum equations are solved for ions, the plasma is quasineutral and the ambipolar flow is assumed along the magnetic field. The heat transport is governed by the energy balance with separate equations for the ions and electrons, similarly as in section 11.2.1. The equations are projected to the poloidal plane and written in the curvilinear coordinate system. Impurity ions are treated as a separate fluid, while usually only one ion temperature is assumed for all ionic species.

In regions where steep gradients are present (e.g. the private region below the X point) and the condition for justification of the fluid description $\lambda \ll L$ (see section 8.5) imposed on the mean free path of collisions λ and the characteristic length scale of variations of the plasma parameters L is not fulfilled, the fluid approximation loses the validity and kinetic corrections should be introduced. The parallel heat transport is flux limited [112, 113] using a flux-limiting factor for the parallel thermal conductivity (see section 11.2.3). Formally, the parallel thermal heat flux is modified as

$$\frac{1}{q_{\|}} = \frac{1}{q_{\mathrm{lim}}} + \frac{1}{q_{\mathrm{CL}}} \tag{12.1}$$

where q_{CL} is the original classical value and

$$q_{\mathrm{lim}} = \alpha n v^{\mathrm{th}} kT. \tag{12.2}$$

A proper value of the flux limiters is an issue that has to be investigated by the kinetic approach.

The transport perpendicular to the magnetic field is large compared to classical or neoclassical predictions. The mechanism of this anomalous transport might be explained on the basis of turbulent plasma behaviour, however, in the considered and mentioned fluid models, it is represented in the form

$$\Gamma_{\perp} = n u_{\perp} = n v_{\mathrm{adv}} - D_{\perp} \frac{\partial n}{\partial r} \tag{12.3}$$

where v_{adv} is an advective velocity and $D_{\perp}$ is a diffusion coefficient. The transport processes that can not be accurately modelled in the fluid approximation are described by anomalous diffusion with an empirical coefficient $D_{\perp}$.

12.4 Model of neutrals

Neutral atoms are treated separately from the fluid plasma model. Various techniques can be used. Monte Carlo models such as EIRENE [114] or

NIMBUS [115] are three-dimensional simulations of a linear transport of test particles (neutrals) in a background medium (plasma). The packages are coupled to databases for atomic and molecular data.

An alternative approach is the fluid description, specifically the neutral diffusion approximation [102]. The neutral-plasma volumetric sources are written in a simple manner for two reactions – the electron impact ionization and the charge exchange. The continuity equation for the neutral density n_0

$$\frac{\partial n_0}{\partial t} + \nabla \cdot \Gamma_0 = -S_0^n \tag{12.4}$$

is solved with the ionization as the source S_0^n. The second moment of the neutral transport equation gives an expression for the neutral flux in the form of the diffusion approximation

$$\Gamma_0 = -D_0 \nabla n_0 \tag{12.5}$$

with the neutral diffusion coefficient D_0 [116, 117]. The approximation assumes that neutrals are in one energy group and locally at the same energy as the average ion temperature. Processes on the solid surface (the recycling and sputtering) appear in the model in boundary conditions.

An analytic approximation is another possibility. The spatial distribution of neutrals is described by a simple analytic expression, again with the plasma-solid processes given at the boundaries. This model is used e.g. in [75, 118].

The analytic approach is simple to implement and quick to solve, but it is not generally intended for the time-dependent resolution of physics. The Monte Carlo technique is the most precise treatment, however, the codes are very costly in computer time. The implementation is more complicated, it is difficult to couple a finite differenced plasma solution to a statistical neutral solution on the same computational grid and to assure convergence [117].

12.5 Boundary conditions

To close the fluid description of the plasma transport, boundary conditions are required at the interface of the plasma with the targets, the wall and the central plasma, evaluating the plasma density, velocity and temperature at boundaries of the computational region. At the core boundary, the total power and particle input fluxes Q^E and Q^n are specified to fix the density and temperature or the density is fixed by a Dirichlet boundary condition [66, 119]. At the wall, decay lengths λ_n and λ_T (the characteristic decay lengths of the density and temperature in the radial direction) are used as a standard choice (see [66, 119])

$$\frac{1}{n_\mathrm{i}}\frac{\partial n_\mathrm{i}}{\partial y} = \frac{1}{\lambda_n}, \tag{12.6}$$

$$\frac{1}{T_\mathrm{e,i}}\frac{\partial T_\mathrm{e,i}}{\partial y} = \frac{1}{\lambda_T}, \tag{12.7}$$

$$\frac{\partial u_\mathrm{i}}{\partial y} = 0. \tag{12.8}$$

The plasma-solid interface at the targets incorporates the sheath boundary conditions (see section 8.2) for the total heat flux

$$Q_{\mathrm{e}\|} = \delta_\mathrm{e} k T_\mathrm{e} n_\mathrm{e} c_\mathrm{s}, \tag{12.9}$$

$$Q_{\mathrm{i}\|} = \delta_\mathrm{i} k T_\mathrm{i} n_\mathrm{i} c_\mathrm{s} \tag{12.10}$$

using the heat transmission coefficients δ_e and δ_i. The parallel flow velocity is assumed to be equal to the local sound speed (the Bohm-Chodura condition)

$$u_{\mathrm{i}\|} = c_\mathrm{s}. \tag{12.11}$$

12.6 Drifts and currents

An impact of electric fields and drifts is important for the transport of plasma and impurities between the divertor legs and effects associated with drifts and currents should be included in the transport codes. The poloidal and radial drift flows and electric currents, which are produced by the electric and diamagnetic drifts, play a crucial role for the plasma redistribution and cause asymmetries in the plasma parameters between the inner and outer divertor regions with respect to the direction of the magnetic field. Basic results can be understood by dividing the drifts into three categories – diamagnetic, $\mathbf{E} \times \mathbf{B}$ and $\nabla\mathbf{B}$.

The dominant effect near the divertor plates comes from the $\mathbf{E} \times \mathbf{B}$ drifts. The poloidal $\mathbf{E} \times \mathbf{B}$ drifts are driven by the radial electric field that arises as a result of radial temperature gradients, while the radial $\mathbf{E} \times \mathbf{B}$ drifts are driven by the poloidal electric field occurring as a consequence of parallel temperature gradients, usually strongest in the vicinity of the X point [62, 65]. Since the $\mathbf{E} \times \mathbf{B}$ drift is the same for the electrons and ions, it generates no current. A self-consistent calculation of the electric field in the two-dimensional edge codes is complicated, the inclusion and implementation is reported e.g. in [120–123].

The presence of pressure gradients results in diamagnetic drift motions. The diamagnetic fluxes are almost divergence free with no effect on plasma boundary conditions. The drift velocity is charge dependent, the diamagnetic drifts produce currents that form closed circuits inside the plasma and do not reach the target surface. The divergence free components do not contribute to the transport [124].

The toroidal magnetic field scales as the inverse major radius $B_{\mathrm{t}} \sim 1/R_{\mathrm{t}}$ giving rise to a $\nabla\mathbf{B}$ drift motion. In the poloidal plane, the velocity due to the $\nabla\mathbf{B}$ drift is downward for the normal field direction. The $\nabla\mathbf{B}$ drift is weaker than the $\mathbf{E} \times \mathbf{B}$ drift and causes an increase in the magnitude of the radial electric field inside the separatrix. Its influence on transport simulations is documented e.g. in [121].

The inclusion of the drift fluxes into the transport codes has been of much recent interest. During the past decades, the drift effects were taken into account and implemented in the codes, nevertheless, results obtained with the drifts and a detailed description of their influence on the profiles or on plasma conditions near the targets are still scarce. Despite their importance, the drift effects are difficult to implement in most of the simulation codes, they strongly effect on the code structure, complicate the boundary conditions and in general cause serious numerical difficulties. To avoid numerical problems, a special treatment is required. Several ways of the implementation and the numerical treatment are described in [75, 123, 125] in more detail.

12.7 Numerics and overview

The edge codes use various approaches for the numerical discretization of the fluid equations. The finite volume method is used in B2 [66] or in [117], while EDGE2D [74, 126] and TECXY [127] use the finite difference technique and the finite element method has been also applied [120, 128, 129]. The main advantage of the finite element modelling is the discretization on an unstructured triangular mesh (an example in Fig. 12.4) instead of conventionally structured quadrilateral mesh which is used for example in B2 or EDGE2D. The finite element method benefits from the geometric adaptability of the unstructured mesh representing the geometry and boundaries in a realistic way and allowing a local refinement in regions where it is needed (i.e. in the vicinity of the X point where strong gradients may occur). In case of the structured grid, increasing the resolution at the X point implies smaller cells also in regions where a finer resolution may not be needed. On the other hand, the methods using the structured grid are well established and the grid is relatively simple and naturally able to represent strong transport anisotropies in a magnetized plasma, while the latter makes certain constrains for the finite element modelling [128]. A tutorial to the technique of the FDM, FVM and FEM is given e.g. in [22].

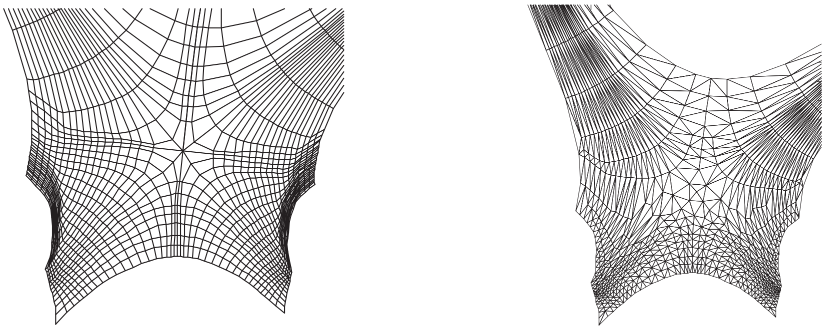

Figure 12.4: A structured quadrilateral grid (left) used in the finite difference or finite volume methods and an unstructured triangular grid (right) used in the finite element method. Reprinted from [128].

The two-dimensional edge transport models are robust packages. The modelling activity has been started in 80's and it continues with further developments, benchmarks and integration. The computer modelling of the edge plasma is an important part of the fusion research, it is used to interpret measurements or to guide the design of machines, while accounting for a comprehensive set of physical effects. Computational investigations study the drift effects [75, 121, 125], the impurity transport and influence, the processes at a solid surface, the detachment [65] or the instabilities such as MARFEs [119].

The fluid codes are either coupled with a Monte Carlo model for the transport of neutrals (NIMBUS, EIRENE) or they treat neutrals in a simpler manner using the analytical model [118] or the neutral diffusion approximation [102, 120]. Some of the fluid and Monte Carlo codes were originally developed to function as a pair – B2/EIRENE, EDGE2D/NIMBUS. The coupled system of EIRENE and EDGE2D is now also available and results of B2 and EDGE2D are being compared in the frame of a benchmark activity [130]. An application of one of the edge transport codes to the COMPASS configuration is planned at IPP Prague.

CHAPTER 13

Conclusions

The work presented in sections 11.5 and 11.6 is an activity supported by an international collaboration. The introducing of the dynamic parallel transport model into the ESEL code is a project that has been launched at EURATOM/UKAEA Association in the frame of a cooperation with the Task Force E (W. Fundamenski, V. Naulin). The project is one of the subjects of the annual meeting EFDA-JET TF-E Modelling month and the ITM-IMP4 activity and the subject of a collaboration of EURATOM/IPP.CR Association (J. Seidl, J. Horáček) and EURATOM/Risø Association (A. H. Nielsen). The B2 simulations were performed by F. Subba (Politecnico di Torino, Italy) and supported by D. Coster (IPP Garching, Germany).

The one-dimensional fluid code which has been developed in the frame of the thesis describes the transport of a plasma along the SOL. The model involves only basic physics compared to two-dimensional fluid packages such as B2 or EDGE2D, however, it is a flexible and fast tool that can be used for various applications. The study of the dynamic parallel transport is a part of a long-term project and the coupling of the code with ESEL is envisaged. The benchmark of the code with B2 will continue for more general form of the model and the code might be also compared with a kinetic simulation (D. Tskhakaya, EURATOM Association ÖAW, University of Innsbruck, Austria) and a Vlasov code (S. Devaux, IPP Garching). The plasma transport in the presented code is based on the classical Braginskii expressions and the transport coefficients have been modified using flux limiters. The code can help to test effects of kinetic corrections in the fluid approach and an application of the code to data calculated by the BIT1 code (D. Tskhakaya) is scheduled.

Chapter 12 is an introduction to two-dimensional SOL transport models. Next step, which is now in progress, is to adapt such tool for the COMPASS tokamak.

References

[1] R. H. Huddlestone and S. L. Leonard (Editors), Plasma diagnostic techniques, Academic Press, New York, 1965.

[2] F. F. Chen, Introduction to plasma physics, Academia, Prague, 1984 (in Czech).

[3] Y. P. Raizer, Gas discharge physics, Springer-Verlag, Berlin, 1991.

[4] A. Bogaerts et al., *J. Appl. Phys.* **78**, 2233 (1995).

[5] A. Bogaerts et al., *J. Appl. Phys.* **38**, 4404 (1999).

[6] R. W. Hockney and J. W. Eastwood, Computer simulation using particles, IOP Publishing, Bristol, 1988.

[7] C. K. Birdsall and A. B. Langdon, Plasma physics via computer simulation, IOP Publishing, Bristol, 1991.

[8] J. S. Liu, Monte Carlo strategies in scientific computing, Springer-Verlag, New York, 2001.

[9] S. M. Yen, *Ann. Rev. Fluid Mech.* **16**, 67 (1984).

[10] G. Chen and L. L. Raja, *J. Appl. Phys.* **96**, 6073 (2004).

[11] V. E. Golant, A. P. Zhilinsky and I. E. Sakharov, Fundamentals of plasma physics, John Wiley & Sons, New York, 1980.

[12] J. D. Bukowski and D. B. Graves, *J. Appl. Phys.* **80**, 2614 (1996).

[13] M. Mitchner and C. H. Kruger, Partially ionized gases, John Wiley & Sons, New York, 1973.

[14] J. P. Boeuf, *Phys. Rev. A* **36**, 2782 (1987).

[15] J. D. P. Passchier and W. J. Goedheer, *J. Appl. Phys.* **74**, 3744 (1993).

[16] Z. Donkó, *Phys. Rev. E* **64**, 026401 (2001).

[17] D. Herrebout et al., *J. Appl. Phys.* **90**, 570 (2001).

[18] D. Herrebout et al., *J. Appl. Phys.* **92**, 2290 (2002).

[19] L. M. Montierth et al., *Phys. Fluids B* **4**, 784 (1992).

[20] E. Meeks and M. A. Cappelli, *J. Appl. Phys.* **73**, 3172 (1993).

[21] S. Baboolal, *J. Phys. D: Appl. Phys.* **35**, 658 (2002).

[22] J. F. Wendt (Editor), Computational fluid dynamics – An introduction, Springer-Verlag, New York, 1992.

[23] D. L. Scharfetter and H. K. Gummel, *IEEE Trans. Electron Devices* **16**, 64 (1969).

[24] C. A. J. Fletcher, Computational techniques for fluid dynamics, Vol. I, Springer-Verlag, Berlin, 1991.

[25] K. Charrada et al., *J. Phys. D: Appl. Phys.* **29**, 2432 (1996).

[26] P. Maruzewski et al., *J. Phys. D: Appl. Phys.* **35**, 891 (2002).

[27] P. Freton et al., *J. Phys. D: Appl. Phys.* **33**, 2442 (2000).

[28] J. J. Gonzalez et al., *J. Phys. D: Appl. Phys.* **35**, 3181 (2002).

[29] A. Blais et al., *J. Phys. D: Appl. Phys.* **36**, 488 (2003).

[30] P. Bartoš et al., *WDS'05 Proceedings on Contributed Papers*, Part III, 625 (2005).

[31] S. Longo et al., *Contrib. Plasma Phys.* **46**, 763 (2006).

[32] B. Alterkp et al., *Contrib. Plasma Phys.* **47**, 190 (2007).

[33] E. V. Barnat and G. A. Hebner, *J. Appl. Phys.* **101**, 013306 (2007).

[34] Y. J. Hong et al., *Comput. Phys. Commun.* **177**, 128 (2007).

[35] S. F. Masoudi, *Vacuum* **81**, 871 (2007).

[36] J. I. F. Palop et al., *Plasma Sources Sci. Technol.* **16**, S76 (2007).

[37] E. Havlíčková et al., *35th EPS Conference on Plasma Physics*, *ECA* **32F**, P-2.155 (2008).

[38] P. Bartoš and R. Hrach, *Czech. J. Phys.* **56**, B638 (2006).

[39] T. A. Davis and I. S. Duff, *SIAM J. Matrix Anal. Appl.* **18**, 140 (1997).

[40] T. A. Davis and I. S. Duff, *ACM Trans. Math. Software* **25**, 1 (1999).

[41] T. A. Davis, *ACM Trans. Math. Software* **30**, 165 (2004).

[42] T. A. Davis, *ACM Trans. Math. Software* **30**, 196 (2004).

[43] W. H. Press, S. A. Teukolsky, W. T. Vetterling and B. P. Flannery, Numerical recipes: The art of scientific computing, Cambridge University Press, New York, 2007.

[44] D. Trunec et al., *Contrib. Plasma Phys.* **42**, 91 (2002).

[45] E. Havlíčková et al., *J. Phys.: Conf. Series* **63**, 012019 (2007).

[46] Š. Roučka, Study of plasma-solid interaction at medium pressures, Diploma Thesis, Charles University, Prague, 2008 (in Czech).

[47] O. Maršálek, Advanced techniques of computer modelling in plasma physics, Diploma thesis, Charles University, Prague, 2008.

[48] R. Mareš et al., *Czech. J. Phys.* **52**, D705 (2002).

[49] COMSOL Multiphysics
URL `http://www.comsol.com`

[50] E. Havlíčková, *WDS'06 Proceedings on Contributed Papers*, Part III, 180 (2006).

[51] P. D. Lax and B. Wendroff, *Commun. Pure Appl. Math.* **13**, 217 (1960).

[52] S. A. Yost and P. M. S. V. Rao, *Int. J. Numer. Meth. Fluids* 29, 951 (1999).

[53] J. P. Boris and D. L. Book, *J. Comput. Phys.* **11**, 38 (1973).

[54] S. T. Zalesak, *J. Comput. Phys.* **31**, 335 (1979).

[55] E. Havlíčková et al., *Eur. Phys. J. D* **54**, 313 (2009).

[56] S. C. Brown, Basic data of plasma physics, AIP Press, New York, 1994.

[57] V. Hrubý, Study of plasma-solid interaction by means of hybrid modelling, Diploma Thesis, Charles University, Prague, 2009 (in Czech).

[58] J. P. Boeuf and L. C. Pitchford, *Phys. Rev. E* **51**, 1376 (1995).

[59] C. Punset et al., *J. Appl. Phys.* **83**, 1884 (1998).

[60] P. Bartoš, Hybrid modelling in plasma physics, Ph.D. thesis, Charles University, Prague, 2006 (in Czech).

[61] P. C. Stangeby, *Plasma Phys. Control. Fusion* **42**, B271 (2000).

[62] P. C. Stangeby, The plasma boundary of magnetic fusion devices, IOP Publishing, Bristol, 2000.

[63] J. Wesson, Tokamaks, Oxford University Press, New York, 2004.

[64] P. C. Stangeby and G. M. McCracken, *Nucl. Fusion* **30**, 1225 (1990).

[65] M. Wischmeier, Simulating divertor detachment in the TCV and JET tokamaks, Ph.D. thesis, EPFL, Lausanne, 2004.

[66] R. Schneider et al., *Contrib. Plasma Phys.* **46**, 3 (2006).

[67] NRL plasma formulary
`URL http://wwwppd.nrl.navy.mil/nrlformulary/index.html`

[68] S. I. Braginskii, *Rev. Plasma Phys.* **1**, 205 (1965).

[69] A. Fukuyama, *3rd International Conference on the Frontiers of Plasma Physics and Technology*, (2007).

[70] G. V. Pereverzev and P. N. Yushmanov, ASTRA – Automated system for transport analysis, Max-Planck-Institut für Plasmaphysik, Report IPP 5/98, 2002.

[71] V. Basiuk et al., *Nucl. Fusion* **43**, 822 (2003).

[72] G. Cenacchi and A. Taroni, JETTO – a free boundary plasma transport code, ENEA Report RT/TIB/88/5, 1988.

[73] R. J. Goldston et al., *J. Comput. Phys.* **43**, 61 (1981).

[74] A. Taroni et al., *Contrib. Plasma Phys.* **32**, 438 (1992).

[75] R. Zagórski et al., *Contrib. Plasma Phys.* **38**, 61 (1998).

[76] T. D. Rognlien et al., *Contrib. Plasma Phys.* **34**, 362 (1994).

[77] D. Tskhakaya and S. Kuhn, *Contrib. Plasma Phys.* **42**, 302 (2002).

[78] D. Tskhakaya and R. Schneider, *J. Comput. Phys.* **225**, 829 (2007).

[79] S. Droste et al., *Contrib. Plasma Phys.* **46**, 628 (2006).

[80] L. Lauro-Taroni et al., *35th EPS Conference on Plasma Physics*, *ECA* **32D**, D-1.003 (2008).

[81] G. T. A. Huysmans et al., *33rd EPS Conference on Plasma Physics*, *ECA* **30I**, P-5.152 (2006).

[82] G. L. Falchetto et al., *Plasma Phys. Control. Fusion* **50**, 124015 (2008).

[83] R. Prater et al., *Nucl. Fusion* **48**, 035006 (2008).

[84] T. Oikawa et al., *22nd IAEA Fusion Energy Conference*, *IAEA Proceedings Series*, IT/P6-5 (2008).

[85] A. Fukuyama et al., *22nd IAEA Fusion Energy Conference*, *IAEA Proceedings Series*, TH/P3-8 (2008).

[86] M. D. Carter et al., *Nucl. Fusion* **36**, 209 (1996).

[87] F. Porcelli et al., *Plasma Phys. Control. Fusion* **38** 2163 (1996).

[88] W. Park et al., *Phys. Plasmas* **6**, 1796 (1999).

[89] C. R. Sovinec et al., *Phys. Plasmas* **10**, 1727 (2003).

[90] A. Bécoulet et al., *Comput. Phys. Commun.* **177**, 55 (2007).

[91] V. Parail et al., *22nd IAEA Fusion Energy Conference*, *IAEA Proceedings Series*, IT/P6-7 (2008).

[92] S. Wiesen et al., *35th EPS Conference on Plasma Physics*, *ECA* **32D**, P-5.053 (2008).

[93] J. R. Cary et al., *J. Phys.: Conf. Series* **125**, 012040 (2008).

[94] O. E. Garcia et al., *Phys. Rev. Lett.* **92**, 165003 (2004).

[95] R. Pánek et al., *Czech. J. Phys.* **56**, B125 (2006).

[96] R. Zagórski et al., *Nucl. Fusion* **36**, 873 (1996).

[97] R. Zagórski et al., *Phys. Scr.* **56**, 399 (1997).

[98] R. Zagórski, *J. Tech. Phys.* **38**, 43 (1997).

[99] R. Aymar et al., *Nucl. Fusion* **41**, 10, 1301 (2001).

[100] D. E. Post et al., *At. Data Nucl. Data Tables* **20**, 397 (1977).

[101] R. Zagórski, *J. Tech. Phys.* **37**, 7 (1996).

[102] E. L. Vold et al., *J. Nucl. Mater.* **176-177**, 570 (1990).

[103] M. E. Renskink and T. D. Rognlien, *J. Nucl. Mater.* **266-269**, 1180 (1999).

[104] O. E. Garcia et al., *Plasma Phys. Control. Fusion* **48**, L1 (2006).

[105] W. Fundamenski et al., *Nucl. Fusion* **47**, 417 (2007).

[106] O. E. Garcia et al., *Nucl. Fusion* **47**, 677 (2007).

[107] J. P. Gunn et al., *J. Nucl. Mater.* **363365**, 484 (2007).

[108] SOLPS manual
URL `http://www.ipp.mpg.de/~dpc/solps/solps.pdf`

[109] L. L. Lao et al., *Nucl. Fusion* **30**, 1035 (1990).

[110] D. E. Potter and G. H. Tuttle, *J. Comput. Phys.* **13**, 483 (1973).

[111] M. Petravic, *J. Comput. Phys.* **73**, 125 (1987).

[112] G. J. Radford et al., *Contrib. Plasma Phys.* **38**, 183 (1998).

[113] W. Fundamenski, *Plasma Phys. Controlled Fusion* **47**, R163 (2005).

[114] D. Reiter et al., *J. Nucl. Mater.* **220-222**, 987 (1995).

[115] E. Cupini et al., NET Report EUR XII-324/9 (1984).

[116] E. L. Vold et al., *Phys. Fluids B* **3**, 3132 (1991).

[117] E. L. Vold et al., *J. Comput. Phys.* **103**, 300 (1992).

[118] H. Gerhauser et al., *Nucl. Fusion* **46**, 149 (2006).

[119] R. Zagórski and H. Garhauser, *Phys. Scr.* **70**, 173 (2004).

[120] R. Marchand and M. Simard, *Nucl. Fusion* **37**, 1629 (1997).

[121] T. D. Rognlien et al., *J. Nucl. Mater.* **266-269**, 654 (1999).

[122] V. Rozhansky et al., *Contrib. Plasma Phys.* **40**, 423 (2000).

[123] V. Rozhansky et al., *Nucl. Fusion* **41**, 387 (2001).

[124] G. J. Radford et al., *Contrib. Plasma Phys.* **36**, 187 (1996).

[125] R. Schneider et al., *Contrib. Plasma Phys.* **40**, 328 (2000).

[126] R. Simonini, *Contrib. Plasma Phys.* **34**, 368 (1994).

[127] R. Zagórski et al., *J. Nucl. Mater.* **266-269**, 1261 (1999).

[128] R. Marchand, *Plasma Phys. Control. Fusion* **44**, 871 (2002).

[129] R. A. Vesey and D. Steiner, *J. Comput. Phys.* **116**, 300 (1994).

[130] D. P. Coster et al., *J. Nucl. Mater.* **337-339**, 366 (2005).